

INFORMATION TO USERS

This manuscript has been reproduced from the microfilm master. UMI films the text directly from the original or copy submitted. Thus, some thesis and dissertation copies are in typewriter face, while others may be from any type of computer printer.

The quality of this reproduction is dependent upon the quality of the copy submitted. Broken or indistinct print, colored or poor quality illustrations and photographs, print bleedthrough, substandard margins, and improper alignment can adversely affect reproduction.

In the unlikely event that the author did not send UMI a complete manuscript and there are missing pages, these will be noted. Also, if unauthorized copyright material had to be removed, a note will indicate the deletion.

Oversize materials (e.g., maps, drawings, charts) are reproduced by sectioning the original, beginning at the upper left-hand corner and continuing from left to right in equal sections with small overlaps. Each original is also photographed in one exposure and is included in reduced form at the back of the book.

Photographs included in the original manuscript have been reproduced xerographically in this copy. Higher quality 6" x 9" black and white photographic prints are available for any photographs or illustrations appearing in this copy for an additional charge. Contact UMI directly to order.

U·M·I

University Microfilms International
A Bell & Howell Information Company
300 North Zeeb Road, Ann Arbor, MI 48106-1346 USA
313/761-4700 800/521-0600

Order Number 9334875

Nonlinear dynamics of sliding charge-density waves

Levy, Jeremy, Ph.D.

University of California, Santa Barbara, 1993

U·M·I
300 N. Zeeb Rd.
Ann Arbor, MI 48106

UNIVERSITY OF CALIFORNIA
Santa Barbara

Nonlinear Dynamics of Sliding Charge-Density Waves

A Dissertation submitted in partial satisfaction
of the requirements for the degree of

Doctor of Philosophy
in
Physics
by
Jeremy Levy

Committee in charge:

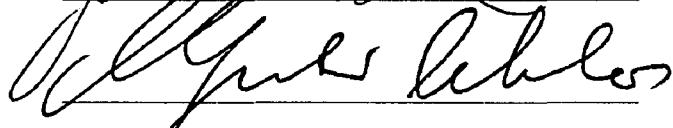
Professor Mark S. Sherwin, Chairperson

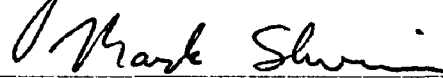
Professor Guenter Ahlers

Professor Jean Carlson

The dissertation of Jeremy Levy is approved:







Committee Chairperson

June 1993

June 2, 1993

Copyright by
Jeremy Levy
1993

Acknowledgements

I am deeply indebted to many people who have helped make this thesis possible. I was immensely fortunate to have had Professor Mark Sherwin as my thesis advisor. His highly creative and thorough approach toward experimental physics has profoundly shaped my own views. He has also been unfailingly supportive, always thinking of his students first, and was a pleasure to work with and to know personally.

In the course of my graduate career I have also had the pleasure of interacting with many other faculty members of this department. Professor Jean Carlson has been enormously helpful to my understanding of many of the theoretical issues related to charge-density-wave phenomena. I have also had many illuminating conversations with Professors John Cardy, Alan Heeger, Doug Scalapino and Robert Schrieffer. I thank Professors Daniel Hone and Günther Ahlers for serving on my thesis committee. I look forward to working with Professor David Awschalom as a postdoc.

I have also enjoyed fruitful collaborations with Farid A. Abraham, James Theiler, and Kurt Wiesenfeld, and have benefitted from discussions with Shobo Bhattacharya, Sue Coppersmith, Geoff Grinstein, Peter Littlewood, Alan Middleton, Chris Myers, and Robert Thorne. Afshin Montakhab has been enormously helpful in sorting out many of the details of the microscopic theory of CDWs.

I would also like to acknowledge the help and support of others in the Sherwin group: Bill Bewley, John Cerne, Keith Craig, Chris Felix, Bryan Galdrikian, and John Plombon. I wish Rich Wilson the best of luck in the years ahead. A special thanks goes to the “First-Year Gang”: Robert Danen, Paul Pinsukanjana, and Raghu Rangaranjan. I thank David Lederman for the use of his \LaTeX thesis template.

Neil Nighman has done an excellent job in growing world-class samples of NbSe_3 . Rudy Stuber helped me enormously with the design of my apparatus, and Andy Weinberg was instrumental in helping build it. I would especially like to thank Henry Sarria and Dr. John Alexander of the Ferro Corporation for their invaluable time and effort.

I would also like to acknowledge help from many hard-working undergraduates who have helped out over the years. Basil Sabbah worked hard toward the completion of the shielded room which has proved essential in the radio-frequency measurements. Suzanne Kyre helped

build much of the high-frequency circuits used in the experiments. Olaf Dippel wrote many of the LabVIEW software drivers that were used in running the experiments. Jason White put up with much abuse and kept our computers running.

I am thankful for the love and support of my family, and especially my wife Chandralekha.

I gratefully acknowledge receipt of a UCSB General Affiliates Graduate Dissertation Fellowship award. The research comprising this thesis was supported in part by NSF Grants DMR8901651 and DMR9214995, INCOR, and the Alfred P. Sloan Foundation. Computations were performed in part at the San Diego Supercomputer Center.

To Chandralekha

Vita

May 18, 1965	Born: New York City, New York.
March 1988	B.A. with Honors in Physics, Harvard University.
September 1988 – January 1989	Teaching Assistant, Dept. of Physics, University of California, Santa Barbara.
January 1989 – June 1993	Research Assistant, Dept. of Physics, University of California, Santa Barbara.

PUBLICATIONS

- “Search for a Bhabha-Scattering Resonance near $1.8 \text{ MeV}/c^2$ ”, A. P. Mills, Jr. and J. Levy, *Phys. Rev. D* **36**, 707 (1987).
- “Conduction Delays in Switching NbSe_3 : Sensitive Dependence on Initial Configuration”, J. Levy and M. S. Sherwin, *Phys. Rev. B* **43**, 8391 (1991).
- “Poincare Sections of Charge-Density-Wave Dynamics: Mode-Locking”, J. Levy and M. S. Sherwin, *Phys. Rev. Lett.* **67**, 2846 (1991).
- “Multiple Attractors and Dynamical Solitons in Mode-Locked Charge-Density Waves”, J. Levy and M. S. Sherwin, in *Proceedings of the 1st Experimental Chaos Conference*, edited by S. Vohra, M. Spano, M. Schlesinger, L. M. Pecora, and W. Ditto, (World Scientific, New Jersey, 1992).
- “Unified Model of Switching and Nonswitching Charge-Density-Wave Dynamics”, J. Levy, M. S. Sherwin, F. F. Abraham, and K. Wiesenfeld, *Phys. Rev. Lett.*, **68**, 2968 (1992).
- “Time-Domain Study of Low-Dimensional Chaos in the Switching Charge-Density-Wave Conductors NbSe_3 ”, J. Levy, M. S. Sherwin, and J. Theiler, *Phys. Rev. Lett* **70**, 2957 (1993).

“Impulse Response of the Switching Charge-Density-Wave Conductor NbSe₃: A Novel Delayed Transition”, J. Levy and M. S. Sherwin, (in preparation).

“Impulse Response of Switching NbSe₃: Experiment and Theory”, J. Levy and M. S. Sherwin, (submitted to Phys. Rev. B).

“Low-Dimensional Chaos and High-Dimensional Behavior in the Switching Charge-Density-Wave Conductor NbSe₃”, J. Levy, M. S. Sherwin and J. Theiler (submitted to Phys. Rev. B).

Abstract

Nonlinear Dynamics of Sliding Charge-Density Waves

by
Jeremy Levy

The nonlinear dynamics of the sliding charge-density-waves have been studied. When the CDW slides, it generates current oscillations whose frequency ω_{nbn} is proportional to the CDW velocity. One can observe mode-locking in response to combined dc+ac driving when a harmonic of ω_{nbn} becomes sufficiently close to a harmonic of the drive frequency ω_{ac} . The CDW was driven with combined dc+ac electric fields, and the time-domain response was measured. Poincaré sections of the attractor are reconstructed using time-delay embeddings. Many surprising features are explained only by taking into account many degrees of freedom.

At lower temperatures, many crystals of NbSe₃ exhibit “switching” behavior, in which the CDW depins abruptly and hysteretically. In the switching regime, the CDW exhibits a period-doubling route to chaos when combined dc+ac fields are applied. The chaotic behavior has been measured in the time domain. Time-series analysis confirms that the chaotic behavior is indeed low-dimensional, and provides an estimate of the number of active degrees of freedom. For ac driving frequencies less than 5 MHz high-dimensional behavior is observed which is indistinguishable from random noise.

A model of both switching and non-switching CDW dynamics is proposed which takes into account the interaction of the CDW with uncondensed carriers. Hysteresis is observed in the limit of strong pinning and/or high temperature, consistent with experiment. However, in NbSe₃ there are uncondensed carriers which do not freeze out at low temperatures. It remains a mystery why these uncondensed carriers do not appear to interact with the CDW in the same way as thermally excited quasiparticles.

Another unique phenomenon of “switching” samples is the phenomenon of delayed conduction. When a rectangular voltage pulse is applied which is above the threshold for CDW conduction, the CDW begins to slide only after a delay τ . Detailed measurements of the impulse response of switching NbSe₃ have been performed as a function of pulse height, temperature, and initial configuration. The phenomenon of conduction delays provides

strong constraints on any model of switching CDW dynamics. Numerical simulations of the proposed model of CDW dynamics agree well with experiment.

Contents

1	Introduction	1
1.1	Basic Notions	1
1.1.1	What is a Charge-Density Wave?	1
1.2	The Peierls Transition	3
1.2.1	Lindhard Theory	3
1.2.2	The Fröhlich Hamiltonian	4
1.3	NbSe₃	8
1.4	The Fukuyama-Lee-Rice Model	9
1.4.1	Strong Pinning, Weak Pinning	12
1.4.2	Normal Carriers	13
1.5	Narrow-Band Noise	14
1.6	Mode-Locking	15
1.6.1	Mode-locking in Josephson Junctions	15
1.6.2	Mode-Locking in CDWs	17
1.6.3	Measurements of Mode-Locking	19
1.7	Switching	27
1.7.1	Delayed Switching	28
1.7.2	Mode-Locking and Chaos	29
1.8	What's Ahead	32
2	Experimental Methods	35
2.1	Cryostats and Temperature Control	35
2.1.1	First Set-Up	35
2.1.2	Second Set-Up	38
2.2	Sample Growth and Preparation	39
2.2.1	Crystal Growth Procedure	39
2.2.2	Mounting Samples	40
2.3	Electronics	42

2.4	Noise Reduction	44
2.5	Software	46
3	Conduction delays in switching NbSe₃: sensitive dependence on initial configuration	49
3.1	Introduction	49
3.2	Experimental Methods	50
3.3	Experimental Results	51
3.4	Discussion	53
4	Multiple Attractors and Dynamical Solitons in Mode-Locked Charge-Density Waves	57
4.1	Introduction	57
4.2	Experimental Set-up	59
4.3	Experimental Results	59
5	Low-Dimensional Chaos and High-Dimensional Behavior in the Switching Charge-Density-Wave Conductor NbSe₃	71
5.1	Introduction	71
5.2	Experimental Technique	73
5.3	Experimental Results	74
5.3.1	Differential Conductance Measurements	74
5.3.2	Detailed form of Chaotic Currents	76
5.3.3	Period-Doubling Route to Chaos	78
5.3.4	High-Dimensional Dynamics	80
5.4	Analysis	84
6	Unified Model of Switching and Non-Switching Charge-Density-Wave Dynamics	93
6.1	Introduction	93
6.2	Derivation of the Model	94
6.3	Switching	97
7	Impulse Response of the Switching Charge-Density-Wave Conductor NbSe₃: A Novel Delayed Transition	103
7.1	Introduction	104
7.2	Experimental Methods	105
7.3	Experimental Results	106
7.3.1	Distribution of Delays	106
7.3.2	Temperature Dependence of Delays	108

7.3.3	“Melting” the CDW	112
7.3.4	“Depolarizing” the CDW	117
7.4	Numerical Results	118
7.4.1	Previous Work	118
7.4.2	Equations of Motion	120
7.4.3	Numerical Experiments	121
7.5	Analysis and Discussion	125
7.5.1	Origin of Delayed Conduction	125
7.5.2	Dependence on Initial Configuration	127
7.5.3	Pulse Height Dependence	129
7.5.4	Temperature Dependence	129
8	Conclusions	131

List of Figures

1.1	One-dimensional crystal in undistorted state and Peierls-distorted state. . . .	2
1.2	Fermi surface nesting in one and two dimensions.	5
1.3	Lindhard Function in one, two, and three dimensions at zero temperature. . .	6
1.4	Kohn anomaly of phonons in $d = 1, 2, 3$ dimensions.	7
1.5	Resistance versus temperature of NbSe ₃	9
1.6	Mechanical analogue of the Fukuyama-Lee-Rice model.	11
1.7	Plot of CDW phase ϕ versus position.	11
1.8	Plot of the charge-density in two regimes of pinning.	12
1.9	Temperature dependence of the linear and nonlinear portion of the current in K _{0.3} MoO ₃	14
1.10	Nonlinear conduction in K _{0.3} MoO ₃ at T=4.2 K	15
1.11	CDW I-V characteristic for different temperatures, using parameters appropriate to K _{0.3} MoO ₃	16
1.12	Fundamental frequency of the narrow-band noise versus measured CDW current.	16
1.13	Power spectrum of narrow-band noise for various values of the dc driving current I_{dc}	17
1.14	Differential resistance in NbSe ₃ as a function of ω_{ex} , for various values of the dc bias I_{dc}	18
1.15	Plot of I_{cdw} versus V_{dc} in the presence of ac driving	19
1.16	Devil's Staircase in response to pulsed driving for Fukuyama-Lee-Rice model in $d = 2$ dimensions	20
1.17	Simple two-fluid picture of CDW and Ohmic conductivity.	21
1.18	Differential resistance dV/dI in the upper transition of NbSe ₃	21
1.19	Differential resistance dV/dI as a function of the dc bias current in the absence and presence of ac driving.	22
1.20	Differential resistance in the presence (top trace) and absence (bottom trace) of 50 MHz rf driving.	23
1.21	Power spectrum of narrow-band noise in the absence and presence of ac driving. 24	24

1.22	Histogram of narrow-band-noise amplitude in the locked and unlocked state	24
1.23	Histogram of ω_{nbn} for sample which displays intermittent mode-locking behavior.	25
1.24	Phase-space attraction toward an invariant 2-torus.	25
1.25	Poincaré section of the Josephson junction simulator.	26
1.26	Predicted and measured power spectrum for the noise-driven Josephson junction simulator.	27
1.27	Arnold tongue diagram depicting mode-locked intervals in the circle map.	28
1.28	Current-voltage curves in NbSe ₃ as a function of temperature.	29
1.29	Digitally smoothed response waveform to a current pulse above threshold for switching.	30
1.30	Distribution of time to switch T for two different driving currents I	31
1.31	Current-Voltage traces in the presence of 15 MHz sinusoidal ac driving	31
1.32	Power spectra of the current response in the Shapiro step region of a sample of NbSe ₃	32
1.33	Power spectrum of CDW current in the presence and absence of $f = 0.5$ MHz rf driving.	33
2.1	Schematic drawing of sample mount and housing.	36
2.2	Set-up for performing measurements on high- and low-impedance samples.	37
2.3	Photograph of 4 1/2 in. conflat flange used for mounting samples.	38
2.4	Scanning electron micrograph of two crystals of NbSe ₃	41
2.5	Scanning electron micrograph of a crystal of NbSe ₃ with a fairly uniform cross section.	42
2.6	(a) Scanning electron micrograph of the crystal of NbSe ₃ used in the mode-locking experiment described in Ch. 4 . (b) Close-up of same crystal.	43
2.7	Close-up of a melted crystal of NbSe ₃	44
2.8	Schematic drawing of subtraction circuit for experiments with combined ac and dc driving.	45
2.9	Sample LabVIEW Virtual Instrument.	47
3.1	CDW current response to four identical voltage pulses.	51
3.2	Plot of distribution of switching delays.	52
3.3	Average delay $\langle\tau\rangle$ and standard deviation σ versus pulse height.	54
4.1	Differential resistance dV/dI vs. dc current I_{dc} in absence and presence of ac driving.	60
4.2	High-sampling-rate measurement of CDW voltage	61
4.3	Poincaré sections obtained by method of delays.	62

4.4	Dynamic staggered order parameter (DSOP) for various values of I_{dc} near the 1:2 mode-locked step.	64
4.5	Plot of every d^{th} point of the time series shown in Fig. 4.3 (d) for various values of d	65
4.6	Plot of time series near the edge of the 0 : 1 mode-locked step	66
4.7	Plot of DSOP W_n for the coupled circle map, Eq. 4.4	69
4.8	Plot of $\Delta\varphi \equiv \varphi(i, n) - \varphi(i, 0) - n\pi$ for n even.	70
5.1	Power spectrum of current oscillations for sample No. 1 at $T=19.3$ K ($R=375 \Omega$) at $T=47.7$ K, length=1.8 mm).	74
5.2	Differential conductance in the absence and presence of 20 MHz rf driving	75
5.3	High-sampling-rate measurement of CDW current versus time	77
5.4	Bifurcation diagram constructed from time series	79
5.5	Time-delay reconstruction of Poincaré section from time series, and corresponding analog power spectra (below) at $T=23.8$ K and $\omega_{ex}/2\pi=20$ MHz (see text for discussion). (a,e) $V_{dc}=153.1$ mV. (b,f) $V_{dc}=157.4$ mV. (c,g) $V_{dc}=161.3$ mV. (d,h) $V_{dc}=163.6$ mV.	80
5.6	Poincaré section obtained from time series at $T=28.8$ K and $\omega_{ex}/2\pi=20$ MHz	81
5.7	Differential conductance dI/dV and rms noise at $T=23.8$ K for $\omega_{ex}/2\pi=4$ MHz, $V_{ac}=43.0$ mV	82
5.8	High-sampling-rate measurement of CDW current versus time	83
5.9	Close-ups of dI/dV near region which shows high- and low-dimensional behavior	85
5.10	Poincaré section from time series at $T=23.8$ K and $\omega_{ex}/2\pi$	86
5.11	Poincaré section obtained from time series at $T=23.8$ K and $\omega_{ex}/2\pi=4$ MHz	87
5.12	Forecasting error versus embedding dimension and forecasting time	88
6.1	Circuit representations of Fukuyama-Lee-Rice model and Unified model	96
6.2	Plot of time-averaged CDW current versus V for various values of α and K	98
6.3	Plot of hysteresis as a function of α and K	99
6.4	Steady-state total current $J(t)$ versus time for two different initial configurations	101
7.1	I - V curves at various temperatures in the switching regime	107
7.2	Schematic representation of the impulse response experiments.	108
7.3	Distribution of delays as a function of V_p and temperature	109
7.4	Plot of average switching delay $\bar{\tau}(\square)$ and standard deviation $\sigma(\Delta)$	110
7.5	Average switching delay $\bar{\tau}$ versus ϵ for different temperatures	111
7.6	Experimentally measured CDW current versus time for a typical "short" delay at four different temperatures	113
7.7	Plot of crossover time τ_{co} and switching time t_{sw} versus inverse temperature	114

7.8	Current versus time for various values of V_p , for two different initial conditions	115
7.9	Final current versus pulse height V_p for two successive pulses (1 and 2) after heating the sample above the Peierls temperature	116
7.10	Current versus time for two successive pulses at various values of V_p , after a 1 s depolarizing pulse	117
7.11	Final current versus pulse height V_p for pulse 1 and pulse 2 for depolarizing experiment	119
7.12	Numerical simulations of Eq. 7.11 for two different initial configurations	122
7.13	Final CDW current versus pulse height E_p for configurations 1 and 2 and $\gamma_1=10$	124
7.14	CDW current response to a pulse $E_p = 0.6$ for three different values of γ_1	124
7.15	Plot of delay τ versus reduced pulse height ϵ for two values of γ_1	125
7.16	Phasor representation of the order parameter Ψ	126
7.17	“Configuration-space” and current plot of $\Psi(t)$, beginning from a polarized configuration	128

Chapter 1

Introduction

It's slinky, it's slinky,
It's fun, it's a wonderful toy.
It's slinky, it's slinky,
It's fun for a girl or a boy,
It's fun for a girl or a boy.
—James Industries

1.1 Basic Notions

1.1.1 What is a Charge-Density Wave?

A charge-density wave (CDW) is a periodic modulation of the electronic density which arises in quasi-one-dimensional materials [1, 2, 3, 4, 5]. Associated with that density modulation is a distortion of the underlying lattice. The CDW instability was first proposed by Peierls in 1955 [6]. Consider a one-dimensional lattice of atoms with spacing a , illustrated in Fig. 1.1(a). In the nearly-free-electron picture, the electronic energy is approximately a quadratic function of the momentum q until one reaches the Brillouin zone, at $q = \pm\pi/a$. The gap in energy at the Brillouin zone is created by the interaction of the Bloch electrons with the periodic potential lattice. The magnitude of the gap is given to first order by $\Delta = 2|V_{2q}|$, where V_{2q} is $2q$ -Fourier component of the lattice potential $V(x)$. At zero temperature, the electrons will fill the lowest energy states up to the Fermi surface, which for a half-filled band is just the two points $\pm\pi/2a$.

Peierls showed that a one-dimensional electronic system is unstable to any perturbation which will create a gap at the Fermi surface. For a half-filled band, if the lattice were to distort as shown in Fig. 1.1(b), a gap would form at the Fermi surface. The electrons

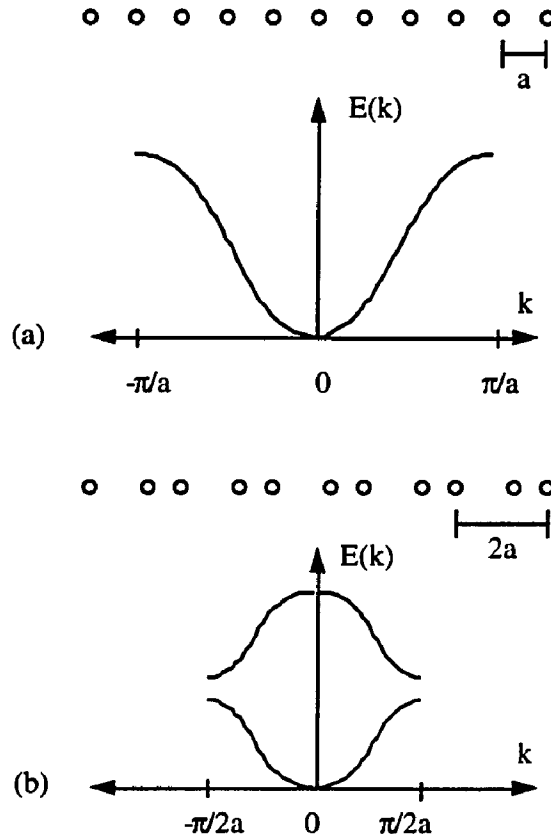


Figure 1.1: (a) One-dimensional crystal in the nearly-free electron approximation. Top part is a schematic real-space picture of the atomic spacings, with lattice constant a . Bottom part shows the energy band for a nearly-free electron gas in one dimension. (b) One-dimensional crystal after Peierls distortion for a half-filled band. The lattice constant has doubled while the Brillouin zone has become half. Bottom part shows the energy band for the Peierls-distorted state.

near the Fermi surface would have their energy lowered. The cost in elastic energy of producing a distortion is proportional to Δ^2 , where 2Δ is the CDW gap, whereas the electronic gain is proportional to $\Delta^2 \log \Delta$ in one dimension, so that the Peierls ground state is always favored in one dimension. Fluctuations destroy long-range order in a truly one-dimensional system, but in quasi-one-dimensional materials such as NbSe₃, long-range ordering is achieved through the transverse coupling, and the Peierls transition occurs at non-zero temperature.

1.2 The Peierls Transition

Several concepts associated with the Peierls transition will be important later, and so it is worth discussing in brief the microscopic theory of the Peierls transition. The mechanism which gives rise to the Peierls instability is the electron-phonon interaction, combined with the peculiar geometry of the Fermi surface in quasi-one-dimensional metals. Lattice distortions perturb the electronic potential in a metal, and these perturbations are typically screened out over the Thomas-Fermi screening length λ_{TF} . But for perturbations with wavevector q near $2k_F$, as we shall see, the screening becomes large and indeed diverges in one dimension. The consequences of this will become clear later, but first let me describe the Lindhard approach to screening, in which it will become clear why $q = 2k_F$ fluctuations are so important.

1.2.1 Lindhard Theory

In a metal, the dielectric function $\epsilon(q, \omega)$ has the form:

$$\epsilon(q, \omega) = 1 + \frac{4\pi e^2}{q^2} F(q, \omega, T). \quad (1.1)$$

$F(q, \omega, T)$ is the temperature-dependent Lindhard (response) function

$$F(q, \omega, T) = \sum_k \frac{f_k - f_{k+q}}{\epsilon_{k+q} - \epsilon_k - \hbar\omega_q + i\eta}, \quad (1.2)$$

where $f_k = (1 + \exp(\beta\epsilon_k))^{-1}$ is the Fermi distribution function and $\beta = 1/k_B T$. It is also related to the linear susceptibility $\chi(q, \omega, T)$

$$\chi(q, \omega, T) = \frac{e^2}{q^2} F(q, \omega, T) \quad (1.3)$$

The Lindhard formalism is really nothing more than first-order time-dependent perturbation theory, and consequently it involves a sum over all the electronic states. In the numerator, one has the difference of the occupation of electronic states at k and $k + q$.

At zero or low temperatures, the numerator will vanish unless the state k is below the Fermi level and $k + q$ is above it, or vice versa. Since one is interested in the most divergent contributions to $F(q, \omega, T)$, one should consider what requirements must be made in order for the denominator in Eq. 1.2 to vanish. For now, let us consider the case where $\omega = 0$. Then, the denominator vanishes when the two states have the same energy. This divergence will be unimportant unless the numerator is non-vanishing as well, and so we see that electronic states on opposite sides of the Fermi surface can give potentially large contributions to the Lindhard function. Furthermore, depending on the shape of the Fermi surface, these contributions can be large or small, depending on how well “nested” the Fermi surface is. That is, if there are large portions of the Fermi surface which are separated by a constant wavevector q , then the divergence of the Lindhard function will be more pronounced. When this happens, the Fermi surface is said to be “well-nested”.

Fig. 1.2 shows an example of nesting in one and two dimensions. In Fig. 1.2(a), the Fermi “surface” consists of two points, and so the nesting is perfect. The solid lines show the original Fermi “points”, and the dashed lines show the same points displaced by $Q = 2k_F$. In Fig. 1.2(b), one considers the effects of higher spatial dimensions, where the Fermi surface is quasi-one-dimensional, so that it is essentially two planes. In Fig. 1.2(c), one sees that only a small portion of the Fermi surface is nested for an isotropic metal. But, in certain cases, such as Fig. 1.2(d), nesting can occur over a large portion of the Fermi surface even in higher dimensions.

Fig. 1.3 shows the Lindhard function in one, two and three dimensions. In one dimension, there is a logarithmic singularity that becomes rounded at finite temperature. In two dimensions, there is a divergence in the slope at $q = 2k_F$, and in three dimensions, the curvature diverges.

One of the consequences of the diverging susceptibility is a dramatic effect on phonon frequencies near $2k_F$. Because the electrons screen $2k_F$ distortions so well, the restoring force between neighboring ions is reduced, and hence the phonon frequency is driven to zero at $q = 2k_F$. This phenomena is known as the Kohn anomaly in general, and in one dimension (because it is so pronounced), it is known as the giant Kohn anomaly.

1.2.2 The Fröhlich Hamiltonian

Let us consider the simplest system in which all of this occurs, known as the Fröhlich Hamiltonian:

$$H_{\text{Fröhlich}} = \sum_k \epsilon_k c_k^\dagger c_k + \sum_q \hbar\omega_q b_q^\dagger b_q + \sum_{k,q} g(q) c_{k+q}^\dagger c_k (b_q + b_{-q}^\dagger). \quad (1.4)$$

The first term is the unperturbed electron hamiltonian, the second term gives the unperturbed phonon system, and the third term gives the electron-phonon interaction, the

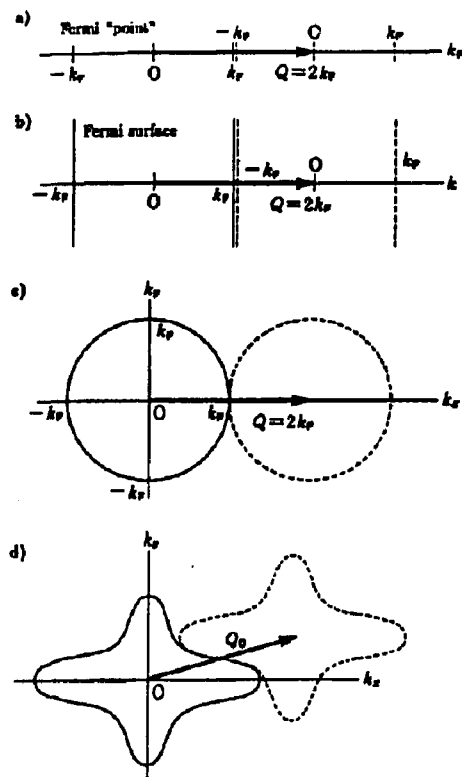


Figure 1.2: Fermi surface nesting in one and two dimensions. (a) Fermi surface consists of two "points". (b) Fermi surface consists of two lines. Such behavior is expected if the transverse coupling is weak. (c) Fermi surface for a 2-d isotropic metal. Nesting is only over a small portion of the Fermi surface. (d) Two-dimensional Fermi surface in which nesting is much more pronounced (ref. [3]).

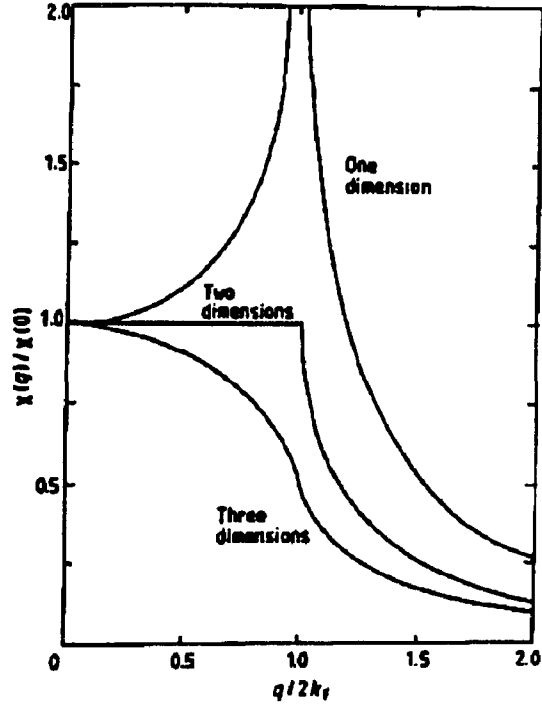


Figure 1.3: Lindhard Function in one, two, and three dimensions at zero temperature. At finite temperatures, divergences are rounded (ref. [7]).

strength of which is given by a wave-vector dependent electron-phonon coupling constant $g(q)$. The phonon creation and annihilation operators are related to the displacement operator by

$$x = \sqrt{\frac{\hbar}{2M\omega}}(b + b^\dagger) \quad (1.5)$$

For the simple monatomic lattice we are considering, there are only acoustic phonons, whose phonon dispersion will be assumed to be linear. The electron-phonon interaction renormalizes the bare phonon energies, yielding a new dispersion relation:

$$\Omega_q^2 = \omega_q^2 \left(1 - \frac{g(q)^2}{\hbar\omega_q} F(q, \omega, T)\right). \quad (1.6)$$

The new phonon dispersion relation is illustrated in Fig. 1.4 for $d = 1, 2, 3$ dimensions.

As was mentioned earlier, the Lindhard function diverges in one dimension at zero temperature:

$$F(q, \omega = 0, T = 0) = D(\epsilon_F) \frac{k_F}{q} \ln \left| \frac{2k_F + q}{2k_F - q} \right| \quad (1.7)$$

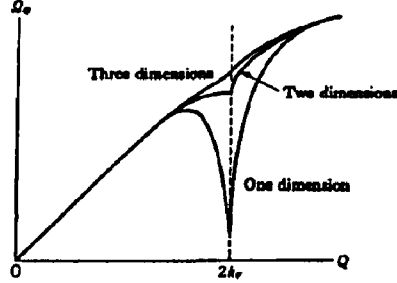


Figure 1.4: Kohn anomaly of phonons in $d = 1, 2, 3$ dimensions (ref. [3]).

Here $D(\epsilon_F)$ is the density of states at the Fermi surface.

As the temperature is lowered, the phonon energy at $q = 2k_F$ is reduced. The temperature at which the $2k_F$ phonon goes to zero is the mean-field Peierls temperature T_P^{MF} , and is given for tight-binding electrons by

$$k_B T_P^{\text{MF}} = 2.28 \epsilon_F e^{-1/\lambda_0} \quad (1.8)$$

where λ_0 is the dimensionless phonon coupling constant $\lambda_0 = g(2k_F)^2 D(\epsilon_F) / \hbar \omega_{2k_F}$.

Below T_P , the $2k_F$ phonon modes will be macroscopically occupied:

$$\langle b_{\pm 2k_F} \rangle = \langle b_{\pm 2k_F}^\dagger \rangle = \frac{u}{2} \left(\frac{\hbar}{2M\omega_{2k_F}} \right)^{-\frac{1}{2}}, \quad (1.9)$$

where u is the amplitude of the ionic displacement and M is the ionic mass. If one only considers the interaction of the electrons with the $2k_F$ mode (i.e., mean-field approximation), then the Hamiltonian Eq. 1.4 becomes quadratic in c_k and c_k^\dagger , and can be diagonalized by a Bogoliubov transformation:

$$H = \sum_k E_k \gamma_k^\dagger \gamma_k + \frac{1}{2} N K u^2 \quad (1.10)$$

where K is the elastic constant of the $2k_F$ mode, and γ_k^\dagger and γ_k are given by

$$\gamma_k^\dagger = u_k c_k^\dagger + v_k e^{-i\phi} c_{k-2k_F}^\dagger \quad (1.11)$$

$$\gamma_{-k}^\dagger = u_{-k} c_{-k}^\dagger + v_{-k} e^{-i\phi} c_{2k_F-k}^\dagger. \quad (1.12)$$

The coefficients u_k and v_k satisfy relations identical to that in the BCS theory of superconductivity:

$$u_k = \sqrt{(1 + \epsilon_k/E_k)/2}, \quad (1.13)$$

$$v_k = \text{sgn}(|k| - k_F) \sqrt{(1 - \epsilon_k/E_k)/2}. \quad (1.14)$$

The quasiparticle energies are given by

$$E_k = \text{sgn}(|k| - k_F) \sqrt{\epsilon_k^2 + \Delta^2} \quad (1.15)$$

where $\Delta = g(2k_F) | \langle b_{2k_F} + b_{2k_F}^\dagger \rangle |$. The CDW gap is 2Δ , and has a BCS-like dependence on temperature.

The order parameter is complex, and therefore has an amplitude and a phase:

$$\Delta e^{i\phi} = g(2k_F) \langle b_{2k_F} + b_{2k_F}^\dagger \rangle. \quad (1.16)$$

The CDW ground state is formed by filling all the quasiparticle states below the gap:

$$|\Psi_{CDW}\rangle = \prod_{k=0}^{k_F} \gamma_k^\dagger \gamma_{-k}^\dagger |0\rangle \quad (1.17)$$

The electronic charge density in the ground state can easily be calculated:

$$\rho(x) = \mathcal{FT} \langle \Psi_{CDW} | \sum_k c_{k+q}^\dagger c_k | \Psi_{CDW} \rangle = \rho_0 + \rho_1 \cos(2k_F x + \phi), \quad (1.18)$$

where

$$\frac{\rho_1}{\rho_0} = \frac{2\Delta}{\pi\lambda_0\epsilon_F} = \frac{2\Delta}{\pi\epsilon_F} \ln\left(\frac{4\epsilon_F}{\Delta}\right). \quad (1.19)$$

The case of interest is when the CDW wavelength $\lambda_{CDW} = \pi/k_F$ is not commensurate with the lattice spacing a . In that case, the ground state energy is independent of the phase ϕ . The formation of a charge-density wave is an example of a spontaneous symmetry breaking that occurs often in physical systems. We shall see that the $U(1)$ symmetry of the order parameter (invariance under multiplication by $e^{i\theta}$) has several important consequences, one of which is the existence of gapless excitations or Goldstone modes, corresponding to the rigid translation of the CDW condensate and yielding a net current.

1.3 NbSe₃

An introduction would not be complete without discussing some of the material aspects of CDWs. In this thesis I have measured exclusively the properties of the CDW material NbSe₃. There are several excellent references which discuss the properties of NbSe₃ and related MX₃ compounds, as well as the other types of known CDW materials [3, 8]. The most important facts about NbSe₃ are as follows: In NbSe₃, there are actually two CDWs, and a portion of the Fermi surface is not completely gapped, so that free carriers remain at low temperatures. The formation of two CDWs shows up rather dramatically in the resistance versus temperature curve shown in Fig. 1.5. There are two peaks corresponding to the freezout of normal carriers, but the resistance eventually drops due to the increasing mobility

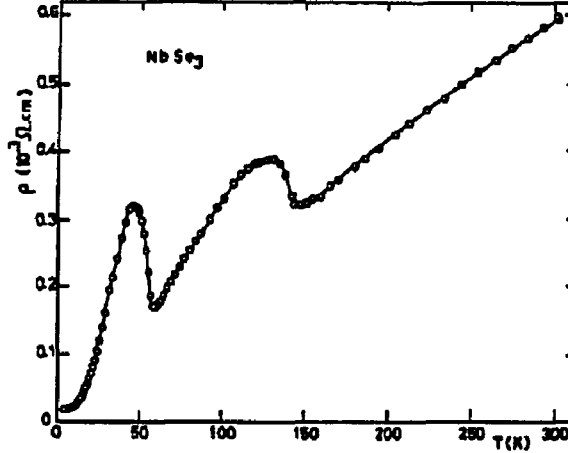


Figure 1.5: Resistance versus temperature of NbSe₃ (ref. [9, 7]).

of the uncondensed carriers. The first Peierls temperature occurs at $T_{P1}=145$ K, while the second occurs at $T_{P2}=59$ K. Although only a small portion of the Fermi surface remains ungapped at low temperatures, it has a dramatic effect on the residual resistance ratio (RRR) = $R(T=300 \text{ K})/R(T=4.2 \text{ K})$, which can be as high as 400 in some samples [10].

1.4 The Fukuyama-Lee-Rice Model

If one is interested in the low-energy excitations of the CDW, then it is useful to write down an effective Hamiltonian by expanding in powers of the phase of the order parameter ϕ and various space and time derivatives. When one does this, one obtains to lowest nontrivial order:

$$H_0 = \int d^d x \left[\frac{1}{2} m^* \dot{\phi}^2 + \frac{1}{2} K (\nabla \phi)^2 \right], \quad (1.20)$$

where d is the dimension of the CDW, and m^* is the effective mass density of the CDW, and K is the Young modulus of the CDW. Empirically, m^* is negligible for many of the regimes of interest, and henceforth will be ignored.

In real materials there are always defects: impurities, grain boundaries, dislocations, etc. Because there exist gapless excitations, which correspond to long-wavelength expansions and compressions of the CDW, there is a coupling of the CDW to these impurities. For simplicity, assume that at sites x_i there exist impurities which perturb the CDW locally in the vicinity of x_i . The impurity potential $V(x - x_i)$ is usually approximated by a delta

function $V(\mathbf{x} - \mathbf{x}_i) \approx V_0 \delta(\mathbf{x} - \mathbf{x}_i)$, and one should add to Eq. 1.20 the term

$$H_{imp} = V_0 \rho_0 \sum_i \cos[2k_F \mathbf{x}_i + \phi(\mathbf{x}_i)] \quad (1.21)$$

One can also couple the CDW to an electric field. The coupling is straightforward:

$$H_{ext} = -\frac{e}{\pi} E \phi \quad (1.22)$$

The equations of motion are obtained by assuming overdamped motion,

$$\gamma_0 \dot{\phi}(\mathbf{x}) = -\frac{\delta(H_0 + H_{imp} + H_{ext})}{\delta\phi} \quad (1.23)$$

where γ_0 is a phenomenological damping constant corresponding to the intrinsic CDW damping.

Eq. 1.23 is usually written down in discretized form, where the degrees of freedom between impurity sites are integrated out [11, 12]. The most common version is when the impurity sites \mathbf{x}_i are assumed to form a lattice, but the phase of the impurity coupling $\beta_i \equiv Q\mathbf{x}_i$ is assumed to be a random variable modulo 2π . In this case, the equations of motion become:

$$\gamma_0 \dot{\phi}_i = K(\phi_{i+1} - 2\phi_i + \phi_{i-1}) + V_0 \sin(\phi_i - \beta_i) + E(t) \quad (1.24)$$

where γ_0 is a phenomenological damping constant, ϕ_i describes the phase at impurity site i , and $E(t)$ is a time-dependent electric field.

Eq. 1.24 is known as the classical-deformable or Fukuyama-Lee-Rice (FLR) model. Several crucial assumptions have been made in arriving at this model. First, it was assumed that the phase ϕ of the order parameter is the only relevant part which contributes to the dynamics, and that amplitude fluctuations require too much energy to be relevant. Empirically, this assumption appears sound in many experimentally accessible regimes. However, Coppersmith has shown [13] that strain energies become unbounded in the sliding state, implying that amplitude degrees of freedom must become important. Another assumption is that the CDW does not interact with normal or uncondensed carriers. When the CDW deforms, the local charge density changes and is compensated by a backflow of normal carriers. This interaction can become quite strong at low temperatures. The consequences of this interaction will be discussed in section 1.4.2, and in chapter 6

The Fukuyama-Lee-Rice (FLR) equations of motion have a quasi-intuitive mechanical analogy, which is that of (massless) balls moving down a washboard, coupled together by springs, shown in Fig. 1.6. The washboard phases are random with respect to one another, and the balls may or may not slide, depending on the amount of tilt (proportional to $E(t)$). It should be clear that if the springs are fairly weak, there will be many metastable states of the CDW, as shown in Fig. 1.7.

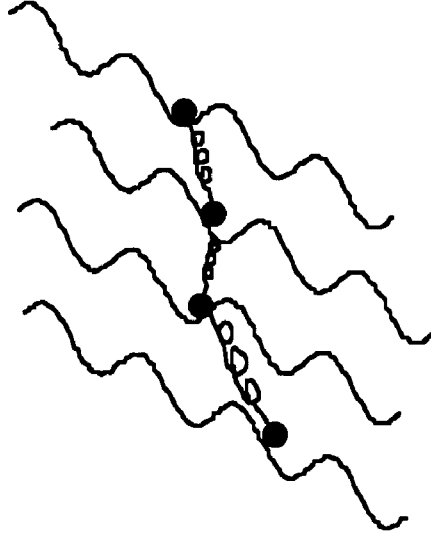


Figure 1.6: Mechanical analogue of the Fukuyama-Lee-Rice model. Balls represent the phase at each impurity site, and springs model the elasticity of the CDW. The washboard interaction arises from the interaction of the CDW with impurities. By tilting the washboard (applying an electric field), one can depin the CDW.

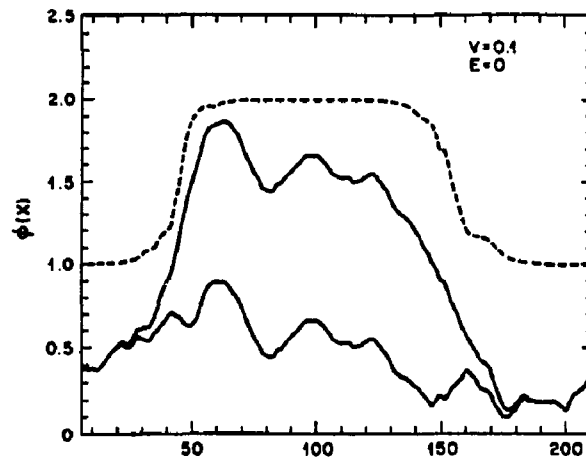


Figure 1.7: Plot of CDW phase ϕ versus position. Two solid lines show two metastable states of the CDW. The dashed line shows the difference of the two states (shifted by one wavelength for clarity). The CDW has advanced by approximately one wavelength in the region $50 < x < 150$ (ref. [14]).

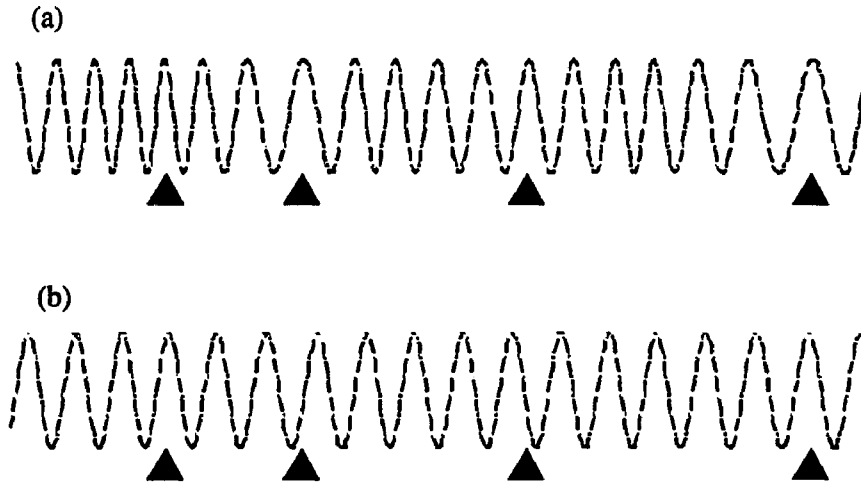


Figure 1.8: Plot of the charge-density in two regimes of pinning. Triangles indicate impurity sites. (a) Strong pinning regime. CDW distorts around each impurity. (b) Weak pinning regime. CDW distorts over the Lee-Rice length λ_{LR} to take advantage of fluctuations in density of pinning centers.

1.4.1 Strong Pinning, Weak Pinning

Aside from the time scale γ_0 , there is really only one other relevant parameter in Eq. 1.24, which is the ratio of the spring force K to the pinning strength V_0 . This ratio is denoted in the literature as $\epsilon \equiv K/V_0$. For $\epsilon \ll 1$, it is much more energetically favorable to align every impurity with an extremum of the CDW, as shown in Fig. 1.8(a). This will happen when the concentration of impurities is small, or if V_0 is small. This is known as “strong” pinning. Note that strong pinning does not necessarily imply that the impurities are strong in any absolute sense. If the concentration is small, then the effective elastic coupling between the phase at two neighboring impurity sites will decrease. In the limit $\epsilon \ll 1$, it is easy to see that the threshold for CDW conduction is $E_T \approx V_0$, which is the threshold for a single degree of freedom.

At the other extreme, $\epsilon \gg 1$, the situation is more complicated. As depicted in Fig. 1.8(b), the impurities are so weak compared to the rigidity of the CDW that the CDW phase is essentially constant over many impurities. However, spatial fluctuations in the number of impurities can be used to lower the energy of the CDW, since regions of few impurities will pin the CDW more strongly. The details of this argument were worked out by Lee and Rice [15]. In the weak-pinning limit, the phase of the CDW is essentially constant over a distance λ_{LR} , known as the Lee-Rice length, and one can think of the CDW as consisting of coupled domains, the length of which is λ_{LR} . It is numerically more efficient

to work in the strong-pinning regime, since there are more Lee-Rice domains. It is widely assumed that the dynamics of sliding CDWs in the weak and strong pinning regime do not differ qualitatively [12]. The Lee-Rice length λ_{LR} is alternately known as the phase-phase coherence length ξ (which is in general anisotropic), which sets the length scale for dephasing of the CDW: $\langle \phi(x)\phi(0) \rangle \sim e^{-x/\xi}$. The transverse correlation length has been measured in NbSe₃ by low-angle X-ray scattering [16], and is on the order of 1 μm . In the conducting direction, the correlation length is estimated to be an order of magnitude larger.

1.4.2 Normal Carriers

In almost all of the known CDW materials, the CDW coexists at finite temperatures with normal carriers which are excited across the gap. In this way, the CDW behaves much like a semiconductor, and the linear ohmic conductivity (not arising from collective motion of the CDW) behaves in an Arrhenius fashion. At finite frequencies, there will be dielectric contributions to the total current. In general, the total current can be written as

$$\mathbf{j}(\mathbf{r}, t) = \epsilon\epsilon_0\dot{\mathbf{E}} + \sigma\mathbf{E} + \rho_c\dot{\mathbf{u}}, \quad (1.25)$$

where ϵ is the dielectric constant, ϵ_0 is the permittivity of free space, and σ is the linear conductivity. The total current is both conserved and incompressible, so that $\nabla \cdot \mathbf{j} = 0$. That the CDW interacts strongly with uncondensed carriers, as can be seen from the fact that the CDW current scales with the linear conductivity above threshold. Fig. 1.9 shows the temperature dependence of the linear and nonlinear currents in the blue bronze K_{0.3}MoO₃. The dashed line in the inset shows the ohmic portion of the conductivity, while the solid line shows the total (CDW plus normal) current versus voltage. The (almost) straight line shows that both the CDW and normal currents are activated. A similar dependence of the dielectric relaxation frequency (corresponding to the “crossover” frequency in a single-degree-of-freedom overdamped oscillator) was observed by Tucker *et al.* At lower temperatures and much higher fields, a second threshold is observed, in which the conductivity changes by more than several orders of magnitude [18]. This second, higher threshold is often hysteretic, as seen in Fig. 1.10. The effects of normal carriers was first investigated in the FLR model by Sneddon, who investigated the corrections due to the presence of normal carriers in the sliding state [20]. Littlewood showed how the interaction of normal carriers could explain the presence of two threshold fields and the scaling of the CDW and normal conductivities in the semiconducting materials. In Fig. 1.11, the total current is shown as a function of the field for various temperatures, using material parameters appropriate to K_{0.3}MoO₃. The crossover from the low-velocity solutions to the high-velocity ones is assumed to occur when the current oscillations occur at such a high frequency that they can no longer be screened by normal currents.

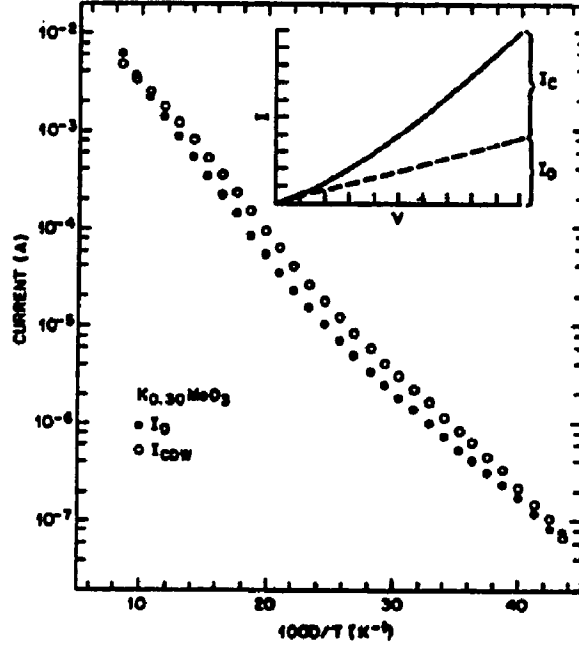


Figure 1.9: Temperature dependence of the linear and nonlinear portion of the current in $K_{0.3}MoO_3$ (ref. [17]).

1.5 Narrow-Band Noise

When the CDW slides over impurities, the current oscillates in time due to the interaction with impurities. The frequency of oscillation is proportional to the time-averaged CDW current, as shown in Fig. 1.12. Such oscillations are known in the literature as “narrow-band noise”. Narrow-band noise was first observed by Fleming [22]. Fig. 1.13 shows power spectra of the voltage across the CDW for various values of the driving current I_{dc} . As the dc current is increased, the narrow-band-noise peak and its harmonics move to higher frequencies.

Narrow-band noise in CDWs is generally believed to be a bulk effect, rather than arising from current conversion (phase slip) at the sample contacts. If narrow-band noise is a bulk effect, then the amplitude of the noise should scale as $N^{-1/2}$ where N is the number of Lee-Rice domains. Experiments generally support this conjecture [23, 24], but there have been studies which suggest otherwise [25]. It has also been suggested that narrow-band noise is generated at the contacts through phase-slip [26].

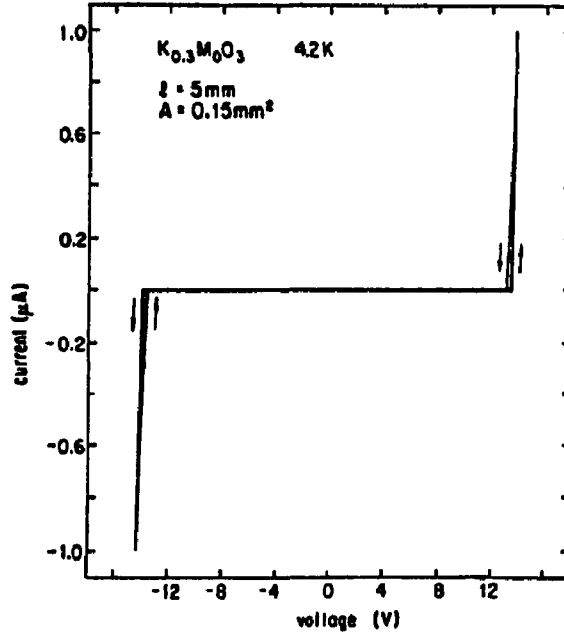


Figure 1.10: Nonlinear conduction in $K_{0.3}MoO_3$ at $T=4.2$ K (ref. [18]).

1.6 Mode-Locking

1.6.1 Mode-locking in Josephson Junctions

Not long after the discovery of narrow-band noise came the idea of applying combined dc and ac fields to the CDW. The expectation was that one might see interference effects similar to those seen in Josephson junctions. In a Josephson junction, a supercurrent J can flow across without any voltage drop, provided that the current is less than a critical amount J_c . Above J_c the voltage increases monotonically. Associated with the increase in voltage is an oscillation whose frequency is proportional to the voltage. This is known as the ac Josephson effect.

The application of microwave fields causes Shapiro “steps” in the observed voltage [27],

$$n\hbar\omega_{ex} = 2eV. \quad (1.26)$$

where ω_{ex} is the microwave frequency, V is the voltage step, and n is an integer. The Josephson steps correspond to mode-locking of the microwave frequency to the Josephson frequency.

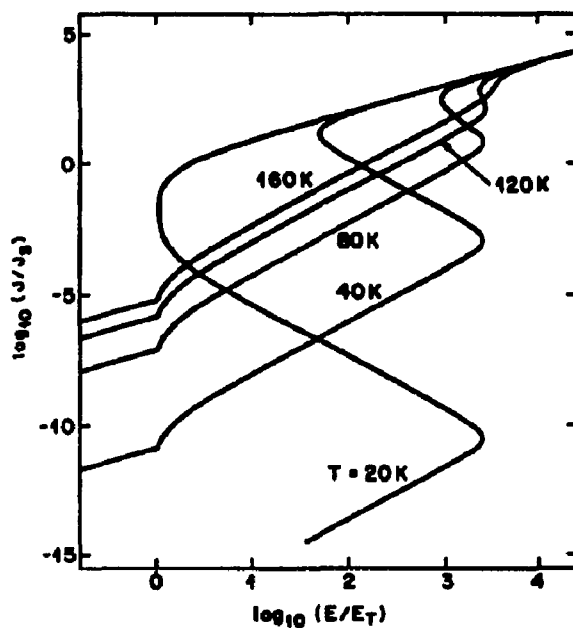


Figure 1.11: CDW I-V characteristic for different temperatures, using parameters appropriate to $K_{0.3}MoO_3$ (ref. [19]).

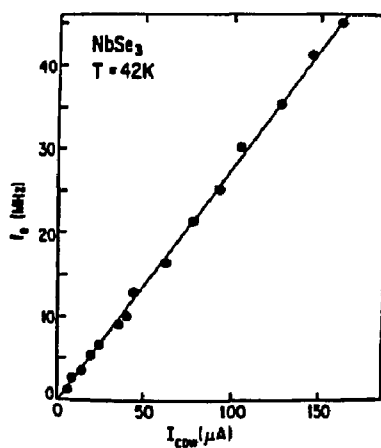


Figure 1.12: Fundamental frequency of the narrow-band noise versus measured CDW current (ref. [21]).

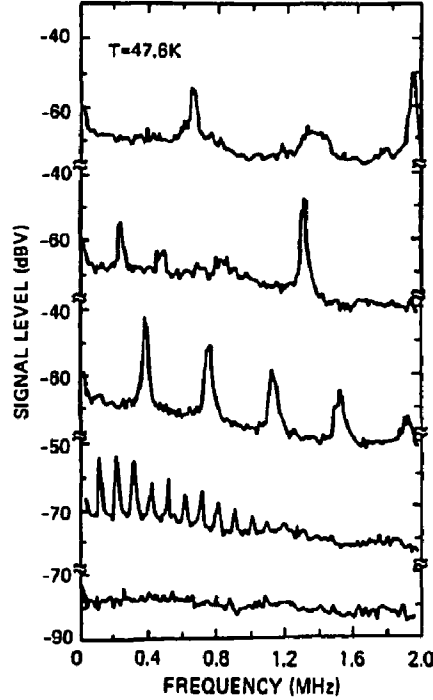


Figure 1.13: Power spectrum of narrow-band noise for various values of the dc driving current I_{dc} (ref. [22]).

1.6.2 Mode-Locking in CDWs

It was quickly realized that a similar type of interference phenomena might be seen in CDWs. In CDWs, the relation between voltage and current are swapped, so that the CDW current I_{cdw} shows a step structure in response to applied radio-frequency fields. As was mentioned in section 1.5, the CDW oscillates with a frequency proportional to its velocity, due to the interaction with impurities. If one applies a time-varying electric field to the CDW,

$$E(t) = E_{dc} + E_{ac} \cos(\omega_{ext} t), \quad (1.27)$$

one can cause the narrow-band-noise frequency ω_{nbn} to “lock” to the external drive frequency if the two are close enough to being commensurate. Such behavior is known as mode-locking, and it occurs generically in nonlinear systems with two competing frequencies. Such interference phenomena was first observed by Monceau in the differential resistance of NbSe_3 as a function of the ac frequency. When the ac frequency became comparable to a multiple of the narrow-band-noise frequency, a peak was observed in the differential resistance.

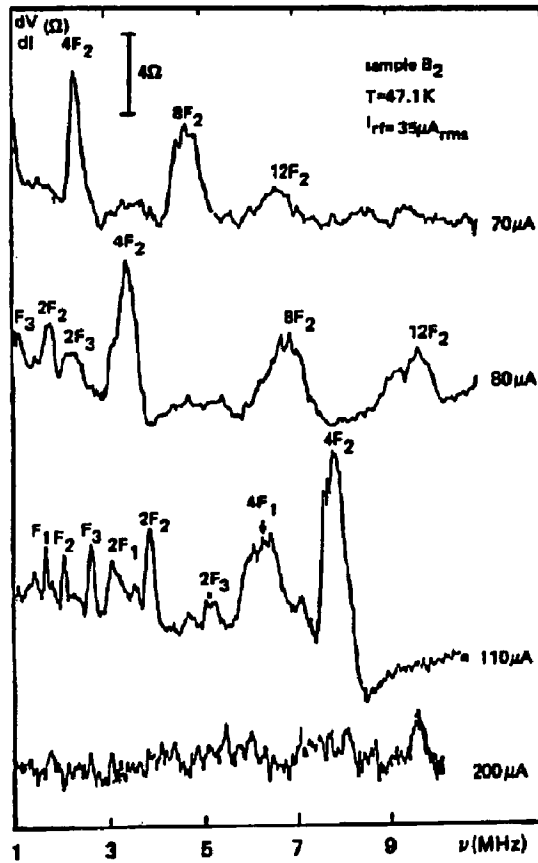


Figure 1.14: Differential resistance in NbSe₃ as a function of ω_{ex} , for various values of the dc bias I_{dc} (ref. [28]).

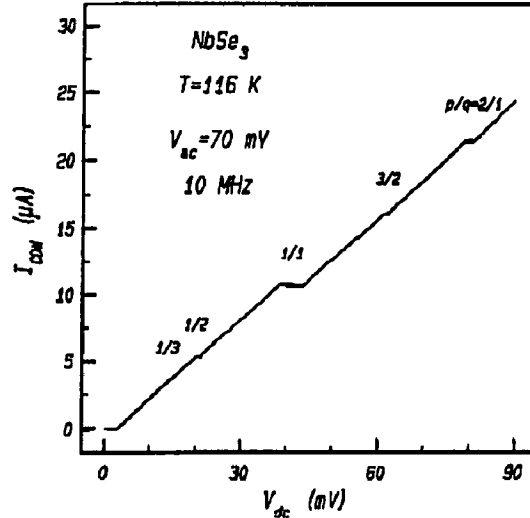


Figure 1.15: Plot of I_{cdw} versus V_{dc} in the presence of ac driving (ref. [7]).

1.6.3 Measurements of Mode-Locking

$I - V$ Curves

There are several signatures of mode-locking in CDWs. If one looks at the $I - V$ characteristics of a CDW, then there will be “steps” at which the CDW current I_{cdw} is constant over a range of voltage. Fig. 1.15 shows a typical $I - V$ curve in the presence of rf fields. Mode-locked steps occur when the ratio of the driving frequency ω_{ex} to the narrow-band-noise frequency ω_{nbn} is sufficiently close to a rational number p/q .

In an ideal, infinite system, these steps are predicted to occur at every rational value $\omega_{nbn}/\omega_{ex} = p/q$ [29]. Such a self-similar structure is called a “devil’s staircase”, presumably because such a staircase would be difficult to climb if one had to land on every step. Fig. 1.16 shows results of a simulation by Middleton of the FLR model in $d = 2$ dimensions driven by square pulses.

Differential Resistance

Such small steps are hard to observe by just looking at $I - V$ curves. Often, one looks at the differential resistance dV/dI , a quantity that is straightforward to measure using lock-in techniques. When mode-locking occurs, the differential resistance of the CDW becomes infinite; uncondensed electrons still contribute to the differential resistance. It is useful to keep a simple two-fluid picture in mind when thinking about mode-locking, as shown in

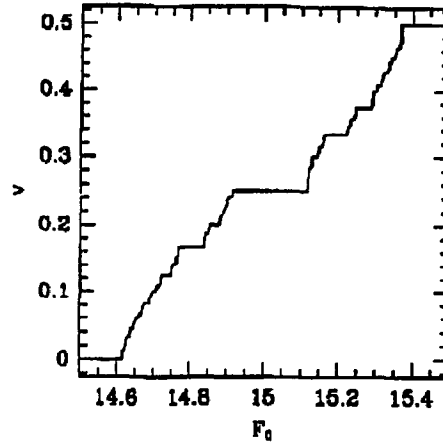


Figure 1.16: Devil's Staircase in response to pulsed driving for Fukuyama-Lee-Rice model in $d = 2$ dimensions (ref. [29]).

Fig. 1.17. Actually, the coupling between the CDW and normal electrons is much more complicated; some of the consequences of this interaction will be discussed in chapter 6.

The interference features show up quite strikingly in the differential resistance, as shown by three examples in Figs. 1.18, 1.19, 1.20. The details of the features vary from sample to sample, but the general phenomena is the same, an increase in dV/dI whenever $\omega_{nbn} \approx p/q \omega_{ex}$. In most samples, such as that shown in Fig. 1.18, only a small fraction of the CDW becomes locked. Some samples exhibit complete mode-locking, but only for the integral ($p:1$) and low-order subharmonic steps such as the 1:2 step. When complete mode-locking occurs, the broadband conduction noise is eliminated, as seen in Fig. 1.19. Vanishingly few samples exhibit a large number of subharmonic steps. Such samples invariably have uniform cross sections and a much lower amount of broadband noise [30] (see section 2.2.2). Fig. 1.20 shows such a sample. The mode-locked steps are flanked by negative "wings", which are indicative of frequency pulling of ω_{nbn} toward ω_{ex} .

Power Spectra

Another way to probe the dynamics of the mode-locked state is to look at power spectra. It is difficult to look at power spectra near the integral mode-locked steps, because of interference with the driving frequency and harmonics. Therefore, interest has centered on behavior near or at subharmonic steps. In the absence of ac driving, the narrow-band noise has a natural width (which is often sample dependent). This width narrows significantly when mode-

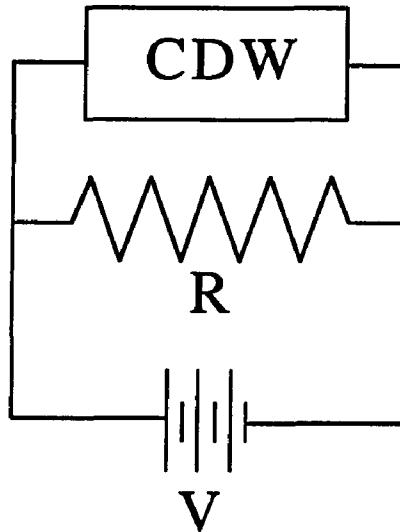


Figure 1.17: Simple two-fluid picture of CDW and Ohmic conductivity. $dV/dI = R$ in the pinned and mode-locked state.

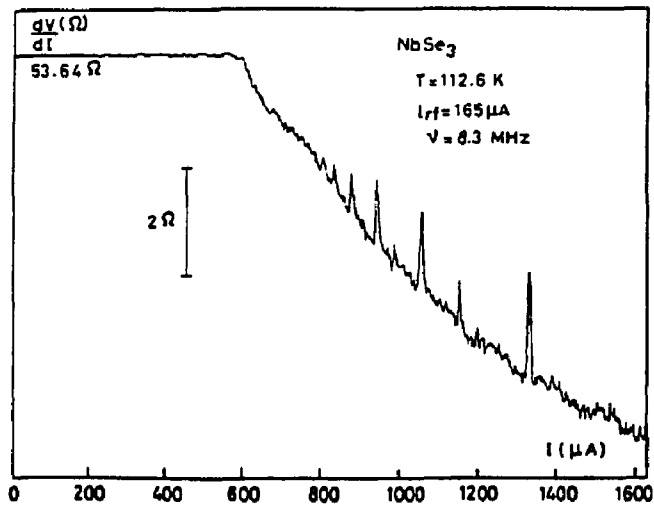


Figure 1.18: Differential resistance dV/dI in the upper transition of $NbSe_3$ (ref. [31]).

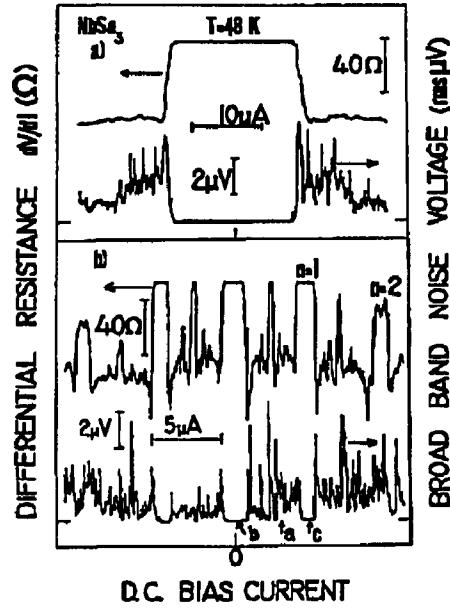


Figure 1.19: (a) Top trace shows differential resistance dV/dI as a function of the dc bias current in the absence of ac driving. Bottom trace shows amplitude of the measured broadband noise. The noise is negligible in the pinned state. (b) Top trace shows dV/dI in the presence of ac driving. Complete mode-locking occurs when dV/dI reaches its ohmic value. Bottom trace shows the magnitude of the broadband noise. Note that when complete mode-locking occurs, the broadband noise vanishes (ref. [32]).

locking occurs. Fig. 1.21 shows an example of such a narrowing. This narrowing during mode-locking indicates that the CDW velocity is highly coherent. Fisher, who had proposed that the CDW depinning transition was an example of a dynamical phase transition [35], has suggested that the magnitude of the narrow-band noise amplitude in the harmonically mode-locked state should scale with the dynamic velocity-velocity correlation length ξ as

$$\frac{\langle j_{ac}^2 \rangle^{1/2}}{j_{dc}} \sim \left(\frac{\xi^d}{V} \right)^{1/2}, \quad (1.28)$$

where V is the volume of the crystal. The correlation length ξ diverges as the mode-locked state is approached. As was mentioned earlier, power spectrum measurements cannot distinguish between the narrow-band noise and the drive signal, so relation 1.28 cannot be verified in this manner.

Relation 1.28 does not hold for the subharmonic mode-locked steps. The amplitude of the current oscillations are not enhanced during subharmonic locking. While the narrow-

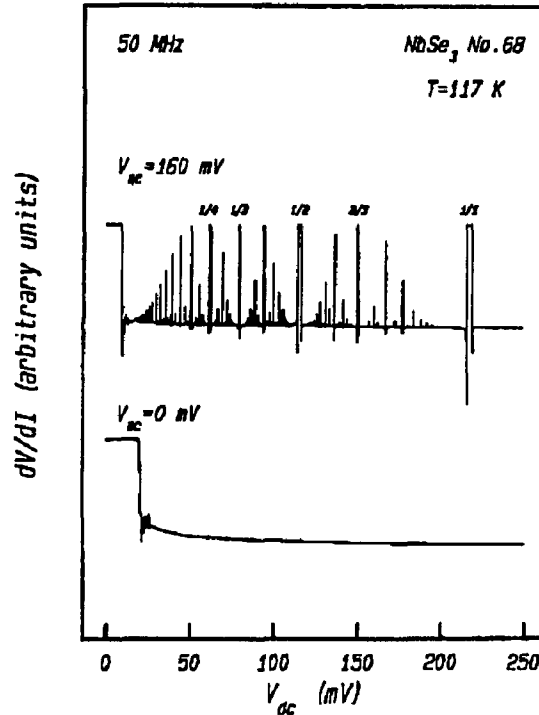


Figure 1.20: Differential resistance in the presence (top trace) and absence (bottom trace) of 50 MHz rf driving. The quality of the crystal is indicated by the presence of more than 150 subharmonically mode-locked steps (ref. [33]).

band-noise peak becomes instrumentally narrow during mode-locking, fluctuations in the amplitude increase dramatically [36, 37]. Fig. 1.22 shows a histogram of the narrow-band-noise amplitude in the 1:2 mode-locked state, and in the absence of ac driving. For large amplitudes of ac driving, the amplitude can remain fixed for minutes [36], giving rise to the different peaks in the histogram.

Fluctuations can also cause intermittent jumping between mode-locked states with different $p : q$ ratios, although this generally occurs with samples which have a large broadband noise [38]. Fig. 1.23 shows a histogram of the narrow-band noise when the CDW is biased slightly away from the 2:3 mode-locked step. The intermittent locking reflects the fact that the mode-locked attractors are preferred to unlocked states, and that lower order rational values of the ratio $\omega_{\text{nbn}} : \omega_{\text{ex}}$ are more attracting than higher order rationals.

Wiesenfeld and Satija have studied the noise tolerance of frequency-locked dynamics [39]. Although the true dynamics of a system may be high-dimensional, one can often treat the

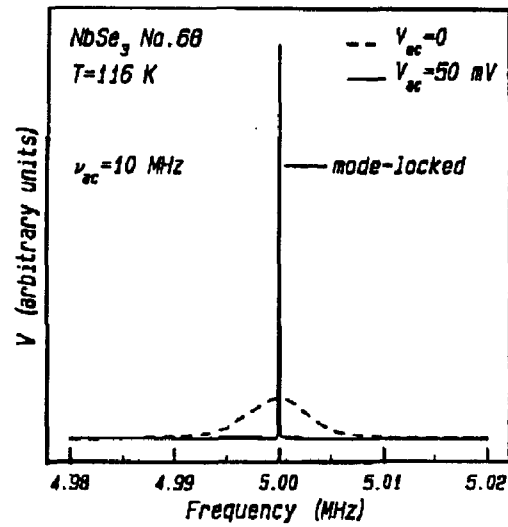


Figure 1.21: Power spectrum of narrow-band noise in the absence (dashed line) and presence (solid line) of ac driving. The mode-locked peak becomes instrumentally narrow during mode-locking (ref. [34]).

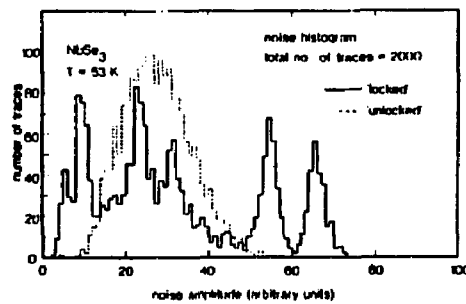


Figure 1.22: Histogram of narrow-band-noise amplitude in the locked and unlocked state (ref. [36]).

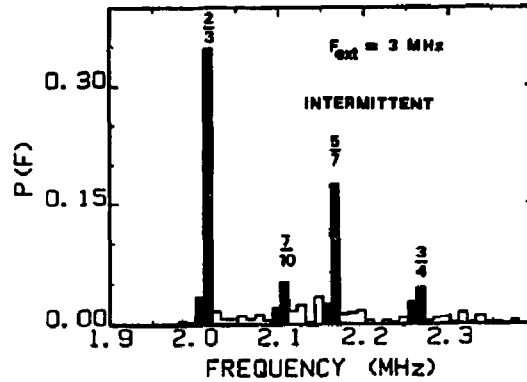


Figure 1.23: Histogram of ω_{nbn} for sample which displays intermittent mode-locking behavior. The sample is biased slightly above the $p : q = 2 : 3$ step (ref. [38]).

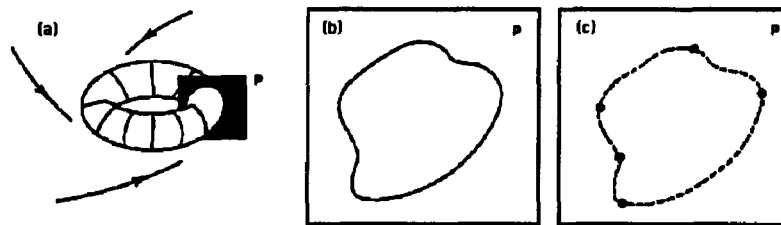


Figure 1.24: (a) Phase-space attraction toward an invariant 2-torus. The intersection of trajectories with the plane P induces an iterative map of the circle onto itself. (b) Quasiperiodic dynamics fill the points on the circle. (c) When mode-locked dynamics occur, the attractor is reduced to a finite number of points (q points for $p : q$ locking) (ref. [39]).

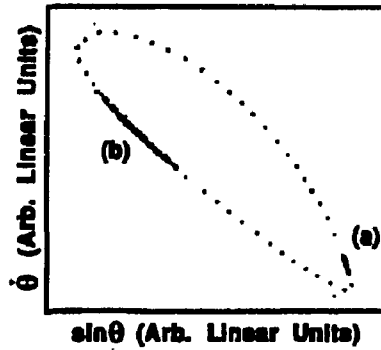


Figure 1.25: Poincaré section of the Josephson junction simulator in the 5:2 mode-locked state. Two noisy fixed points are shown, superimposed upon a dotted curve which represents a nearby quasiperiodic orbit. The noise drives the attractor away from the fixed point mainly in the direction of the quasiperiodic orbit (ref. [40]).

system as lying on the surface of an N -torus, where $N=2$ for a system with two competing frequencies. Fig. 1.24(a) shows a schematic of such an attractor in phase space, where the dynamics are attracted onto a 2-torus. With such an attractor, it is sufficient to know the map which takes trajectories from one intersection of the plane P to a successive intersection, known as the Poincaré section. If the dynamics are strongly attracted to the surface of the torus shown in Fig. 1.24(a), then the locus of points which cross P will be topologically equivalent to a circle, as seen in Fig. 1.24(b). When $p : q$ mode-locking occurs, the attractor is reduced to q points, shown in Fig. 1.24(c).

The theory of Wiesenfeld and Satija suggested that the increase in broadband noise near the edge of a mode-locked step is consistent with the dynamics of a fixed point which is constantly being kicked away by white noise. To test experimentally this hypothesis in a controlled fashion, Crommie *et al.* studied a mode-locked Josephson junction simulator driven by white noise [40]. Fig. 1.25 shows a Poincaré section of the Josephson junction simulator in the 5:2 mode-locked state. The dotted lines indicate a nearby unlocked attractor. Crommie *et al.* found an excellent quantitative agreement between the theory and experiment, although the high-frequency dynamics were influenced by degrees of freedom associated with relaxation onto the circle, as can be seen from the power spectrum shown in Fig. 1.26.

The nonlinear system with two interacting frequencies is reduced to the study of a one-dimensional map of the circle onto itself [41]. The canonical map is known as the circle

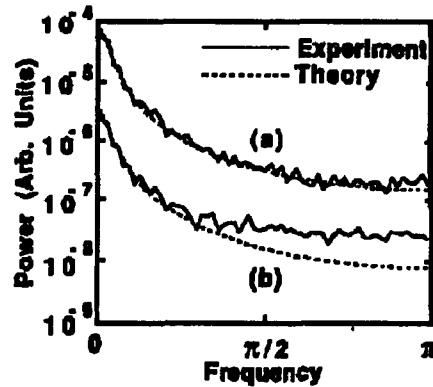


Figure 1.26: Predicted (solid line) and measured (dashed line) power spectrum of the angular coordinate of fixed points a (a) and b (b) shown in Fig. 1.25. The deviation in (b) between experiment and theory at high frequencies comes from fast relaxation onto the circle not accounted for by the theory of Wiesenfeld and Satija (ref. [40]).

map:

$$\theta_{n+1} = \theta_n + \Omega + \frac{K}{2\pi} \sin(2\pi\theta_n) \quad (1.29)$$

For values of K less than $K = 1$, Eq. 1.29 is invertible, and the map exhibits both locked and unlocked behavior. The phase diagram is usually displayed as shown in Fig. 1.27. The boundaries of the various mode-locked regions are drawn in solid lines, and the regions are called “Arnold tongues”. The critical line $K = 1$ separates a region which still has unlocked solutions from a region in which there is overlap; on the critical line itself the set of points which are unlocked is fractal [44, 45, 46].

Well into the non-invertible regime, Eq. 1.29 exhibits a period-doubling route to chaos. Mode-locking experiments performed at lower temperatures showed period-doubling and chaos [47], and so it was believed that both the mode-locking and chaotic behavior could be described by a simple one-dimensional map [48].

1.7 Switching

At temperatures near the CDW transition, the CDW depins at a unique threshold field E_t . As the temperature is lowered, a second threshold E_t^* develops, and the threshold field often becomes hysteretic. The size of the hysteresis increases as the temperature is lowered still further. Such behavior has been seen in all materials, although not in all samples. In NbSe_3 , hysteresis can be induced by quenching [49] and Fe doping [50], and freshly-grown

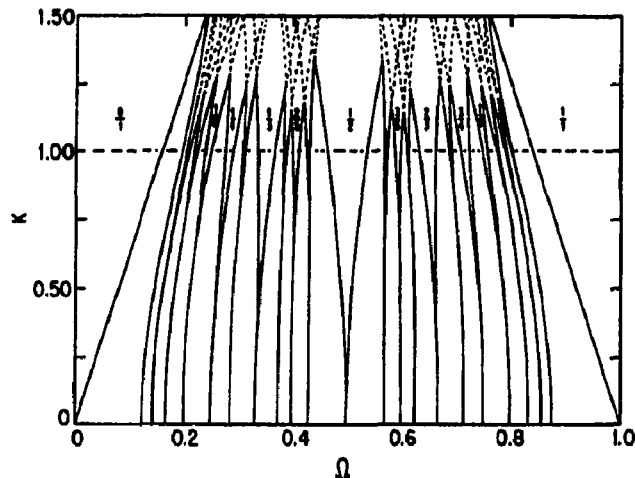


Figure 1.27: Arnold tongue diagram depicting mode-locked intervals in the circle map Eq. 1.29 as a function of Ω and K (refs. [41, 42, 43]).

batches almost invariably show switching behavior, whereas batches aged over a period of months do not [51].

Switching in NbSe_3 is associated with a host of phenomena not observed in the non-switching regime, such as hysteresis [53], negative differential resistance [54], anomalously large broadband noise [52], delayed conduction [53, 55], and period-doubling routes to chaos [47]. While many of the unique features of sliding CDWs had been successfully accounted for by the classical Fukuyama-Lee-Rice model, none of the features associated with switching could be accounted for. Several attempts have been made to understand switching behavior in NbSe_3 in terms of phase slip [56], CDW inertia [47], and other processes [57]. Of the mechanisms proposed, phase slip seemed the most promising. Models which include phase slip were proposed by Inui *et al.* [56], and Marcus, Strogatz and Westervelt [58]. These models exhibited hysteresis, delayed conduction, and a period-doubling route to chaos.

Two distinctive features of switching behavior are relevant to this thesis: delayed switching and chaos in ac-driven switching samples. These two phenomena will be discussed briefly in the following two sections.

1.7.1 Delayed Switching

In investigating the properties of switching samples, Zettl and Grüner noticed that if one applied a voltage pulse above threshold, the CDW does not slide immediately, but only after a delay [53]. Fig. 1.29(a) shows the sample voltage as a function of time in response

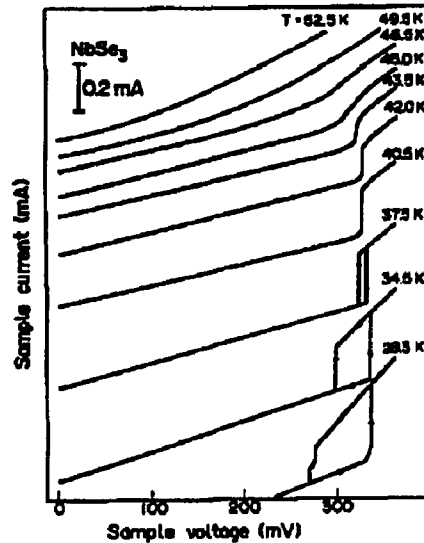


Figure 1.28: Current-voltage curves in NbSe_3 as a function of temperature. As the temperature is lowered, the hysteresis develops (ref. [52]).

to a square current pulse. The CDW remains pinned until a time T , after which the CDW begins to slide. Fig. 1.29(b) shows the voltage before and after the switch as a function of the current pulse height. The delay decreases as the height of the pulse increased above threshold. This delayed conduction has been observed in NbSe_3 [53] and in $o\text{-TaS}_3$ [55], and appeared to be an intrinsic and distinctive feature of switching. Fluctuations in the switching delay for fixed bias were also observed. A distribution of switching delays was obtained by differentiating the average of many pulses (see Fig. 1.30). It was observed that the distribution of switching delays could be fit to a Lorentzian whose width increased as threshold was approached.

1.7.2 Mode-Locking and Chaos

The behavior of switching samples in the presence of ac driving is quite different from the non-switching regime. Instead of observing both locked and unlocked behavior, the CDW appears to be mode-locked always in integral mode-locked steps. Fig. 1.31 shows I-V curves in the presence of 15 MHz ac driving for various strengths of the driving field. The Shapiro steps indicate that the CDW is always mode-locked on an integral ($p:1$) step.

Chaotic behavior is also observed in the presence of combined dc and ac fields. Evidence for chaotic behavior comes from measurements of power spectra [48], where a period-doubling route to chaos is observed (see Fig. 1.32). At lower ac driving frequencies, a

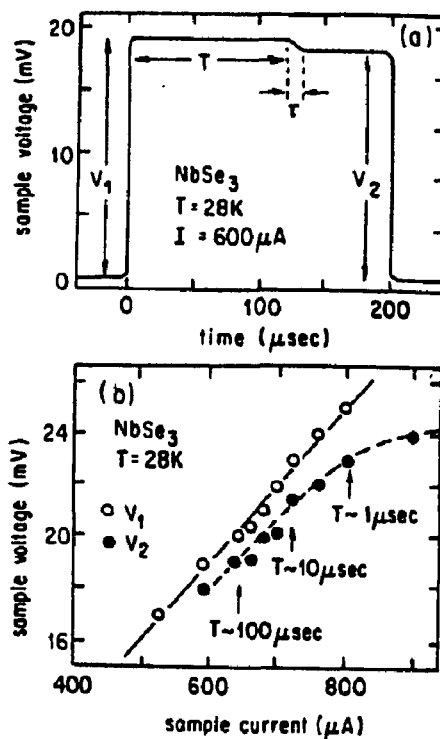


Figure 1.29: (a) Digitally smoothed response waveform to a current pulse with I just above I_T . The switching phenomena is clearly seen at a time $120 \mu\text{s}$ from the start of the pulse. Identified in the figure are the voltages V_1 and V_2 (corresponding, respectively, to the non-conducting and conducting states), the time before switching T , and the switch duration τ . (b) $I - V$ curves obtained from pulse measurements similar to the one shown in (a), where the voltages V_1 and V_2 are defined. The full line is the Ohmic conductivity, while the dotted line is a guide to the eye for the nonlinear conductivity. Typical values of the time to switch T , for a given sample current I , are also shown (ref. [53]).

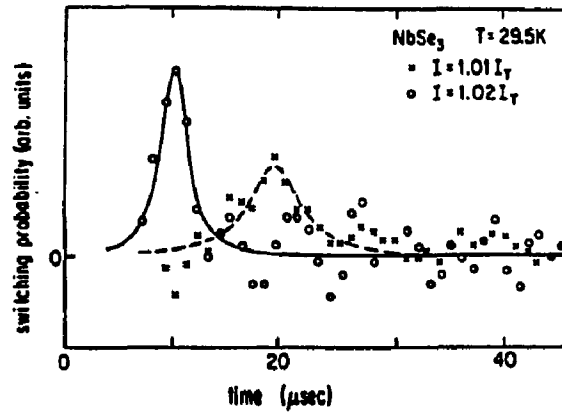


Figure 1.30: Distribution of time to switch T for two different driving currents I . The full line is a fit to a normalized Lorentzian distribution. The width for the dashed line is approximately twice that for the solid line (ref. [53]).

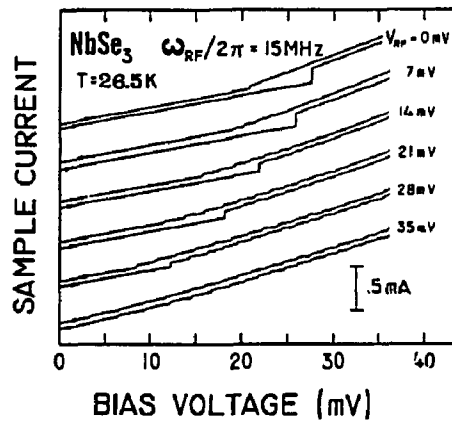


Figure 1.31: Current-Voltage traces in the presence of 15 MHz sinusoidal ac driving for various values of the ac amplitude. Traces where voltage is swept up and down are offset slightly for clarity (ref. [52]).

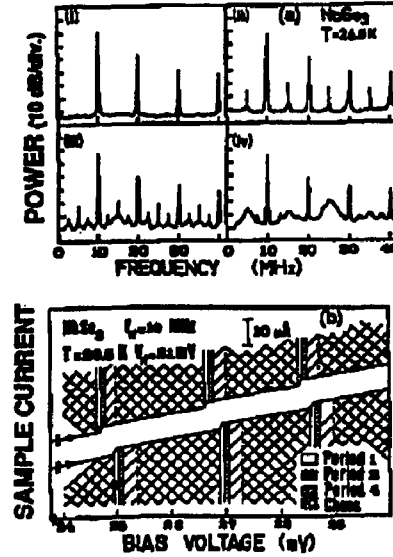


Figure 1.32: (a) Power spectra of the current response in the Shapiro step region of a sample of NbSe_3 . External rf drive frequency and amplitude as in (b). (i) $V_{\text{dc}} = 25 \text{ mV}$, period 1; (ii) $V_{\text{dc}} = 25.1 \text{ mV}$, period 2; (iii) $V_{\text{dc}} = 25.2 \text{ mV}$, period 4; (iv) $V_{\text{dc}} = 25.5 \text{ mV}$, chaos. (b) Schematic representation of the periodicity of the current response in the Shapiro-step region for the sample, for forward- and reverse-bias voltage sweeps (ref. [48]).

broadband chaotic response was observed similar to the broadband noise seen in absence of ac driving, but roughly 10 dB larger in magnitude (see Fig. 1.33). The origin of the noise was attributed to fluctuations in the switching delays (see Sec. 1.7.1).

1.8 What's Ahead

This thesis focuses on the study of the many fascinating dynamical properties of CDWs. In a broad sense, the aim of this thesis is to address and explore two related questions:

- How can recent advances in the field of nonlinear dynamics be applied toward understanding the physics of sliding CDWs?
- How can the physics of sliding CDWs provide insight into the dynamics of overdamped spatially-extended systems with quenched disorder?

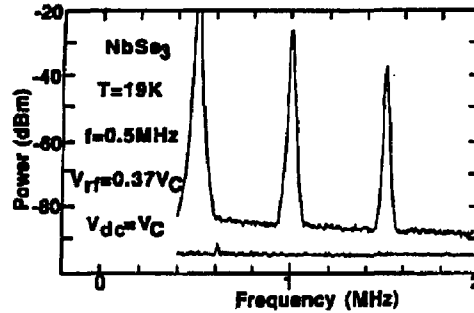


Figure 1.33: Power spectrum of CDW current in the presence (top trace) and absence (bottom trace) of $f = 0.5$ MHz rf driving. Peaks in the power spectrum indicate the rf driving and harmonics due to the response of the CDW. There is an anomalously large broadband noise associated with the ac-driven dynamics (ref. [48]).

The symbiotic relation between CDWs and the burgeoning field of nonlinear dynamics should become apparent as you read (or skim) this thesis.

Chapter 2 describes the experimental methods used in the experiments performed for this thesis. Chapter 4 presents time-domain measurements of mode-locking in non-switching NbSe_3 . In chapter 3, I describe initial experiments involving delayed conduction in switching NbSe_3 . Chapter 4 describes time-domain measurements of mode-locking non-switching CDWs in the presence of combined sinusoidal ac and dc currents. Chapter 5 describes experiments on time-domain measurements of chaos in switching NbSe_3 . In Chapter 6, a unified model of switching and non-switching CDW dynamics is presented. A comparison between predictions of this model and further experimental study of delayed conduction in switching NbSe_3 is presented in chapter 7.

Enjoy!

Chapter 2

Experimental Methods

I will now describe the experimental methods employed in this thesis. Several methods are common to all experiments, while others are specific to a particular set of experiments.

2.1 Cryostats and Temperature Control

All of the experiments in this thesis were performed on samples of the CDW conductor NbSe_3 , in the lower CDW transition at temperatures below the Peierls temperature $T_{P2} = 59$ K. The samples were cooled using a CTI Cryogenics Model 22 closed-cycle helium refrigerator with a zero-load base temperature of 8 K.

2.1.1 First Set-Up

In the first set-up, the samples were mounted inside a 1 1/3 in. conflat flange filled with 1 atm. helium gas (see Fig. 2.1). The bottom half of the flange was secured to the closed-cycle refrigerator coldhead. The samples were sealed inside in order to minimize the effects of heating. Electrical feedthroughs were constructed by epoxying eight gold-plated IC socket pins through one half of the flange, using Stycast 2850 epoxy. Samples were mounted across 0.001 in. gold wires using silver paint to make electrical contact.

Each of the four sample feedthrough pairs were connected by a twisted pair of wires leading out of the cryostat. A simple bridge circuit was used to subtract the ohmic response of the sample. For high-impedance samples, a voltage-driven set-up was used, as shown in Fig. 2.2(a). For low-impedance samples, a current-driven set-up was used, shown in Fig. 2.2(b). The switching samples used in the experiments described in Ch. 3 were typically small and thin, with large (~ 1 k Ω) impedances. Non-switching samples can have much lower impedances (≤ 100 Ω). Two diodes were used for temperature control and measurement. One diode was fastened near a 1/2 in. thick Cu disk that was sandwiched between the cold

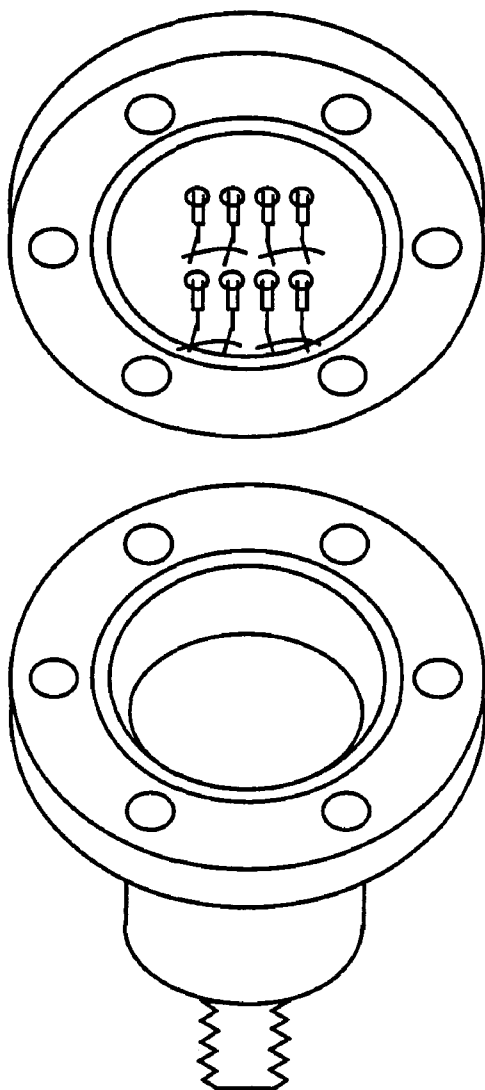


Figure 2.1: Schematic drawing of sample mount and housing.

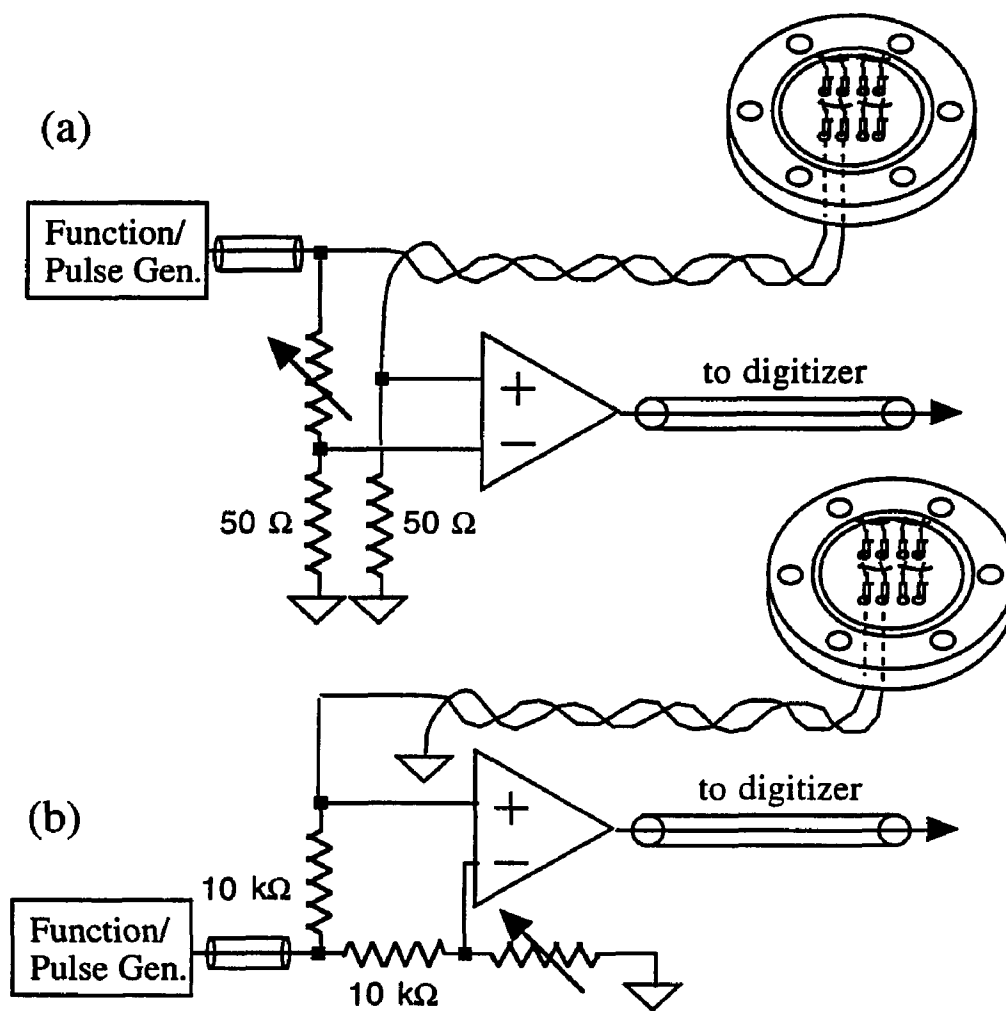


Figure 2.2: (a) Set-up for performing voltage-driven measurements on high-impedance samples. (b) Set-up for performing current-driven measurements on low-impedance samples.

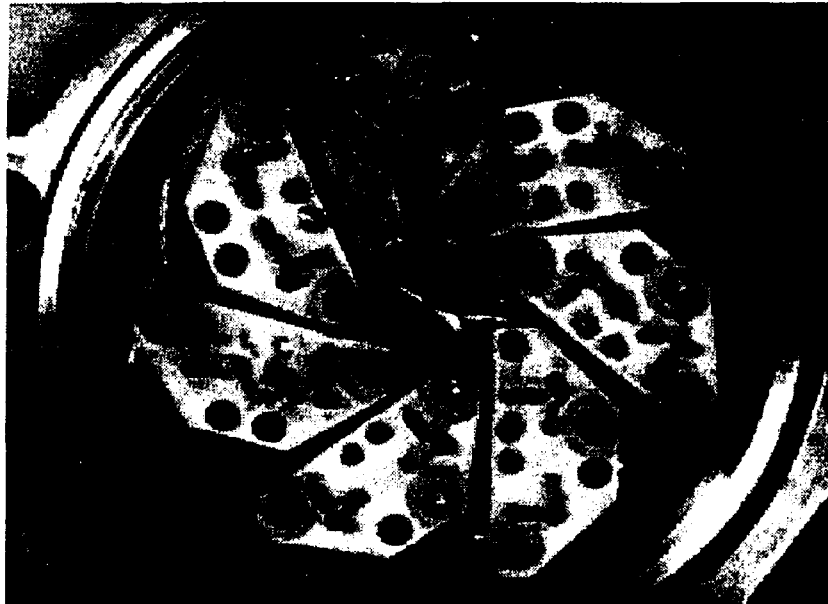


Figure 2.3: Photograph of 4 1/2 in. conflat flange used for mounting samples.

head of the refrigerator and the conflat flange. A $50\ \Omega$ heater was embedded inside the copper disk, next to which another diode was attached, for controlling the temperature.

2.1.2 Second Set-Up

The first set-up, while adequate for most experiments, had several undesirable features:

- The twisted pairs did not form a $50\ \Omega$ transmission line, and ac signals had to be calibrated at different frequencies. In fact, large resonances often appeared at frequencies as low as 10 MHz.
- Because of imperfect shielding, the twisted pairs were highly susceptible to rf pickup.
- The BNC connectors needed to be isolated from ground, making ground loops more difficult to eliminate.
- Only three samples could be examined at a given time.

In later experiments, an improved sample holder and cryostat were built which overcame many of the disadvantages of the first set-up. The new sample holder was constructed out of a 4 1/2 in. conflat flange, with 14 $50\ \Omega$ SMA feedthroughs, shown in Fig. 2.3. One feedthrough was used to send current to an internal heater; another was used to measure

the voltage across a temperature-sensing diode. Twelve feedthroughs were left for sending signals to and from six samples. Stainless steel 0.85 in. diameter semi-rigid coaxial cables were used to make connections outside the cryostat. Samples were mounted on a ceramic microstripline in a voltage-driven configuration (see Fig. 2.3). Signals were terminated at one end of the sample with a $50\ \Omega$ resistor, and the current through the CDW sample was measured via the voltage across another $50\ \Omega$ resistor.

The second set-up had many improvements over the first one:

- Signals were transmitted and received via $50\ \Omega$ transmission lines, yielding reproducible and resonanceless response from dc to beyond 500 MHz.
- Because signals were shielded, rf pickup was almost completely eliminated.
- Six samples could be examined during a single cycle.
- Because of the large thermal mass, temperature stability was greatly improved.

To further improve the temperature stability, two temperature controllers were employed. One diode and heater were placed close to the cold head, to minimize long-timescale fluctuations in cooling power that inevitably occur in closed cycle helium refrigerators. The second diode and heater were placed inside the He chamber, to control and measure the temperature on a much finer scale. Because of the He atmosphere, the temperature inside the chamber was to good approximation spatially uniform. Because of the symmetric positioning of the samples and diode, it is reasonable to assume that the temperature of the sample was the same as the diode temperature.

2.2 Sample Growth and Preparation

2.2.1 Crystal Growth Procedure

Samples of NbSe_3 were grown by conventional vapor transport methods.¹ Stoichiometric ratios of Nb and Se were combined in a quartz tube and sealed under vacuum. The tube was then heated to allow the elements to react and form amorphous NbSe_3 . The tube was then placed in a three zone furnace and heated to 900 K from one end for a period of 12 hours, so as to “chase” the material to the other end of the tube. Then, the temperature gradient was reversed so that the material-rich end was at 660–670 K, and a constant temperature gradient of 20 K was maintained from one end of the tube to the other. Growth typically took place over a period of 10–15 days. The quartz tube was then allowed to cool for a period of 1–2 days, and then removed.

¹All samples used in this thesis were grown by Neil Nighman.

Because of the central role impurities play in determining the electrical properties of CDW materials such as NbSe_3 , special care was taken to ensure that the starting materials, especially Nb, be as pure as possible. Tantalum is the most important impurity in nominally pure Nb, so starting materials were found which had less than 2ppm Ta. However, it has been shown by Thorne [10] that oxygen getters impurities, including Ta, eliminating the need for ultrapure starting materials.

2.2.2 Mounting Samples

The mounting of samples is an acquired skill, and is one which does not translate easily onto the printed page. Special care must be taken in handling samples, for it is easy to introduce strain defects by bending them. Often the samples are quite thin, which makes them more difficult to handle. Because so few samples are of high enough quality to do measurements on, a great deal of time is spent finding suitable samples. The following is a list of features to avoid when looking for crystals:

- Gross thickness steps in the cross section. Such features were shown by Maher et. al (find reference) to produce large broadband noise features and multiple narrow-band noise peaks in power spectra measurements.
- “Split-end” crystals. If a crystal is split at one end, chances are that there is a large thickness step, or some other gross imperfection in the crystal.
- Crystals which diffract light under point source illumination.² This is an indication of there being many microscopic steps which actually form a diffraction grating. Such features almost invariably mean that the sample will have a low-Q narrow-band noise.
- Large, thick crystals. Such crystals almost invariably have many grain boundaries, and are useless for most of the experiments described in this thesis.

Having said all that, one might reasonably ask if it is at all possible to find a high-quality crystal. There are other ways of finding out whether a particular crystal may be suitable for measurements. One way is to take scanning electron micrographs (SEMs) of particular crystals within a batch of grown crystals, isolate a desired crystal, mount it, cool it, and measure power spectra. However, there are many pitfalls along the way from finding the crystal under the SEM to measuring power spectra, and the yield is quite low. Nevertheless, by this method one can screen out crystals which have any of the undesirable qualities itemized above. Fig. 2.4 shows a picture of two crystals, one with many thickness steps, and the other without any visible imperfections. The SEM resolution is limited by the fact that the crystal is not well-supported physically, and vibrates easily. Fig. 2.5 shows

²This feature was pointed out to me by Robert Thorne.

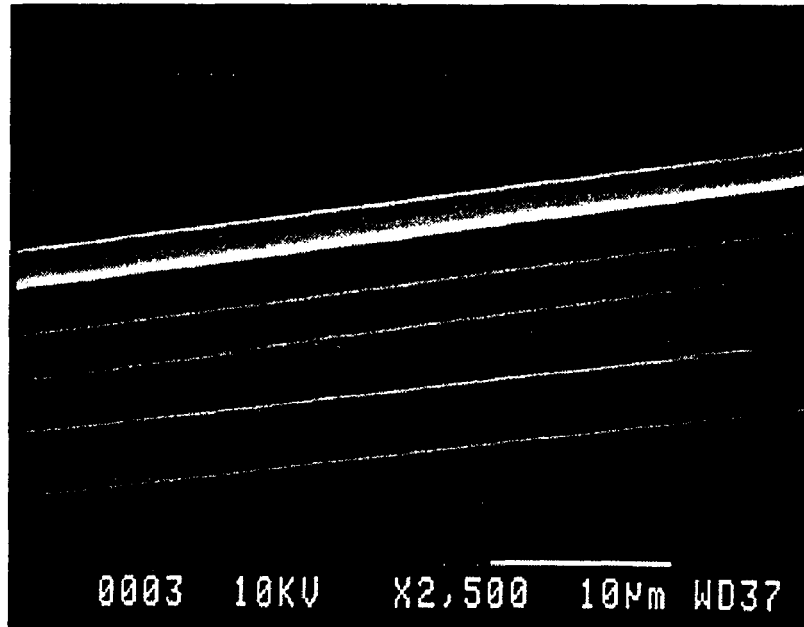


Figure 2.4: Scanning electron micrograph of two crystals of NbSe₃.

a close-up of a highly promising sample. Once a promising sample is found under the SEM, more photographs are taken at successively lower magnifications in order to locate the crystal under an optical microscope. Locating the sample optically is not a straightforward task, because the contrast provided by the secondary electrons may bear little resemblance to the contrast provided by visible light. Unfortunately, the sample shown in Fig. 2.5 got "eaten up" by a giant blob of silver paint when I tried to secure it to the microstrip line.

Fig. 2.6(a) shows a low-magnification SEM picture of the sample used in the mode-locking experiments described in Ch. 4. Fig. 2.6(b) shows a close-up of the sample. While there appear to be surface imperfections, the cross section is quite smooth. The uniformity of the cross section is certainly correlated with the high-Q ($\sim 30,000$) of the narrow-band noise measured in power spectra. The samples are particularly sensitive to heating, and can be damaged by excessive dc or ac applied electric fields. The danger is much greater if the sample is current driven, because of the potential for thermal runaway. Such was the case with the sample shown here. Fig. 2.7 shows a localized portion of the sample which melted as a result of too large of an ac drive. Surprisingly, the sample still performed better than most crystals with thickness steps. This result indicates that defects localized along the length of a crystal have a much smaller effect than do steps, which are more extended defects.

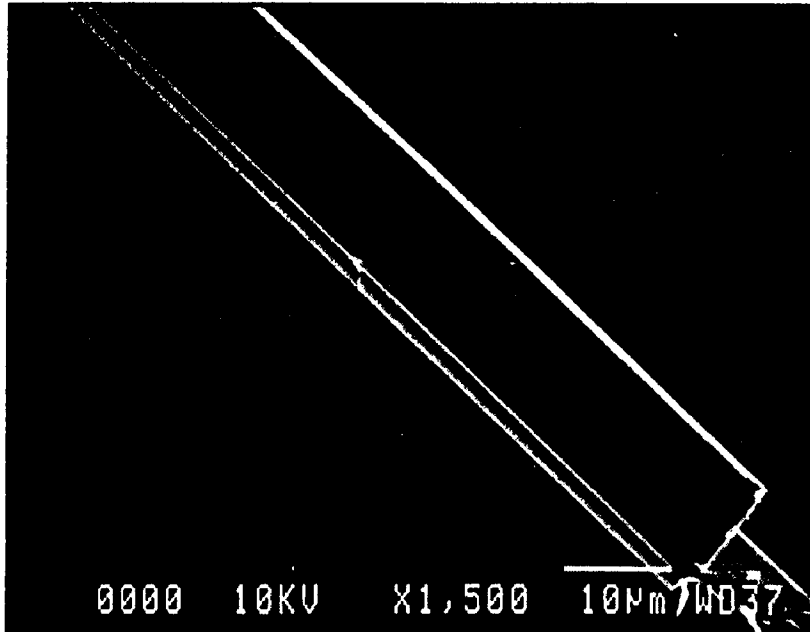


Figure 2.5: Scanning electron micrograph of a crystal of NbSe_3 with a fairly uniform cross section.

2.3 Electronics

Most of the experiments involved the extraction of small signals from large backgrounds, so it is worth some discussion. For the experiments involving delayed conduction (Ch.3-7), the setup shown in Fig. 2.2 was adequate. The experiments involving combined dc and ac driving required more involved methods of subtraction. Fig. 2.8 shows a schematic of the method used to measure the signals in real time. A $50\ \Omega$ rf source was split using a 6dB splitter. Part of the signal was combined with a dc source using a unity gain follower. The output of the follower was used to drive the sample. The sample output was amplified by a Miteq AU-1310 low-noise preamplifier with a noise figure < 1.45 dB and a bandwidth of 10 kHz–500 MHz. The signal was further amplified by two 13 dB Avantek GPD-1061 amplifiers, and fed into one input of a Tektronix P6046 differential amplifier probe. The other part of the rf signal was split again. One component of the split signal was converted to ECL logic levels, and delayed using a ECL delay line. The delayed ECL signal was used to clock a Tektronix RTD710 digitizer exactly once per drive cycle at any specified phase. The other component of the split ac signal was delayed using an analog delay line, attenuated, and fed into the other input of the differential amplifier. The attenuation and delay line

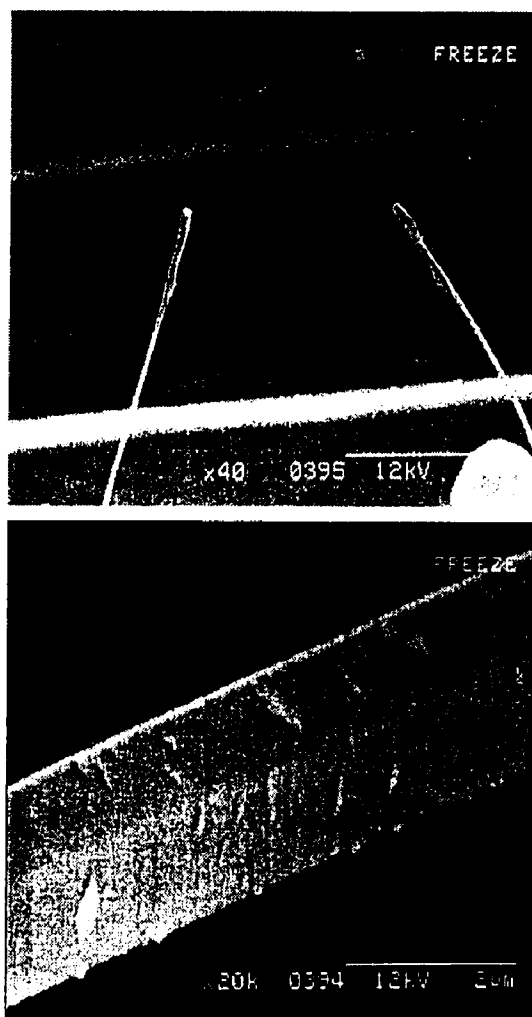


Figure 2.6: (a) Scanning electron micrograph of the crystal of NbSe_3 used in the mode-locking experiment described in Ch. 4. (b) Close-up of same crystal.

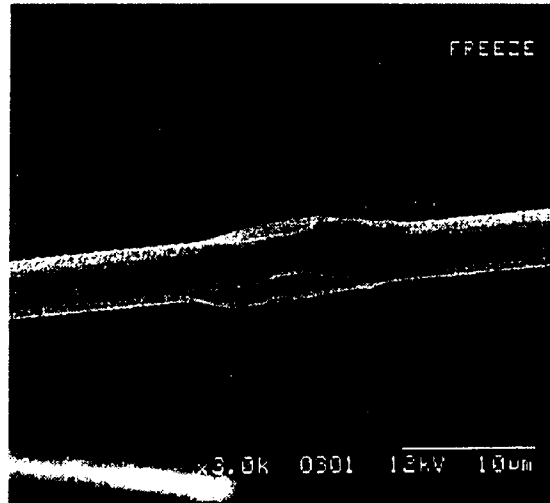


Figure 2.7: Close-up of the portion of the crystal shown in Fig. 2.6 which melted as a result of too large an applied ac drive.

allowed both the amplitude and phase of the linear response of the CDW to be subtracted. The subtraction was essential for bringing the signals within the range of the digitizer.

2.4 Noise Reduction

Along with high-speed electronics, it is essential to reduce all sources of noise. For the real-time measurements, one cannot use standard techniques of reducing noise, e.g. lock-in techniques, signal averaging, filtering. The main sources of noise for these experiments were the following:

- Line-cycle noise (60 Hz and harmonics).
- Radio-frequency noise (radio stations).
- Digital noise (from displays, CRTs, computers, computer clocks, etc.).
- Amplifier noise.

Various techniques were used to combat these sources of noise. Line-cycle noise was usually the result of a ground loop in the circuit, and could be eliminated largely by filtering inputs (not outputs!), and using coax-wound baluns to shunt the ground loops. Improper grounding of electronic instruments could also result occasionally in line-cycle noise. Making

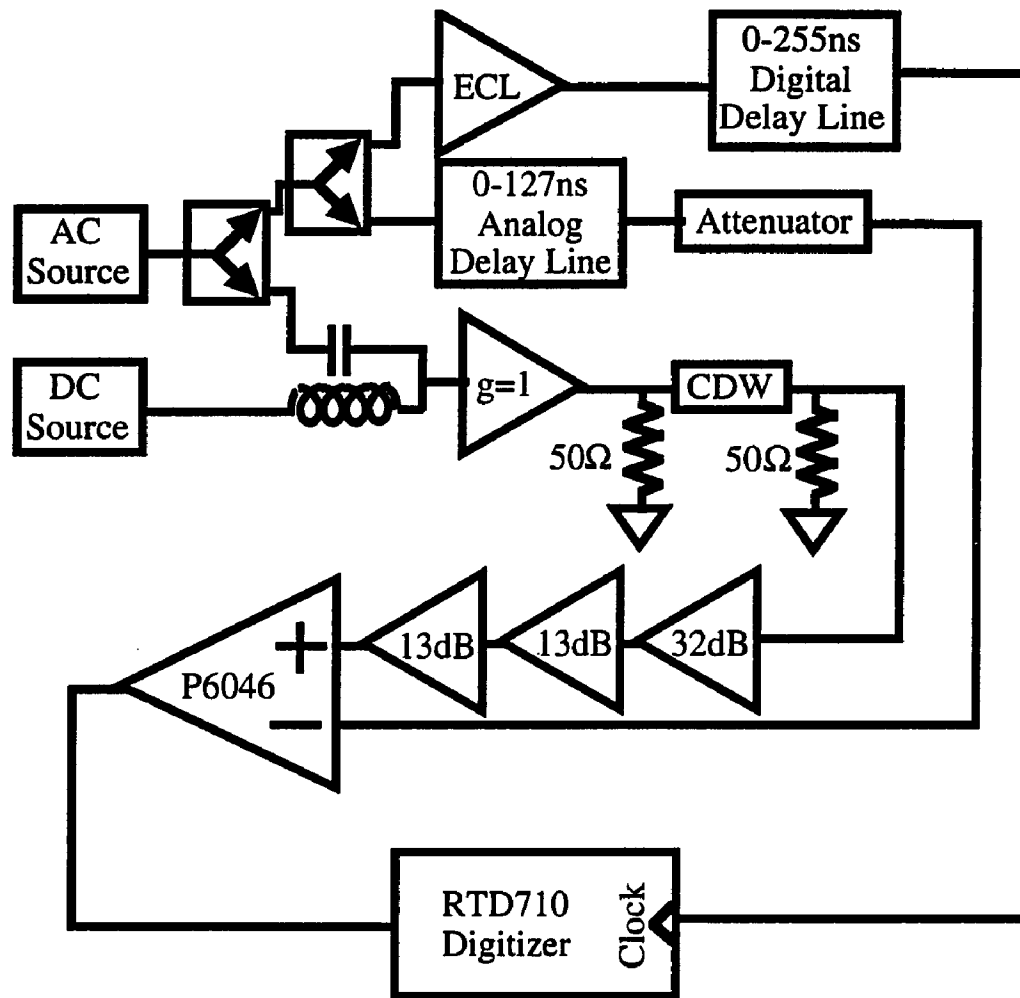


Figure 2.8: Schematic drawing of subtraction circuit for experiments with combined ac and dc driving.

sure that all instruments shared a common ground point greatly reduced the amount of line-cycle noise.

Radio-frequency noise was much harder to eliminate, and required the use of a shielded room. Special care was taken to ensure that no digital instruments were in the room. Even well-shielded GPIB cables can track in large amounts of digital noise. The DC signals were generated from 16-bit D/A converters on the computer, but were fraught with clock noise. Pi-filters were the most successful in filtering digital noise, and they were also used to filter noise coming from the 10 μ A current sources used to forward-bias the temperature-sensing diodes.

Amplifier noise is always a problem, and choosing the right amplifiers can greatly improve the signal to noise ratio. The unity-gain followers used to drive the sample can themselves generate unwanted noise. We used an Elantec 2004C FET buffer which had a nominal bandwidth of 350MHz, and was relatively quiet. Attenuating the output of the buffer eliminated any residual noise. For amplifying output signals, the best wideband low-noise preamplifier we found was the Miteq AU-1310. It had a flat response from 10 kHz to 500 MHz, and had by far the lowest noise figure. After eliminating all other sources of noise, one's signal-to-noise ratio is limited by the noise figure of the first preamplifier.

2.5 Software

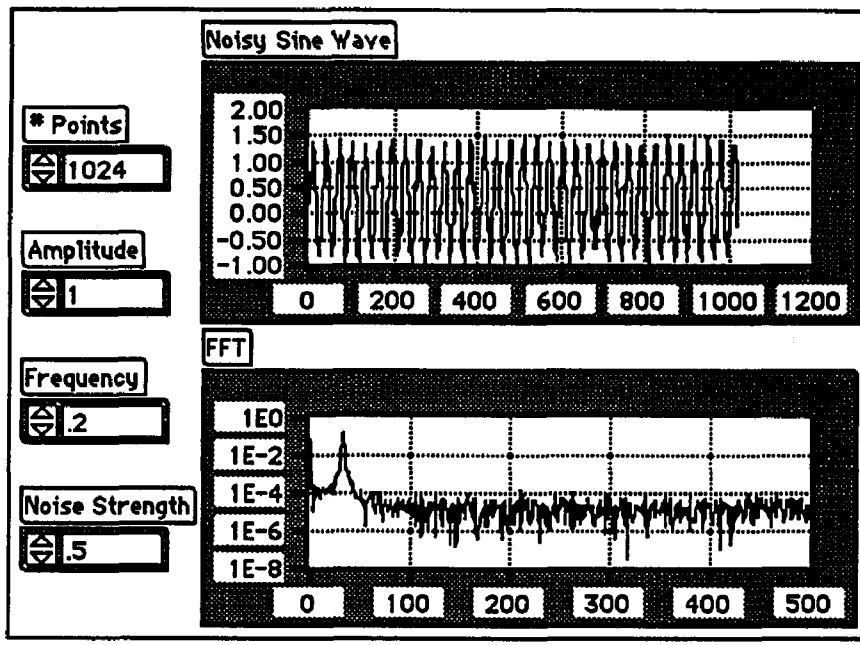
The software is the instrument.

The diagram is the software.

-*LabVIEW t-shirt*

A few words should be said about the software used to perform these experiments, since they required a great deal of automation. We used a program called LabVIEW, which is an object-oriented programming language much like C++, but with an emphasis on data acquisition and control. LabVIEW has a graphical interface, which means that instead of writing code as one does in most programming languages, the programs are constructed by wiring modules (subroutines) together from an extensive library. Because of its modular design, it is simple to automate complex tasks using LabVIEW. The top part of Fig. 2.9 shows the "front panel" of a typical "Virtual Instrument" (VI). The VI consists of sets of input and outputs, which can be numbers, arrays, graphs, strings, etc. The VI shown here generates a noisy sine wave, calculates the Fourier transform, and plots both. These inputs and outputs are then "wired" together on the VI diagram, shown in the bottom part of Fig. 2.9. As it says on my LabVIEW t-shirt, the diagram *is* the software. Because the VI diagram looks so much like a flow-chart, good programming techniques become almost unavoidable. LabVIEW makes the standard software "bug" (e.g., a misspelled variable name) an endangered species. Of course, one is still free to make conceptual errors.

Front Panel



Block Diagram

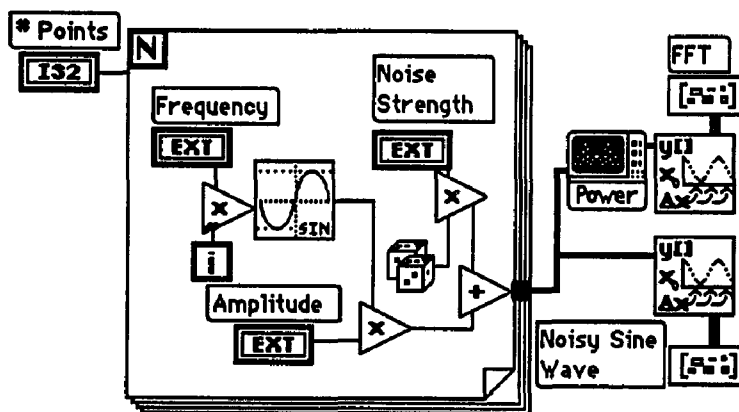


Figure 2.9: Sample LabVIEW Virtual Instrument. The entire program took less than five minutes to write.

Chapter 3

Conduction delays in switching NbSe₃: sensitive dependence on initial configuration

In “switching” charge-density-wave (CDW) conductors, a voltage pulse greater than threshold causes the CDW to slide only after a delay τ . For identical experimental conditions, we have found a new class of delays as long as 5 sec with fluctuations as large as five orders of magnitude. For large τ , the distribution of delays $N(\tau) \propto \tau^{-\gamma}$, with $0.8 < \gamma < 1.3$. We argue that τ measures the time at which the internal strain somewhere in the CDW exceeds the threshold for phase slippage. The electronic history of the sample, and hence the distribution of initial configurations of the CDW, determines $N(\tau)$.

Note: the reader of this thesis may wish to skip section 3.4 until he or she has read chapter 7, in which we describe an alternate explanation for conduction delays.

3.1 Introduction

Sliding charge density wave (CDW) conductors have now been established as models for the study of dissipative nonlinear dynamical systems with many equally-important degrees of freedom. The CDW in conventional samples depins smoothly at a threshold E_t . Classical models with many degrees of freedom have been successful in explaining the critical behavior of the depinning in conventional samples [59], hysteresis and non-exponential relaxations of the CDW polarization [60], and other observed phenomena. A central feature of these models is the existence of an exponentially large number of metastable states for a pinned CDW [12]. Switching samples depin abruptly and hysteretically. Zetl and Grüner observed

that, on applying current pulses larger than threshold, the CDW began to slide only after a time delay between 1 msec and 100 msec, with fluctuations of smaller than 100% from pulse to pulse [53]. We report detailed measurements of the delays near threshold. We find a new class of long switching delays clearly separated from the shorter ones observed by Zettl and Grüner. These long delays may be of order seconds, and fluctuate up to 5 orders of magnitude from one pulse to the next for identical external experimental conditions. Delayed transitions occur in many driven dynamical systems, from lasers [61] to convecting fluids. [62] However, we know of no physical system exhibiting delays with variability comparable to the long delays in switching CDWs. Our results rule out several theories of switching CDW conduction. We propose a novel mechanism: the switching delay is the time during which the CDW evolves from one of a large number of initial configurations to a configuration in which the internal strain is sufficiently large to tear the CDW.

3.2 Experimental Methods

Samples of freshly-grown, nominally-pure NbSe_3 were mounted in a standard two-probe configuration. The samples were cooled in a Helium exchange gas to between 25 K and 30 K in a temperature-controlled closed cycle refrigerator. The rms temperature fluctuations were 10 mK over an indefinite period of time. In initial experiments we applied a train of square pulses to a sample and measured the switching delay for each pulse. For voltages V near the threshold V_t the first delay was between 1 ms and 100 ms, but every subsequent delay was of order 1 ms. The CDW began in an unpolarized state. The first pulse polarized the sample, and for every subsequent pulse the initial state of the sample was highly polarized. This behavior is reminiscent of the pulse sign memory effect. [63] The initial state of the sample in large part determines the switching delay time. For all data presented here, the remanent polarization was erased before each square voltage pulse with a three-second “erasing pulse” (discussed below) of the form $V(t) = \frac{V_0}{2}(1 - \cos \Omega t) \cos(2\pi ft)$, with $V_0 = 185 \text{ mV} > 2V_t$, $2\pi/\Omega = 3 \text{ sec}$, and $f = 1 \text{ kHz}$. Fig. 3.1 shows the amplified CDW current response to four identical voltage pulses applied to a single sample. In order to use the full dynamic range of our digitizer, the ohmic current has been subtracted using a standard bridge circuit. Because the switching delays ranged from 1 msec–1 sec, the current was measured in logarithmic time intervals. The switching time was determined in software after each pulse. After the beginning of each pulse, a displacement current flows as the CDW polarizes, decreasing roughly logarithmically until the abrupt switch. The current traces are nearly identical before the abrupt switches. Thus the macroscopic CDW polarization $P = \int I_{\text{CDW}}(t)dt$ just prior to a switch depends on the switching delay τ . *Switches do not always occur at the same macroscopic polarization of the CDW.*

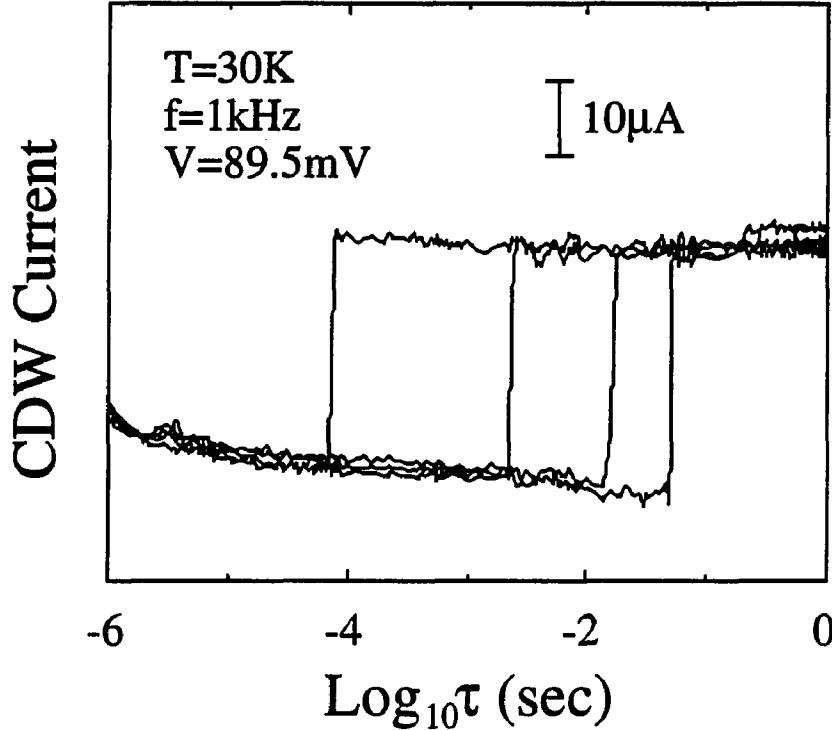


Figure 3.1: CDW current response to four identical voltage pulses.

3.3 Experimental Results

In presenting distributions which vary over many orders of magnitude, logarithmic binning in a histogram $N'(w = \log \tau)$ is preferable to conventional linear binning in a histogram $N(\tau)$. Fig. 3.2 shows the distribution of delays for a single sample under different experimental conditions. Fig. 3.2(a) shows the shift of $N'(w)$ from long to short delays as V is increased above the threshold V_t . (V_t was defined as the voltage at which 50% of the delays were less than 1 sec, 87.8 mV for these data. Changing the percentage criterion from 30% to 70% of the time shifted V_t less than $\pm 0.5\%$). For the smallest voltage $V = 88.6$ mV, the delays are between 100 msec and 1 sec. At an intermediate value $V = 89.4$ mV, the distribution is bimodal with a peak at a few μsec , a gap between 10 μsec and 100 μsec , and a broader peak between 100 μsec and 100 msec. For the highest value of $V = 90.2$ mV, most of the weight is in the peak near a few μsec .

Near V_c , the distribution $N(\tau)$ of long delays obeys a power law with a cutoff at short times. Fig. 3.2(b) plots $P(w) = \log(N'(w)/10^w)$ for 4000 long delays at $V = 89.3$ mV. It can

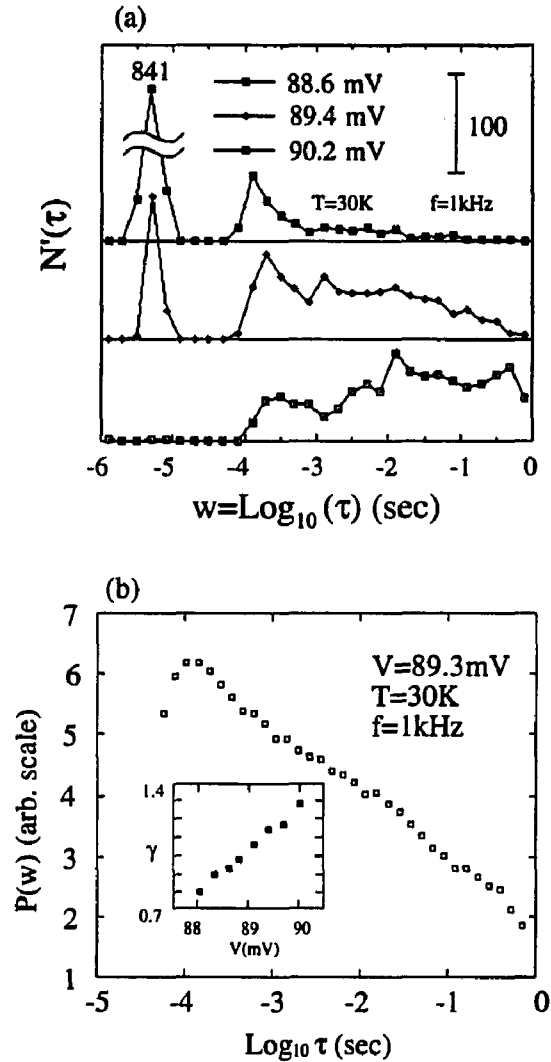


Figure 3.2: Distributions of delays. (a) Dependence on V : Three distributions $N'(w)$ (where $w = \log \tau$) of 1024 delays each, binned in logarithmic increments. The distribution shifts to shorter times as V is increased. A gap in $N'(w)$ appears between 10 and 100 msec. (b) Power law: For $\tau > 10^{-4}$ sec, $N(\tau) \propto \tau^{-\gamma}$. This is evident here because $P(w) = \log_{10}(N'(w)/10^w)$ lies on a straight line over four orders of magnitude (see text). Inset graph shows the dependence of the exponent γ on the pulse height V . Standard error on γ was of order 5%.

easily be shown that, if $N(\tau) \propto \tau^\gamma$, then $N'(w) \propto 10^{(1-\gamma)w}$ and $P(w) = -\gamma w + \text{constant}$. $P(w)$ in Fig. 3.2(b) is clearly well-fit by a straight line over at least four orders of magnitude. A least-squares fit of a line to $P(w)$, with points weighted by $\sqrt{N'(w)}$ and including only points with $-0.02 > w > -4.1$ ($100 \text{ msec} < t < 1 \text{ sec}$), gave us γ . The inset shows the variation of γ from 0.8 to 1.2 as V was varied from 88 to 90 mV (sufficiently close to V_t that few short delays appeared). The form of $N'(w)$ depends critically on the erasing frequency f . For $50 \text{ Hz} < f < 5 \text{ kHz}$, delays were uncorrelated¹, indicating that the erasing procedure was effective. With all other experimental parameters (including any thermal or other noise) fixed, the width of $N'(w)$ for the long delays drops from four to two orders of magnitude as f is increased from 50 Hz to 5 kHz. For $f > 5 \text{ kHz}$, correlations develop between successive delays. The sensitive dependence of $N'(w)$ on f shows that external noise is not the dominant cause of fluctuations in τ , in conflict with the explanation of Joos and Murray. [64]

Fig. 3.3 shows the dependence of the average $\langle \tau \rangle$ and standard deviation σ on the pulse height V with $f = 1 \text{ kHz}$. Between $V = 88 \text{ mV}$ and 92 mV , the average delay decreases by three orders of magnitude and σ is larger than $\langle \tau \rangle$. Near 92 mV , the gap evident in Fig. 3.2(b) appears. Above 92 mV , only short delays are observed, with $\sigma < \langle \tau \rangle$. Note that the voltage at which the gap occurs is different in Figs. 3.3 and Fig. 3.2(b). We attribute this to an observed extremely long-term (weeks) drift in the threshold voltage. Thin, short samples of uniform cross-section from freshly-grown batches of NbSe_3 are most likely to have a single switch. All measurements reported here were performed on a single sample 0.4 mm long with resistance 630Ω at 25 K and $3.81 \text{ k}\Omega$ at 295 K . A temperature of 30 K was convenient because switching does not occur much above 30 K in virgin samples, [51] and at much lower temperatures heating becomes a problem. Lowering the temperature to 25 K did not qualitatively change the observed behavior. Measurements were also performed on other samples from two growths. All samples we measured showed long and short delays with a gap in $N(\tau)$ in the range $10 \text{ msec} - 1 \text{ msec}$, a power law tail in $N(\tau)$ for long delay times, and $\langle \tau \rangle$ decreasing faster than $\epsilon^{-\beta}$ for small ϵ , where $\epsilon = (V - V_t)/V_t$. The exact position of the gap and the exact form of $\langle \tau \rangle(\epsilon)$ vary from sample to sample. Initial observations by Zetl and Grüner [53] are consistent with the short delays we have observed.

3.4 Discussion

Several theories have been proposed to explain CDW conduction in switching samples. Hall et al. [51] have proposed that switching samples contain a few "ultrastrong pinning

¹ We calculated the delay-delay autocorrelation function $C(n) = 2/N \sum_{j=1}^{N/2} \tau_j \tau_{j+n}$ for each series of N delays $\{\tau_j\}$ [$C(n)$ defined for $0 \leq n \leq N/2$]. If $C(n)$ decayed from $C(0) \approx \sigma^2 + \langle \tau \rangle^2$ where σ and $\langle \tau \rangle$ are the standard deviation and average of the distribution of τ , to $C(n) \approx \langle \tau \rangle^2$ for all $n > 0$, the delays were defined to be uncorrelated: this is the expected behavior for a series of uncorrelated random events.

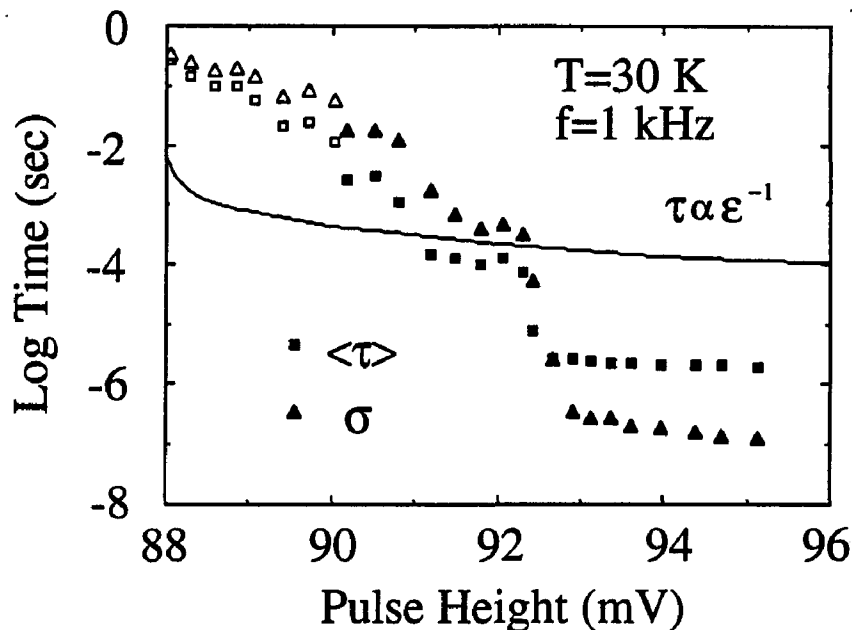


Figure 3.3: Average $\langle \tau \rangle$ (\square) and standard deviation σ (\triangle). Only distributions with fewer than 10% of delays longer than 1 sec are included. The σ and $\langle \tau \rangle$ represented by hollow symbols are systematically low: some of these delays were longer than 1 sec but are included in the average as 1-sec delays. Each $\langle \tau \rangle$ is the average of 1024 delays. The solid line represents $\langle \tau \rangle(\epsilon) \propto \epsilon^{-1}$ (for $V_t = 87.8$ mV) predicted for the model of Strogatz et al. (ref. [65]).

centers" [66] which prevent the intact CDW from sliding. The CDW can slide only when the internal strains become sufficiently large to cause tears, or phase slips, in the fabric of the condensate. Inui et al. [56] proposed a many-body Hamiltonian embodying these ideas, and they numerically investigated a 1-degree-of-freedom version. Strogatz et al. [67] have proposed a different, exactly-soluble many-body Hamiltonian that is isomorphic to the mean-field x-y model. Each of these models shows delayed switching, [65] with $\tau \propto \epsilon^{-\beta}$. For the model of Strogatz et al., $\beta=1$ (solid line in Fig. 3.3) and for any 1-degree of freedom model, $\beta = 1/2$. Using our operational definition of V_t to define ϵ , the average τ decreases faster than ϵ^{-2} for $0.005 < \epsilon < 0.05$, ruling out the model of Strogatz et al. and all 1-degree-of-freedom models. There are no fluctuations in τ reported for the model of Strogatz et al.

We analyze our results by modifying successful classical models of conventional sliding

CDW conduction to include ultrastrong pinning centers. A discretized phase-dynamical model that has been studied numerically by a number of authors is [11, 12]

$$\frac{d\phi_i}{dt} = \frac{\phi_{i+1} - \phi_i}{x_{i+1} - x_i} - \frac{\phi_i - \phi_{i-1}}{x_i - x_{i-1}} + \frac{e}{2}(x_{i+1} - x_{i-1}) + V \sin(\phi_i - \beta_i) \quad (3.1)$$

where ϕ_i is the phase of the CDW at the i^{th} impurity site, x_i is the random dimensionless position of the i^{th} impurity, e is the dimensionless electric field, V is the strength of the impurity pinning potential, and β_i is a random phase. Phase-dynamical models are only valid when the local strain, or phase gradient $\phi' = \frac{d\phi}{dx}$ of the CDW is smaller than a critical value ϕ'_c . A phase gradient larger than ϕ'_c will cause the CDW to tear by nucleating a phase vortex. [51, 56] The sparsely-distributed, extremely strong impurities that pin CDW in switching samples prevent the CDW from sliding even above the critical voltage for depinning in conventional samples. [51] In our picture, as the voltage across the sample is increased, the local strain somewhere in the sample will eventually exceed ϕ'_c . At this point, a large portion of the CDW begins to slide. We have assumed that, on application of a voltage pulse, phase-slippage does not occur until $t = \tau$. Thus the details of the dynamics of phase slippage are unimportant in modeling τ . We can qualitatively explain our data with two simple modifications to Eq. 3.1:

- The presence of a single extremely strong pinning center is modeled by changing the boundary condition to fix the phase at one end of the chain.
- Each “spring” is assigned a breaking threshold ($\phi_{i+1} - \phi_i t = \Delta\phi_i^t = \phi'_c l_i$ where $l_i = x_{i+1} - x_i$ is the distance between impurities. The state of a static CDW in configuration space can be defined by the vector $\mathbf{v} = (\Delta\phi_1, \Delta\phi_1, \dots, \Delta\phi_N)$, where $\Delta\phi_1 \equiv \phi_{i+1} - \phi_i$. The intersection of the planes defined by $\Delta\phi_i = \Delta\phi_i^t$ defines the surface of a “hyperrectangle”² in the configuration space of the CDW. We call this surface the phase-slip boundary (PSB). The volume enclosed by the PSB contains all phase-slip-free configurations of the CDW. At any point exterior to the PSB, phase slippage must occur and the CDW must slide. The switching delay τ is then the time it takes for the CDW to evolve from one of an exponentially large number of metastable configurations to the PSB.

This simple picture qualitatively explains many of our observations.

- Memory of previous switch: A CDW begins from a relaxed state. A pulse applied to this CDW will cause a switch after a relatively long delay τ_0 and place the CDW in a highly-polarized configuration. A second pulse will cause a switch in a shorter time τ_1 , because the highly-polarized configuration is closer to the PSB.

²Like a hypercube, but with edges of unequal length.

- Displacement current: The current that flows before the switch in Fig. 3.1 is the displacement current of a polarizing CDW.
- τ and the macroscopic polarization: The switch in this model will not always occur at the same macroscopic CDW polarization because the condition for switching is that the local phase gradient $\phi'_i > \phi'_c$.
- Distribution of delays and erasing pulse: Each of the exponentially large number of metastable configurations of the CDW should take a different time to evolve to the PSB. Contributions to the maximum width of the distribution of delays come from distributions in both initial configurations and in $\Delta\phi'_i$. As the erasing frequency f is increased, smaller and smaller subsets of allowed initial configurations are sampled, as shown by the decreasing width of $N'(w)$.

The erasing frequency at which erasing pulses become ineffective, 5 kHz, is close to the reciprocal of the position of the long-time edge of the gap in Fig. 3.2(b) ($t \approx 10^{-4}$ sec). Such high-frequency pulses could induce no long switches, although with amplitude $2V_c$ they repeatedly depinned the CDW after short switches. Apparently, many long switches are required to access a wide distribution of initial configurations. However, to understand the central result of this chapter, that the switching delay is extremely sensitive to the initial configuration, requires dynamical simulations beyond the scope of this chapter.³ A clarification of dynamic issues will shed new light on the distribution and evolution of internal strains in CDW conductors, quantities that have been inaccessible to previous experiments.

The theoretical model proposed in this chapter assumed that phase slip was the physical mechanism behind switching. As will be discussed in chapters 6 and 7, there is compelling evidence that switching is the result of the interaction of the CDW with uncondensed carriers. However, several aspects of this model, such as the motion of the CDW as it polarizes [68], may still be applicable.

³A detailed study of the model presented in this chapter is presented in Refs. [68, 69].

Chapter 4

Multiple Attractors and Dynamical Solitons in Mode-Locked Charge-Density Waves

This chapter describes time-domain measurements of the dynamics of charge-density waves in the presence of applied dc + ac electric fields. The techniques of nonlinear dynamics have proven especially useful in understanding much of the mode-locking behavior that was observed. Time-domain measurements have allowed us to address many outstanding questions regarding mode-locking. We find that the dynamics of the mode-locked state is in many respects similar to the pinned state, in which there exist many metastable configurations. The dynamics that moves the CDW between nearby configurations is seen to be dominated by dynamical solitons, analogous to the solitons that separate nearby metastable configurations in the pinned state.

4.1 Introduction

For dc electric fields greater than threshold, the CDW depins from impurities and slides through the crystal. As the CDW slides, it interacts with an impurity potential that is periodic in the rigid displacement of the CDW by one wavelength, generating so-called “narrow-band noise” (NBN) of frequency ω_{nbn} . The application of combined dc+ac currents produces rich “interference” phenomena [31, 70, 71]. In general, ω_{nbn} can lock to the external drive frequency ω_{ex} over a finite range of dc bias when the p^{th} harmonic of ω_{ex} is sufficiently

close to the q^{th} harmonic of ω_{nbn} . Previously, experiments performed on mode-locking in CDWs have fallen into two categories: measurements of the dc differential resistance dV/dI , and measurements of the power spectrum of the CDW voltage or current.

In the presence of combined dc+ac currents, dV/dI contains rich structure. Complete mode-locking occurs [32, 36] when the velocity of the entire CDW is locked to the external drive frequency over a finite range of dc bias (or external drive frequency). Complete mode-locking is manifested in dV/dI as a feature with a flat top at the ohmic ($I_{\text{dc}} = 0$) resistance value flanked by negative “wings”. The negative wings occur when ω_{nbn} is “pulled” [72] towards ω_{ex} prior to locking. Incomplete mode-locking [70, 71, 32] occurs when a portion of the CDW remains unlocked, and is manifested in dV/dI as a flat-topped peak that does not attain the dc value but still has negative wings [72]. Many interference features in dV/dI are simple peaks, without flat tops or frequency pulling. Such features have been the cause of some confusion in the literature. Some theories have attributed such features to “increased dissipation” [73] or “Shapiro anomalies” [74, 75]. In the experimental literature, such features have been termed “unlocked” [72], or possibly “intermittently locked” [37].

A second class of measurements has been in the frequency domain. By measuring power spectra, several authors [37, 34] have observed that, upon mode-locking, the quality factor ($Q = \omega/\Delta\omega$) of the NBN increases dramatically from its $I_{\text{ac}} = 0$ value to a value that is resolution-limited. However, the NBN amplitude fluctuations, observed in the $I_{\text{ac}} = 0$ state, often persist in the mode-locked state [71, 37]. Furthermore, the NBN amplitude does not increase dramatically in the mode-locked state [71, 37, 34]. This has been a puzzling observation [34]: Fisher [35] has predicted that the NBN amplitude should scale as $\xi_{\text{dyn}}^{d/2}$, where ξ_{dyn} is the dynamic velocity-velocity correlation length of the CDW and d is the dimension, and Matsukawa [74, 75] has predicted that ξ_{dyn} diverges in the mode-locked state.

Measurements of dV/dI and power spectra have failed to provide an unambiguous identification of mode-locked CDW dynamics. Four fundamental questions remain unanswered:

1. How should one define mode-locking for CDWs?
2. Are non-mode-locking mechanisms necessary to explain all the structure in dV/dI ?
3. Why do NBN amplitude fluctuations persist during mode-locking?
4. Why is there no dramatic enhancement of the NBN amplitude during mode-locking?

This chapter describes the first real-time measurements of the dynamics of a mode-locked charge-density wave. Poincaré sections in two dimensions have been reconstructed from recorded time series. Some high-sampling-rate time series are also presented. These powerful methods have been fruitfully applied to other experimental systems exhibiting quasi-periodicity and mode-locking [76, 77] The outstanding questions described above are resolved, and several new ones are raised.

4.2 Experimental Set-up

A sample of high-quality NbSe₃ was driven by combined dc and ac currents $I(t) = I_{dc} + I_{ac} \cos(\omega_{ex}t)$. The voltage $V(t)$ across the sample was amplified with an ultra-low-noise preamplifier. In mode-locked NbSe₃, the narrow-band noise voltage amplitude is roughly 60 dB smaller than the ac voltage across the sample. To increase the effective dynamic range of our digitizer, the sinusoidal component of the voltage across the sample was subtracted out using a high-speed differential amplifier. The resulting signal was then further amplified and digitized at intervals of the drive period $T = 2\pi/\omega_{ex}$. The resulting time series,

$$\{V_n \equiv V(t = nT + t_0), 0 \leq t_0 < T\}, \quad (4.1)$$

was then analyzed using recently developed techniques of time series analysis.

All measurements reported here were performed in a standard two-probe configuration, on a single crystal of high-purity (RRR=240) NbSe₃. The sample was mounted on the end of two .001" Au wires with silver paint, as described in Chapter 2. In order to minimize the effects of sample heating, the samples were placed in a He exchange gas (again, for details, see Chapter 2). This experiment was performed in the non-switching regime ($T \geq 35$ K). We chose to work at $T=48$ K, where the sample resistance has a local maximum (see Fig. 1.5)), so that slight variations in temperature would have as small an effect as possible on the measurements.

4.3 Experimental Results

The lower trace of Fig. 4.1 shows dV/dI vs. I_{dc} for $I_{ac}=0$ at $T=48$ K. For this sample, dV/dI drops abruptly at threshold, partially recovers, and then decreases more slowly. Such a dV/dI curve was first reported in NbSe₃ by Thorne *et al.* [33] in a sample for which the Q of the NBN was extremely high, and which exhibited complete mode-locked behavior of very high quality.¹ When biased with only a dc current such that $\omega_{nbn} \simeq 30$ MHz, the Q of the NBN for our sample exceeds 10^4 . The upper trace of Fig. 4.1 shows dV/dI for $I_{ac} = 1.5$ mA and $\omega_{ex}/2\pi = 13$ MHz. Complete mode-locking occurs up to $p : q = 1 : 5$ and small peaks occur up to $1 : 13$. Such fine structure in mode-locking and high-Q NBN are only observed in high-purity samples that have been carefully selected and handled [34].

Fig. 4.2 shows a high-sampling-rate trace of the current when the CDW is mode-locked on the 1:2 step. Most of the fundamental signal has been subtracted. The open circles indicate where the Poincaré sections were taken. Note the rich harmonic content of the CDW response.

¹It has been recently suggested that the shape of this kind of dV/dI curve is a finite-size effect [78]. This behavior has also been observed in very small samples of o-TaS₃. See F. Ya. Nad', Ref. [8].

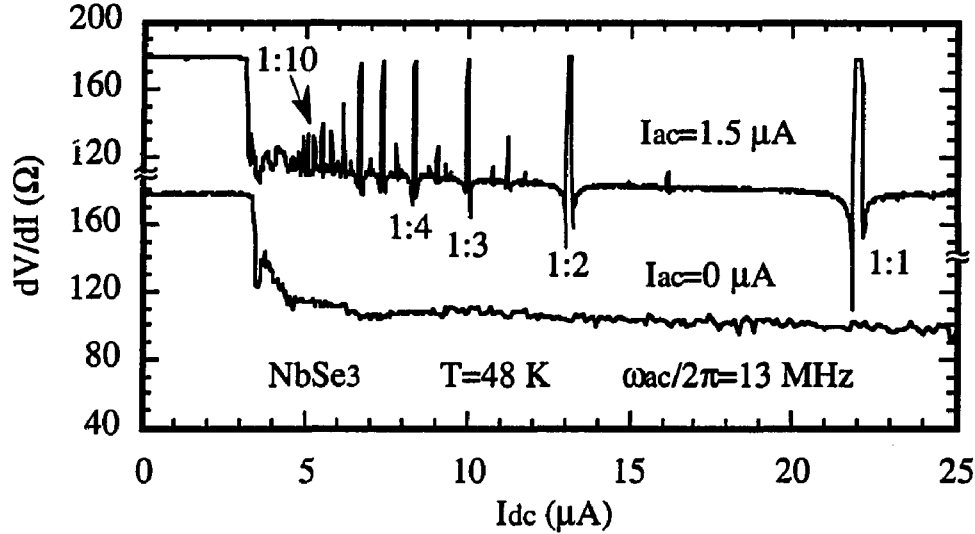


Figure 4.1: The lower trace shows differential resistance dV/dI vs. dc current I_{dc} with no ac driving. The upper trace shows dV/dI with ac driving. Subharmonic peaks occur up to $\omega_{nbn} : \omega_{ex} = 1 : 13$.

Fig. 4.3 shows Poincaré sections of unlocked and locked CDW dynamics. The Poincaré section is reconstructed by embedding the time series in two dimensions to form vectors $V_n = (V_n, V_{n+r})$ (the “method of delays”) [79]. Figs. 4.3(a-h) each contain 1024 points. Fig. 4.3(a) shows V_n versus V_{n+1} when the sample was biased at the middle of the 1:2 ML step in dV/dI . The density of points is peaked around two well-separated period-two points. Fig. 4.3(b) shows V_n versus V_{n+3} on the 1:10 peak in dV/dI . One can see that there are ten well-defined points, indicating that the CDW is mode-locked. Fig. 4.3(c) shows 1:34 locking. Because there is a large overlap of period-34 points, we have plotted the average of every 34th point as open circles in Fig. 4.3(d). The small dots show every 34th point, the average of which is the large solid black circle. Fig. 4.3(e) shows 29:60 locking with $r = 14$. As in Fig. 4.3(d), we have plotted the average of every 60th point as open circles in Fig. 4.3(f). The small dots show every 60th point, the average of which is the large solid black circle. Fig. 4.3(g) shows the Poincaré section where dV/dI shows no peak. The density of points is peaked along a closed curve (henceforth, “circle”). Fig. 4.3(h) shows the Poincaré section constructed from the same 32K record as Fig. 4.3(c), but 18,000 drive cycles earlier. The circle remains, but is smaller and clearly different in shape.

Fig. 4.4 displays in more detail the dynamics near the 1:2 mode-locked state. In analogy with the staggered magnetization in an antiferromagnet and the staggered order parameter

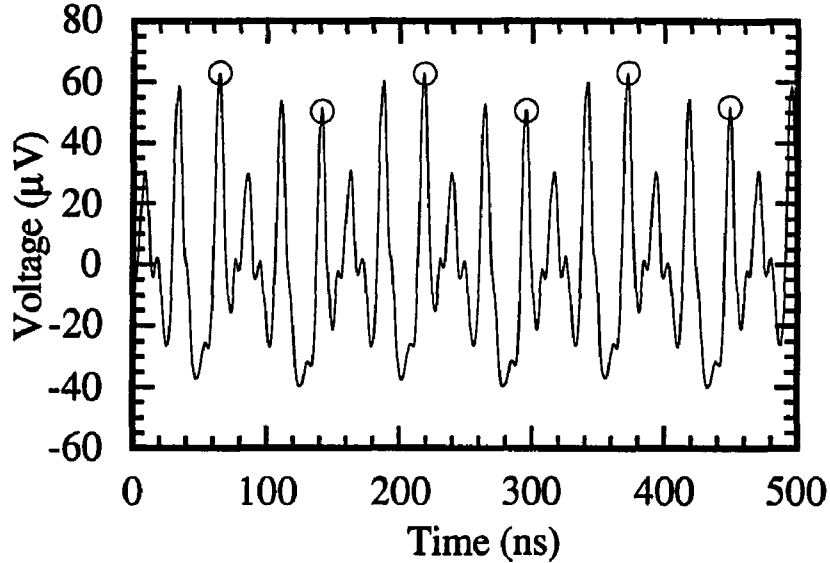


Figure 4.2: High-sampling-rate measurement of CDW voltage near 1 : 2 step for $I_{ac}=1.5 \mu A$ and $\omega_{ac}/2\pi=13$ MHz. The signal has been averaged 32 times in a region where the NBN amplitude remains constant for minutes at a time. Circles indicate where Poincaré sections were taken.

in a $1/2$ filled Peierls system one can define a “dynamic staggered order parameter” (DSOP) to describe the dynamics of the 1:2 mode-locked state. One writes $s_n = (-1)^n v_n$, and

$$S_n = \text{Av}[s_n, s_{n+1}, \dots, s_{n+j-1}], (j = 10) \quad (4.2)$$

for a suitable averaging. Ideal mode-locking would correspond to a constant value of S_n for all n . Fig. 4.4 shows the DSOP over 32,000 cycles of rf drive for various values of I_{dc} . In Figs. 4.4(a-b) the sample was biased near the middle of the 1:2 mode-locked step. The DSOP is essentially constant in both traces, but the magnitudes differ. For slightly higher I_{ac} than shown here, the amplitude of NBN, and hence the DSOP, can remain constant for several minutes [71], in contrast to some earlier observations [37]. In Fig. 4.4(c), the sample was biased on the edge of the 1:2 mode-locked step. The DSOP is constant over more than 16000 cycles, switches sign, and afterward exhibits long-term drifts in magnitude. In Fig. 4.4(d), the sample was biased just below the 1:2 mode-locked step. The behavior is intermittent and aperiodic. In Fig. 4.4(e), the sample had been damaged by excessively

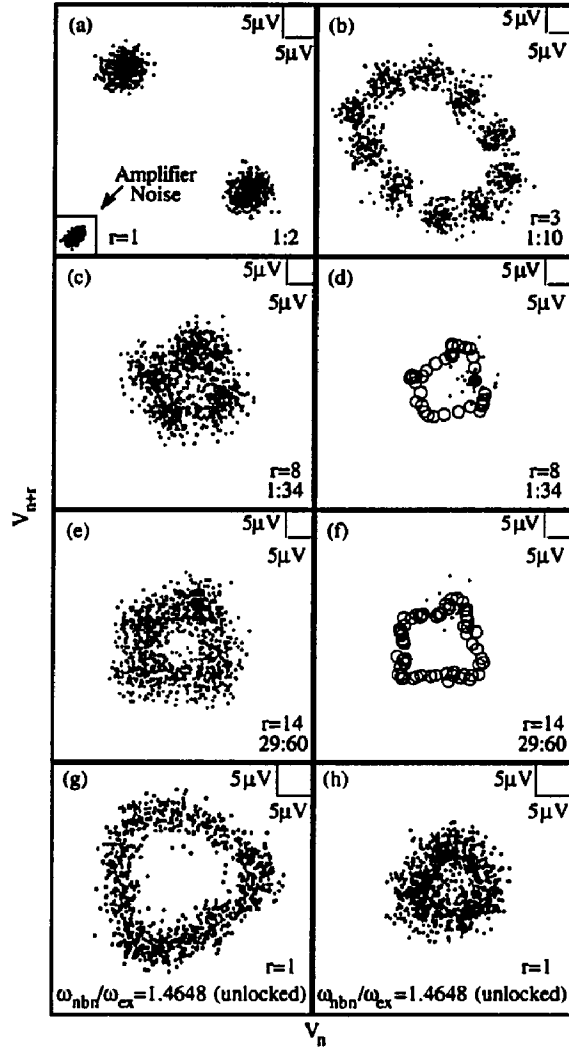


Figure 4.3: Poincaré sections obtained by method of delays. The driving frequency is $\omega_{ex}=13$ MHz.

(a) Biased at the 1 : 2 mode-locked step, $I_{ac} = 1.5 \mu A$. Inset shows strength of amplifier noise. (b) Biased at the 1 : 10 mode-locked step, $I_{ac} = 5.0 \mu A$. (c) Biased at the 1 : 34 mode-locked step, $I_{ac} = 5.0 \mu A$. (d) Average of period-34 points shown in (c) plotted as open circles. The small dots show points $34j$, where j is an integer. The large solid circle is the average of the small dots. (e) Biased at the 29 : 60 mode-locked step, $I_{ac} = 5.0 \mu A$. (f) Average of period-60 points shown in (e) plotted as open circles. The small dots show points $60j$, where j is an integer. The large solid circle is the average of the small dots. (g) Biased in an unlocked region, $I_{ac} = 1.5 \mu A$. (h) Same as (g), but 18,000 drive cycles earlier, $I_{ac} = 1.5 \mu A$.

high rf fields.² The sample was biased just as for Figs. 4.4(a–b), but here the DSOP takes on many different discrete values, and shows concomitant locked and unlocked behavior (see arrows). This behavior is similar to that observed in samples of lesser quality.

One can construct a similar order parameter for other $p : q$ mode-locked states. In principle, if one wanted to include all of the points, the order parameter would be complex, but one can keep it real by looking only at every q^{th} point. In this way we define

$$s_n^{p:q} \equiv V_{qn+n_0} \quad (4.3)$$

where $0 \leq n_0 < q$. Fig. 4.3 shows a plot of $s_n^{1:d}$ versus $d * n$ for $d = 33, 34, 35$, from the same 32K time series with $I_{ac}=1.5 \mu\text{A}$ and $\omega_{ac}/2\pi=13 \text{ MHz}$. The time series has not been averaged this time. The fast oscillations for $d = 33$ and $d = 35$ indicate that the CDW is not locked at the 1 : 33 step nor at the 1 : 35 step. If one looks at $d = q = 34$, one sees that it is intermittently locked at the 1 : 34 step (c.f. Fig. 4.4(d)).

The dynamics is also quite interesting near the threshold of an integrally mode-locked step. Fig. 4.6(a) shows the time series where the CDW is biased at the threshold of the 0 : 1 mode-locked step. The spikes in V_n correspond to “avalanches”, in which there is a surge of current. Apart from the largest oscillations, the time-series is qualitatively self-similar, as one can see from the close-up in Fig. 4.6(b). A power spectrum of the entire 32K time series is shown in Fig. 4.6(c).

We structure our analysis around the four outstanding questions stated earlier.

(1) In the study of dissipative dynamical systems, qualitatively distinct dynamical states are usually associated with topologically inequivalent attractors. For systems with two competing frequencies, three kinds of behavior are usually observed: periodic, or mode-locked; quasiperiodic; and chaotic [42, 43]. Chaos has been observed only in switching CDW conductors [47, 48], and will not be further discussed in this chapter. The Poincaré sections of the attractors for periodic and quasiperiodic behaviors are, respectively, zero-dimensional (q distinct points for $p : q$ mode-locking), and one-dimensional (“circle”). We define as mode-locked a state whose Poincaré section reduces to a set of points. Even in the presence of measurement noise, by averaging as was done in Fig. 4.4(b), such an attractor is topologically distinguishable from the circles shown in Figs. 4.4(c–d).

(2) As defined above, we observe mode-locking on all peaks in dV/dI . Thus it is unnecessary to invoke non-mode-locking mechanisms to explain structure in dV/dI . On the 1:9 step, dV/dI shows a simple peak and does not rise to its ohmic value. The Poincaré section reduces to a set of 9 points over time intervals of order 1000 drive cycles. Over longer time scales, the Poincaré section is “smeared” by portions of the CDW that become unlocked. Mode-locking on simple peaks in dV/dI is thus both intermittent and incomplete.

(3),(4) Questions concerning the persistence of fluctuations and the lack of enhancement of NBN amplitude during mode-locking have not been linked in the past. However, they

²Interestingly, the anomalous behavior in dV/dI at threshold was unaffected by the damage.

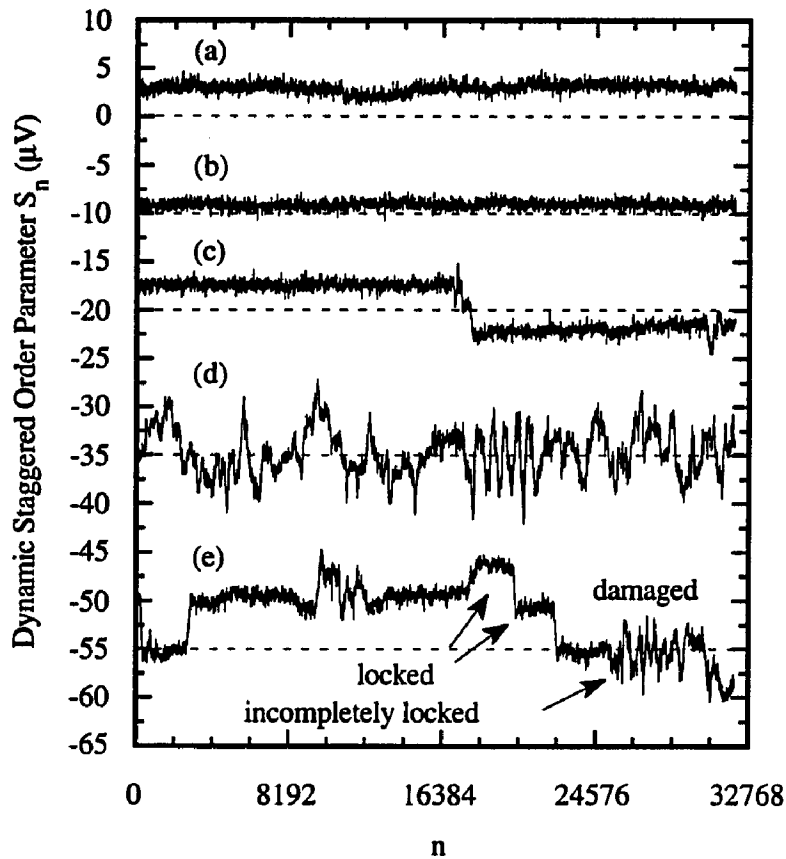


Figure 4.4: Dynamic staggered order parameter (DSOP) (see text for discussion) for various values of I_{dc} near the 1:2 mode-locked step. Dashed lines refer to (a) $I_{dc} = 13.083\mu A$, biased in the middle of the 1:2 step. DSOP is constant with slow modulations. (b) $I_{dc} = 13.034\mu A$. DSOP is *different* in magnitude from (a). (c) $I_{dc} = 12.984\mu A$. Biased near the edge of the 1:2 step. DSOP switches sign near $n = 16000$, then drifts slowly. (d) $I_{dc} = 13.131\mu A$. Biased just past the 1:2 step. DSOP is aperiodic and intermittent. (e) Biased in the middle of the 1:2 step. The sample has been damaged by excessive rf fields. Arrows point to completely locked and partly locked behavior.

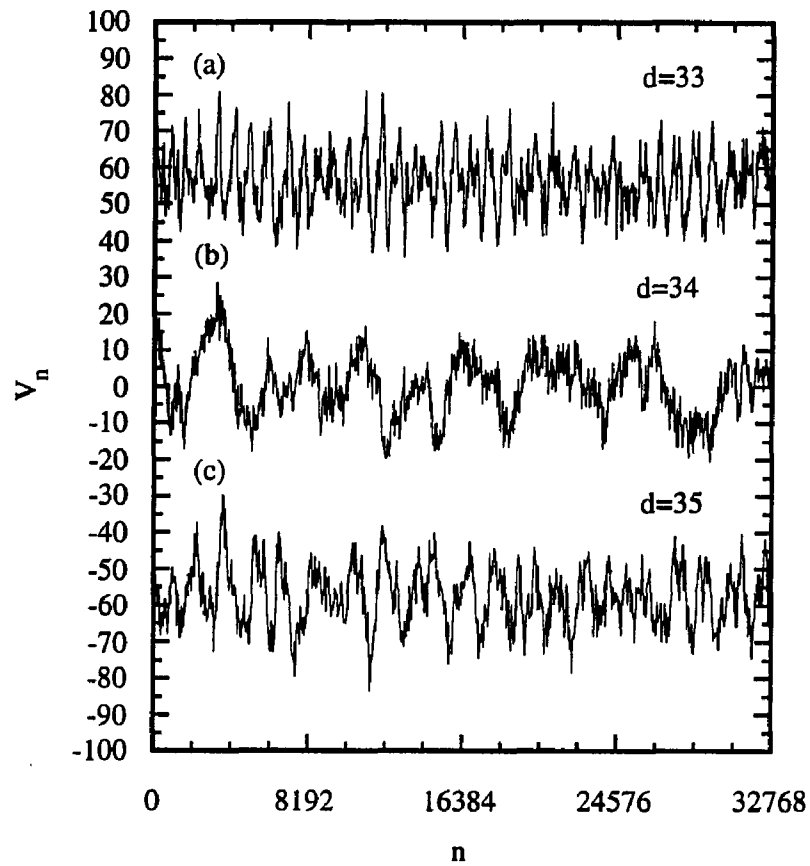


Figure 4.5: Plot of every d^{th} point of the time series shown in Fig. 4.3(d) for various values of d . (a) $d = 33$. (b) $d = 34$. (c) $d = 35$.

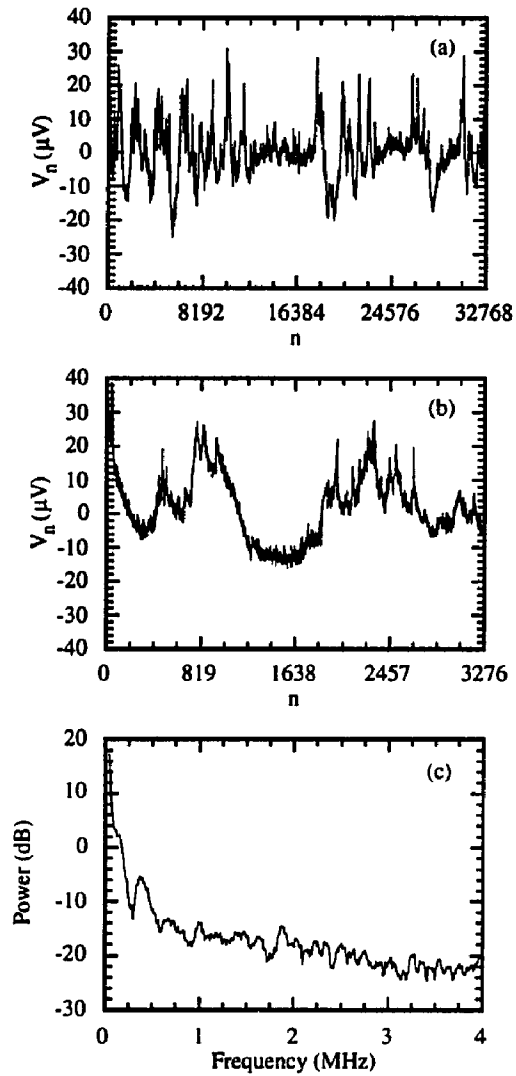


Figure 4.6: (a) Plot of time series near the edge of the 0 : 1 mode-locked step. The spikes correspond to “avalanches”, in which a portion of the CDW advances, carrying current. (b) Close up of the first 10th of the time series. (c) Power spectrum of the entire 32K time series.

have a common resolution within the framework of the Fukuyama-Lee-Rice (FLR) picture of a deformable CDW interacting with random impurities [80]. Theoretical studies of mode-locking in the FLR model have been performed by Coppersmith and Littlewood [73] and by Matsukawa and Takayama [74, 75, 81]. Coppersmith and Littlewood have concentrated their simulations in the regime where the external field brings the CDW below threshold, and the CDW has time to relax towards a pinned configuration within each cycle of the ac field. For the data in Fig. 4.4, the CDW spent no time below threshold. Consistent with experiments of Thorne [33] Matsukawa has confirmed numerically that mode-locking occurs within FLR whether or not the CDW spends time below threshold [81]. He proposed that mode-locking is accompanied by a dynamical phase transition, where the CDW velocity-velocity correlation length ξ_{dyn} diverges as the mode-locked state is approached.

We note that $p : q$ subharmonically mode-locked phases are q -fold degenerate: q equivalent attractors exist, each invariant only under translations by q cycles of the external drive. At the mode-locked phase transition, different domains of the CDW can fall into different attractors. Portions of the CDW in different attractors must be separated by a domain wall. For concreteness, we consider the $p : q = 1 : 2$ step, where $\omega_{\text{ex}} = 2\omega_{\text{nbN}}$ exactly, although the arguments are easily generalized to the $p : q$ mode-locked case. In the 1:2 case the magnitude of the DSOP is proportional to the magnitude of the NBN. At each point in the sample the CDW can be in one of two attractors. Consider the following 2 hypotheses, which are not rigorous but illustrate our point qualitatively.

1. A local DSOP density $\rho_D(x)$ can be defined at each point in the crystal. At each x , $\rho_D(x)$ can take on only two values ± 1 , corresponding to the two degenerate attractors.
2. The DSOP that is measured in experiments is the integral of $\rho_D(x)$ over the entire crystal volume Ω .

These hypotheses have several consequences:

1. For subharmonic mode-locking, the DSOP does not have a unique value for a given set of external parameters. The measured DSOP can in principle take on any value between $-\Omega$ and Ω . As in the pinned state, there should exist physically distinct, dynamically stable configurations of the mode-locked CDW. The change in magnitude from Fig. 4.4(a) to Fig. 4.4(b) is an illustration.
2. NBN need not be enhanced during mode-locking. In fact, if the physically preferred configurations of the CDW are ones in which roughly equal portions of the sample have $\rho_D = \pm 1$, then the NBN amplitude V_{nbN} can actually be suppressed during mode-locking. It is commonly argued that NBN in the absence of ac driving vanishes in the thermodynamic limit. We believe this is also true for subharmonically mode-locked CDWs.

3. During mode-locking, fluctuations in V_{nb} occur if the sign of the DSOP density switches in a macroscopic domain within the sample. The macroscopic size and sudden nature of the jumps in DSOP in Figs. 4.4(c) and 4.4(e) suggest that the size of such domains is a large fraction of the crystal size. Also, movement of the domain walls could account for long-term drifts such as those seen in Fig. 4.4(c).

To illustrate these ideas, we have constructed a model consisting of locally coupled circle maps which, although not rigorously derived from the Fukuyama-Lee-Rice equations of motion, seems to capture the essential dynamics. The map can be written as

$$\begin{aligned} \varphi(i, n+1) = & \varphi(i, n) + \Omega + K \sin(\varphi(i, n) - \beta(i)) + \\ & D(\varphi(i+1, n) + \varphi(i-1, n) - 2\varphi(i, n)) + \\ & E_{\text{ac}} \sin(\varphi(i, n)) + \xi(i, n), i = 1, \dots, N_{\text{imp}} \end{aligned} \quad (4.4)$$

The $\varphi(i, n)$ represent the phases of the CDW at impurity site i at the n^{th} drive cycle. The phases are coupled by springs with spring constant D , to model the elasticity of the CDW. The $\beta(i)$ are random phases of the impurities which couple to $\varphi(i, n)$ with strength K . E_{dc} and E_{ac} can be thought of as the dc and ac applied fields, respectively. The E_{ac} term was inspired by the numerical simulations of Matsukawa [81], and can be thought of as an ‘‘ordering’’ field which tries to keep the phases aligned with the ac drive, but is frustrated by the random positioning of the impurities. There is a phenomenological white noise term $\xi(i, n)$, which is Gaussian with width σ .

One can define the total CDW current as

$$j(n) = \frac{1}{N_{\text{imp}}} \sum_{i=1}^{N_{\text{imp}}} \varphi(i, n) - \varphi(i, n-1) \equiv \frac{1}{N_{\text{imp}}} \sum_{i=1}^{N_{\text{imp}}} j(i, n) \quad (4.5)$$

The time-averaged current can be subtracted and the DSOP W_n defined:

$$\text{Av}[w_n, w_{n+1}, \dots, w_{n+k-1}], w_n = (-1)^n (j(n) - \pi), k = 10, \quad (4.6)$$

just as in Eq. (4.2).

Fig. 4.7 plots the DSOP W_n versus n . The DSOP starts off with a constant value 0.05, then at $n = 900$ drops suddenly to zero, recovers, and ends up at $n = 2800$ in a state where W_n is constant again but opposite in sign. Fig. 4.8 plots $\Delta\varphi(i, n) \equiv \varphi(i, n) - \varphi(i, 0) - n\pi$ for n even. The quantity $\Delta\varphi(i, n)$ represents the deviation of the phase from a metastable solution $\varphi(i, 0)$. A soliton-antisoliton pair (localized phase gradients with charge $\pm e$) are created at $n = 1000$, causing the sudden jump in the DSOP, and their propagation over the entire length causes the sign of the DSOP to change. As the solitons propagate, $\Delta\varphi(i, n)$ changes by $\pi + \rho_D(i)$, where $\rho_D(i) \equiv \varphi(i, 1) - \varphi(i, 0)$ is the local DSOP. The model presented here yields behavior that is strikingly similar to the experimental results, and is consistent with our conceptual picture.

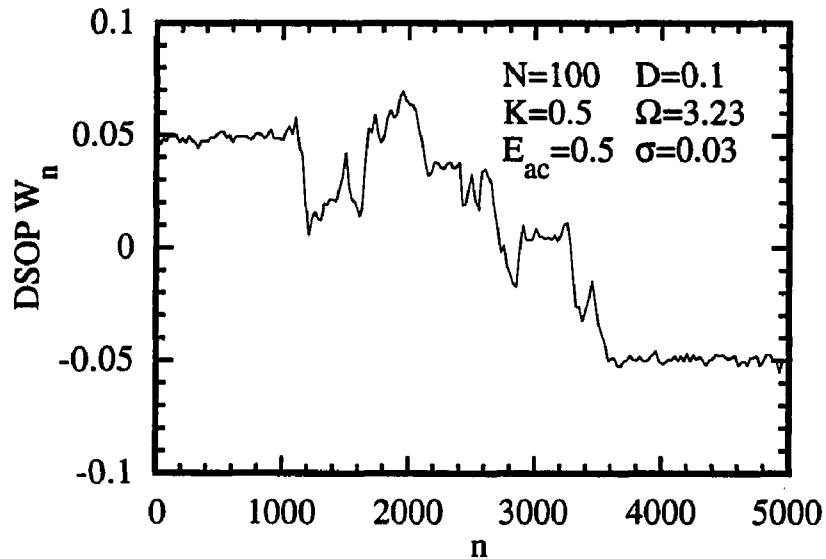


Figure 4.7: Plot of DSOP W_n for the coupled circle map, Eq. 4.4.

Domain walls in CDWs have in the past been shown to have their own particle-like attributes such as charge, mass and spin [82, 83]. The domain walls separating different degenerate attractors in subharmonically mode-locked CDWs are the dynamical analog of the solitons separating different degenerate ground states in commensurate CDWs like polyacetylene [83]. We speculate that domain walls we infer in mode-locked CDWs can be viewed as dynamical solitons. The CDW may be strained at the walls between degenerate attractors. In this case the dynamical solitons should carry a charge which may in principle be a fraction of an electron per chain [82].

The existence of high-order mode-locking observed in Fig. 4.3(c-f) leads us to speculate that the CDW may in fact be “completely” mode-locked, as is suggested by numerical simulations [29]. However, a more quantitative statement concerning the completeness of the mode-locking based on the data is beyond the scope of this thesis.

In conclusion, we see that Poincaré sections provide an invaluable tool for understanding physical systems that display complex nonlinear behavior involving many degrees of freedom. We have resolved a number of fundamental questions relating to mode-locking in CDWs. We have suggested that the subharmonically mode-locked CDW breaks up into domains separated by dynamical solitons. Clearly, many fruitful avenues for investigation remain in the study of mode-locked CDWs.

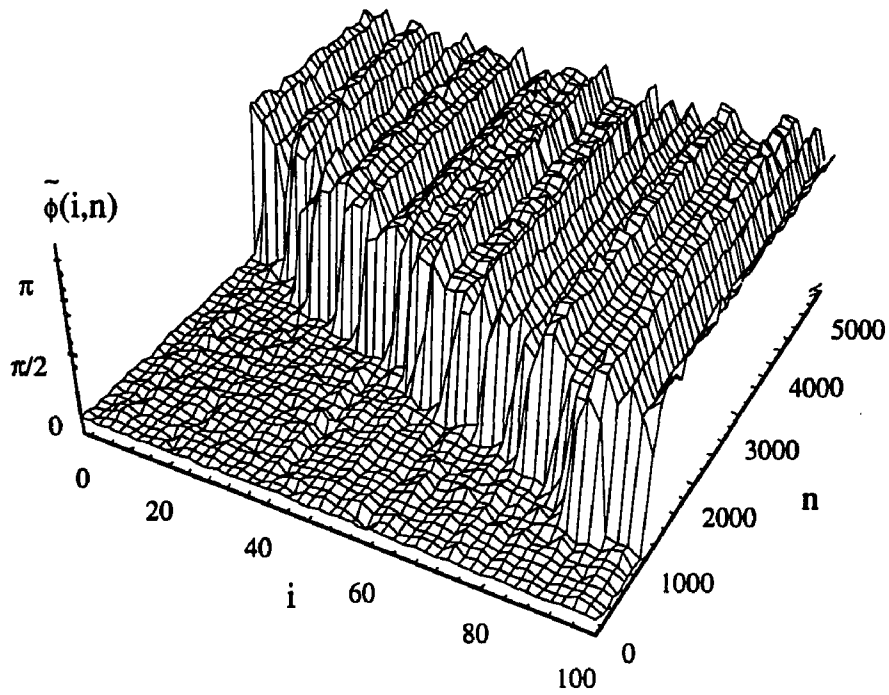


Figure 4.8: Plot of $\Delta\varphi \equiv \varphi(i, n) - \varphi(i, 0) - n\pi$ for n even. A “soliton-antisoliton” pair is created at $n = 1000$, spreading quickly to the right and more slowly to the left. The phase changes by $\pi + \rho_D(i)$, where $\rho_D(i)$ is the local DSOP. By $n = 2800$, the entire system has shifted attractors, corresponding to an overall change in sign in the DSOP.

Chapter 5

Low-Dimensional Chaos and High-Dimensional Behavior in the Switching Charge-Density-Wave Conductor NbSe_3

The dynamics of the switching charge-density wave (CDW) conductor NbSe_3 is studied in the presence of combined dc and ac electric fields. At a driving frequency of 20 MHz, the dynamics are both low-dimensional and chaotic, while at lower drive frequencies (<5 MHz) high-dimensional dynamics are observed. Analysis of the time series provides Lyapunov exponents, and an estimate for the number of active degrees of freedom for the low-dimensional chaotic behavior. The principal nonlinearity which gives rise to the low-dimensional chaos in switching CDWs is shown to be the hysteresis in the depinning transition, rather than the interaction between two frequencies.

5.1 Introduction

Sliding charge-density-wave (CDW) conductors [84] have played a central role in the study of spatially-extended dissipative nonlinear dynamical systems. In most treatments, the CDW is regarded as a classical deformable medium pinned by randomly-spaced impurities [80]. When a dc electric field E_{dc} greater than a threshold E_t is applied, the CDW depins and

slides with an average velocity v . In most samples of NbSe_3 the depinning transition is smooth. In so-called switching samples, the depinning transition becomes hysteretic at low temperatures. In the sliding state, the interaction of the CDW with impurities produces current oscillations or “narrow-band noise” of frequency $\omega_{\text{nbn}} \propto v$.

Rich dynamical behavior has been observed when the CDW is driven by combined dc+ac electric fields [85] in the non-switching regime. Mode-locking [86] occurs when ω_{nbn} becomes locked to a rational multiple of the external drive frequency ω_{ex} over a finite range of parameters. In a related phenomenon known as the pulse-duration memory effect [87], a train of identical square voltage pulses of width T causes the CDW current to synchronize to the end of each pulse. The source of nonlinearity in these phenomena is the interaction between two frequencies: ω_{nbn} and ω_{ex} for mode-locking, and ω_{nbn} and $1/T$ for the pulse-duration memory effect. It is widely accepted that many degrees of freedom are crucial to an understanding of mode-locking [73] and the pulse-duration memory effect [88, 89] in CDWs. Our earlier experimental study [90] showed explicitly the importance of many degrees of freedom in the dynamics of the subharmonically mode-locked state.

Samples in the switching regime behave in a dramatically different fashion under excitation by combined dc and sinusoidal ac electric fields. Previous studies reported several kinds of power spectra that are not observed in the non-switching regime. For $\omega_{\text{ex}}/2\pi > 5$ MHz, a period-doubling route to chaos was inferred from a sequence of power spectra containing structure at harmonics and subharmonics of ω_{ex} [48]. At lower driving frequencies, observed power spectra were broad-band, with noise amplitude much greater than conventional broad-band noise, and relatively featureless between harmonics of ω_{ex} . The latter spectra were called “ac switching noise.” Such power spectra have never been observed in the non-switching regime.

In this chapter, we report a time-domain study of the currents induced in switching samples of NbSe_3 by combined dc and ac fields. The questions we address are:

- 1) How many degrees of freedom are involved in the measured dynamics?

Powerful tools that have been developed for the analysis of chaotic time series enable one to answer this question based on the data alone, without reference to any particular model. We find that the behavior previously identified as chaotic is in fact low-dimensional. The low-dimensional data are consistent with the dynamics of two coupled first-order nonlinear ordinary differential equations with periodic driving and noise. The behavior previously identified as “ac switching noise” is high-dimensional, and is indistinguishable from random noise based on the data alone.

- 2) What is the principal source of nonlinearity that underlies the observed dynamics?

Both the low- and high-dimensional dynamics occur only when the ac field drives the sample repeatedly through the switch in the I - V curve. We show that the low-dimensional chaos arises because the depinning time varies in a chaotic fashion from one cycle to the next. This behavior is reminiscent of the delayed conduction that occurs on application of a

square voltage pulse to a switching sample [91]. Such a delayed transition occurs only if there is hysteresis in the depinning transition. Thus we conclude that the principal nonlinearity underlying the chaotic dynamics is the hysteresis in the depinning transition, rather than the interaction between ω_{nbn} and ω_{ex} . In the high-dimensional behavior, the depinning transition always occurs at approximately the same phase of the external drive. The largest cycle-to-cycle variability in the high-dimensional signal occurs near the middle of the time interval over which the CDW is sliding. The mechanism underlying the high-dimensional dynamics is unclear.

The remainder of the chapter is organized as follows: in section 5.2, we describe the experimental techniques used. In section 5.3, we describe the time-domain measurements as well as other more conventional measurements such as differential conductance and power spectra measurements. In section 5.4, the chaotic data is characterized using recently-developed methods of time-series analysis, and implications of our results for competing models of switching CDW dynamics is discussed.

5.2 Experimental Technique

In order to perform time-domain measurements of CDW currents, it is important to reduce or eliminate every source of external noise. Standard noise-reduction techniques such as signal averaging, lock-in amplification, bandpass filtering, etc., generally cannot be used because real-time information is lost or distorted. The signals of interest are quite small ($\sim 1\text{--}10\ \mu\text{A}$) and high frequency (1–100 MHz); furthermore, they reside atop of relatively large sinusoidal signals (mainly due to the response of normal carriers). Noise reduction is achieved through careful shielding and by reducing input noise at the amplifier stages. The experiments were performed inside a Faraday cage to reduce rf interference from radio stations, computers, and other high-frequency noise sources. Only analog components were placed inside the cage, because the clocks from digital equipment can produce significant interference.

Nominally pure crystals of NbSe_3 were mounted on a ceramic microstripline in a two-probe voltage-driven configuration. The ac signals were terminated by a $50\ \Omega$ resistor on one end of the sample. The voltage across a $50\ \Omega$ resistor on the other end of the sample was measured with a Miteq AU-1310 low-noise preamplifier with a 500 MHz bandwidth and a maximum noise figure of 1.4 dB. Semi-rigid coax cables were fed directly to and from the microstripline launchers. The samples were sealed inside a 4 1/2 in. conflat flange filled with 1 atm. of Helium gas to minimize the effects of ohmic heating. The sample was driven by combined dc and ac voltages:

$$V(t) = V_{\text{dc}} + V_{\text{ac}} \sin(\omega_{\text{ex}} t) \quad (5.1)$$

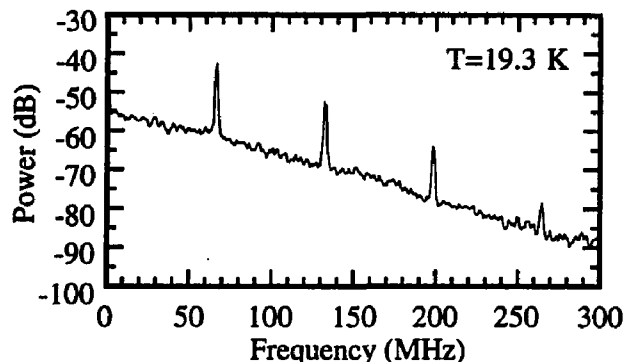


Figure 5.1: Power spectrum of current oscillations for sample No. 1 at $T=19.3$ K ($R=375$ Ω at $T=47.7$ K, length=1.8 mm).

The majority of the fundamental signal at ω_{ex} was subtracted off with a high-speed differential amplifier. The resulting signal was further amplified and digitized once per drive cycle using a Tektronics RTD710 digitizer, yielding a time series of the current. The signal was also digitized at a much higher rate, using a Tektronics DSA602 digital signal analyzer. Power spectra were measured with a HP-4195A (sweeping filter) spectrum analyzer.

Two samples (No. 1 and No. 2) from separate growths were investigated, although we will only present results for sample No. 1. Comparisons between the response of the two samples will be made where appropriate. Samples were selected which displayed a single switch. Fig. 5.1 shows a power spectrum of the narrow-band-noise for sample No. 1 at $T=19.3$ K in the absence of ac driving. The 3 dB width of the narrow-band-noise oscillations is approximately 10^3 , indicating a highly homogeneous distribution of CDW velocities within the sample.

5.3 Experimental Results

5.3.1 Differential Conductance Measurements

This section describes measurements of the differential conductance as a function of temperature. Because the samples were voltage-driven, the direct measurement was made of the differential conductance dI/dV , rather than the differential resistance dV/dI . Figs. 5.2(a-c) show the differential conductance dI/dV in the absence (top traces) and presence (bottom traces) of ac driving for three temperatures. The frequency $\omega_{ex}/2\pi = 20$ MHz and amplitude $V_{ac} = 38.8$ mV were the same for all three temperatures.

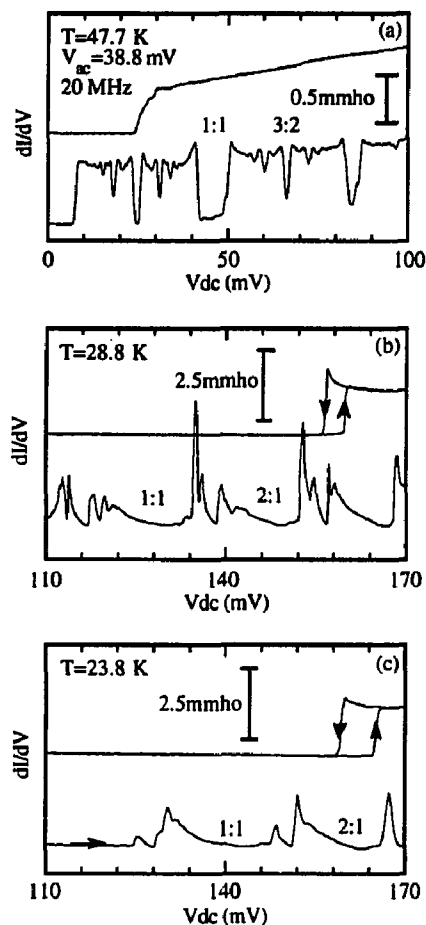


Figure 5.2: Differential conductance of sample No. 1 ($R=375 \Omega$ at $T=47.7$ K, length=1.8 mm) in the absence (top traces) and presence (bottom traces) of 20 MHz rf driving with amplitude $V_{ac} = 38.8$ mV. (a) $T=47.7$ K. Sample is non-hysteretic. There are many harmonic (e.g., 1:1) and subharmonic (e.g., 3:2, 1:3) mode-locked features, flanked by symmetric “wings”. (b) $T=28.8$ K. The sample is in the hysteretic regime, as indicated by the arrows. The mode-locked features are highly asymmetric, and many of the subharmonic features have disappeared. (c) $T=23.8$ K. The hysteresis loop has increased in size, and fewer subharmonic features remain.

In the top trace of Fig. 5.2(a), the CDW is pinned up to a threshold voltage $V_t=25.0$ mV, above which dI/dV monotonically increases and eventually saturates. At $T=47.7$ K, V_t is unique and non-hysteretic. The bottom trace shows dI/dV in the presence of ac driving. Mode-locking occurs when the frequency of the narrow-band noise ω_{nbn} becomes locked to the external drive frequency ω_{ex} . We define $p : q$ mode-locking as the condition $\omega_{nbn} = p/q \omega_{ex}$. When complete mode-locking occurs, the differential conductance dI/dV drops to its ohmic ($V_{dc} = V_{ac} = 0$) value. The 1:1 step is almost completely mode-locked, as is the 1:2 subharmonic step. The mode-locked steps are symmetric, and flanked by positive “wings” [72], which are associated with frequency pulling. There are also many other subharmonic features.

As the temperature is lowered to 28.8 K, the CDW conductance near V_t decreases, and a second, hysteretic threshold develops at a higher value of V_{dc} , as seen in the top trace of Fig. 5.2(b). The dc voltage V_{dc} has been swept in both directions, as indicated by the arrows. The width in voltage of the integrally (i.e., $p:1$) mode-locked steps increases manyfold, while the subharmonic mode-locked steps become less pronounced. However, one can still see remnants of the 2:3 and 3:4 steps, for example. Another noticeable feature is the asymmetry of the mode-locked steps. Both the integral and half-integral steps approach their ohmic limit slowly from the left, while the increase in dI/dV is large and sudden on the right. This asymmetry does not depend on which direction the bias is swept.

Fig. 5.2(c) shows dI/dV at $T=23.8$ K. As the temperature is lowered, the hysteresis loop increases in size, and the subharmonic steps become even less pronounced. The half-integral steps still remain at this temperature, but disappear at lower temperatures.

5.3.2 Detailed form of Chaotic Currents

The solid line in Fig. 5.3(a) shows the CDW current $I(t)$ measured at a high sampling rate when the CDW is in a chaotic state. The dotted line indicates the sinusoidal current that would result if the sample response were purely linear. The differential amplifier has subtracted out slightly more than the purely linear response, and thus the dotted line is 180° out of phase with the true linear response. The measured response is very close to sinusoidal for a fraction of each cycle, indicating that the CDW is pinned. The depinning transition is clearly visible in each cycle as a sharp increase in the current. The difference between the solid and dashed lines in Fig. 5.3(a) gives the instantaneous CDW current, the integral of which is plotted below in Fig. 5.3(b). The CDW displacement $u(t)$ is plotted in units of the CDW wavelength λ_{CDW} (where λ_{CDW} is determined from the fact that the CDW is locked at the 2:1 step). There are very large deviations in the total displacement from one cycle to the next, and yet the CDW current is uniform over long times. The amount of relaxation in the pinned state varies greatly from cycle to cycle, but patterns of motion are clearly visible. Fig. 5.3(c) plots the difference in current $I(t)$ shifted in time by

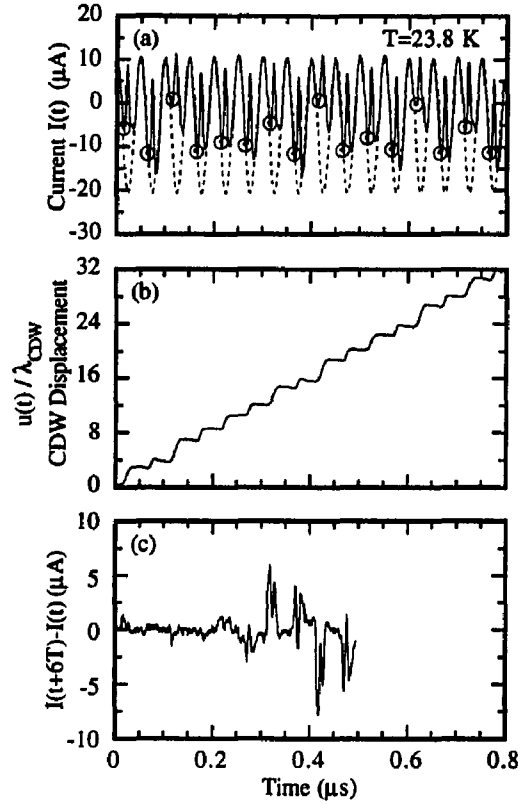


Figure 5.3: (a) High-sampling-rate measurement of CDW current versus time, after subtraction of most of fundamental at 20 MHz. Parameters are $\omega_{ex}/2\pi=20$ MHz, $V_{ac} = 38.8$ mV, $V_{dc} = 163.6$ mV. The CDW is mode-locked at the 2:1 step. Dashed lines indicate ohmic component of the signal. Note that after subtraction, effective ohmic resistance is actually *negative*. The difference between the solid line and the dashed line is the excess current due to sliding of the CDW. Open circles indicate where time series was obtained. (b) CDW displacement $u(t)$, measured in units of the CDW wavelength λ_{CDW} , versus time, obtained by integrating the CDW current in (a). Fluctuations in the cycle-to-cycle CDW displacement are of order 100%, but the time-averaged displacement is two wavelengths per drive cycle. (c) Deviation of CDW current $I(t)$ for two “nearby” initial configurations displaced in time by $6T$. There is a sensitive dependence on initial conditions characteristic of chaotic behavior.

six periods of the ac driving. The deviation is initially small, indicating that the CDW is nearly in the same configuration, but small differences are magnified in time, and one sees the sensitive dependence on initial conditions that is indicative of chaotic behavior. A more quantitative measure of the chaotic nature of this attractor will be presented in Sec. 5.4

5.3.3 Period-Doubling Route to Chaos

The real-time traces plotted in Fig. 5.3(a) contain more information on a short time scale than is necessary for characterizing a chaotic attractor. For example, the fact that the CDW is pinned for more than half of the drive cycle means that half of the time series conveys almost no information. In fact, by sampling the current just once per drive cycle, one can obtain almost all of the essential information about the state of the system. If the resulting time series

$$\{I_n \equiv I(t = nT + t_0), n = 1, 2, \dots, N\} \quad (5.2)$$

is plotted versus a control parameter, one obtains a bifurcation diagram. Fig. 5.4(b) shows such a diagram: $N = 128$ points of the time series for the drive parameters in Fig. 5.2(c) are plotted vertically for 150 evenly-spaced values of V_{dc} , yielding the characteristic signature for a period-doubling route to chaos. The corresponding values of dI/dV are plotted above, in Fig. 5.4(a). The first period-doubling bifurcation occurs at $V_{dc} = 154$ mV. The inset to Fig. 5.4(a) shows the power spectrum of the time series for $V_{dc} = 156.3$ mV. A sharp peak occurs at 10 MHz, flanked by narrow-band noise peaks which suggest that the CDW is not locked. The separation increases until $V_{dc} = 159$ mV, where a second period-doubling bifurcation takes place. The bifurcation in the lower branch is too narrow to be seen here. At $V_{dc} = 162$ mV, the onset of chaotic behavior is observed. The chaotic signal splits into two bands at $V_{dc} = 166$ mV, and ends with an abrupt increase in the time-averaged current.

Embedding the time series in two dimensions by plotting I_n versus I_{n+1} yields a visual reconstruction of the Poincaré section of the attractor. Figs. 5.5(a-d) show such an embedding for four values of V_{dc} . The corresponding measurements of the power spectra are plotted below, in Figs. 5.5(e-h). Fig. 5.5(a) shows period-one behavior at $V_{dc}=153.1$ mV, characterized by a single point in the Poincaré section. The lower right corner shows the Poincaré section when the CDW is locked in the 0:1 state (i.e., not sliding). The power spectrum below in Fig. 5.5(e) shows a peak at the fundamental frequency 20 MHz, as well as some narrow peaks due to the mixing of the narrow-band noise with the drive. One can also see a fairly broad feature at 10 MHz. This is a “noisy precursor” of the period-two behavior, indicating that the CDW is close to a bifurcation point [92]. Fig. 5.5(b) shows the system at the $V_{dc}=157.4$ mV, after the first period-doubling bifurcation, with two corresponding period-two points. The power spectrum below in Fig. 5.5(f) shows a large peak at 10 MHz, corresponding to the period-two behavior. There are also two fairly broad features centered at 5 MHz and 15 MHz. These are noisy precursors of the period-4 behavior. Fig. 5.5(c)

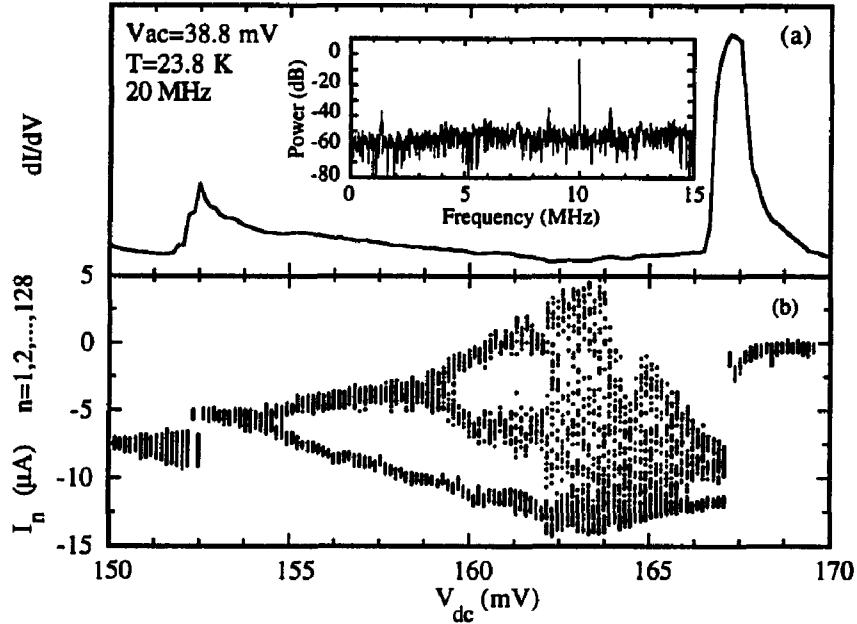


Figure 5.4: (a) Close-up of dI/dV near 2:1 mode-locked step. Inset shows power spectrum of time-series obtained at $V_{dc} = 156.3$ mV. (b) Bifurcation diagram constructed from time series. Successive points of time series plotted versus V_{dc} (see text for discussion).

shows period-four behavior at $V_{dc} = 161.3$ mV. The points are highly elongated, indicating that they are close to being unstable. The corresponding power spectrum in Fig. 5.5(g) shows four peaks, and there is a noticeable rise in the noise level, indicating that the system is near to becoming chaotic. Fig. 5.5(d) shows a chaotic attractor at $V_{dc} = 163.6$ mV. The two leaves of the attractor visible in the left half are the remnants of the two barely-stable fixed points on the left half of Fig. 5.5(c). The attractor is approximately one-dimensional, with one fold visible on the left. The steep slope on the left is indicative of chaos. The power spectrum in Fig. 5.5(h) is now broadband with broad peaks remaining at multiples of $f/4$ [48].

Measurements were made on a second sample No. 2. Both the period-doubling cascade and the shape of the chaotic attractor seen for sample No. 2 are nearly identical to that of sample No. 1. We conclude that the chaotic behavior is unrelated to defects or peculiarities of particular samples [93].

Figs. 5.6(a-d) show a similar period-doubling cascade for $T = 28.8$ K near the 2:1 mode-

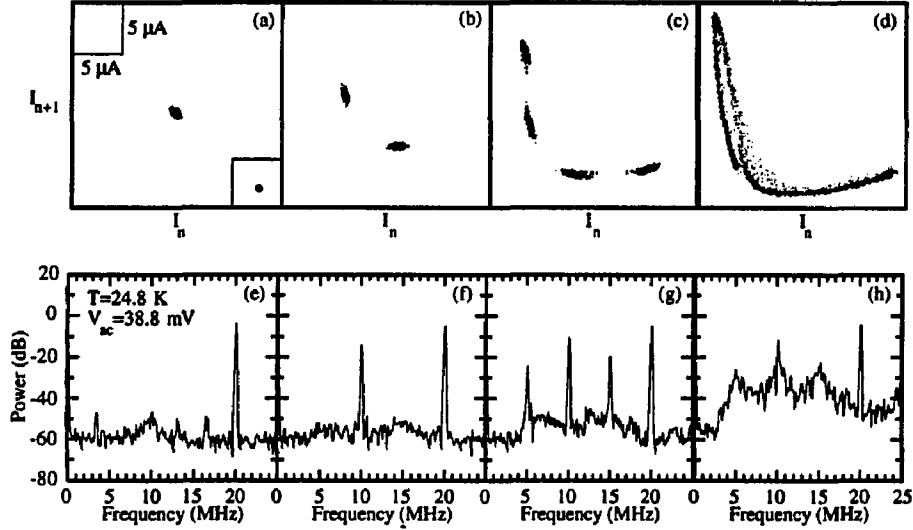


Figure 5.5: Time-delay reconstruction of Poincaré section from time series, and corresponding analog power spectra (below) at $T=23.8 \text{ K}$ and $\omega_{ex}/2\pi=20 \text{ MHz}$ (see text for discussion). (a,e) $V_{dc}=153.1 \text{ mV}$. (b,f) $V_{dc}=157.4 \text{ mV}$. (c,g) $V_{dc}=161.3 \text{ mV}$. (d,h) $V_{dc}=163.6 \text{ mV}$.

locked step, corresponding to the dI/dV curve plotted in Fig. 5.2(b). The corresponding analog power spectra are plotted below in Figs. 5.6(e-h). In Fig. 5.6(a), the first period-doubling bifurcation has just occurred. The power spectrum in Fig. 5.6(e) shows a peak at 10 MHz, corresponding to the period-two behavior, but also shows several unlocked peaks, indicating the CDW is unlocked. In Fig. 5.6(b), the period-two behavior is quite large, and the two points themselves are on the verge of becoming unstable. The same noisy precursors are evident in Fig. 5.6(f) as in Fig. 5.5(f). The period-four behavior is quite robust in Fig. 5.5(c), and the power spectrum in Fig. 5.6(g) shows distinct peaks which are roughly 30 dB above the noise floor. In Fig. 5.6(d), the period-four points are nearly unstable, as evidenced by their elongated shape. In the power spectrum in Fig. 5.5(h), one can see evidence of period-8 behavior. The period-doubling sequence ends before the onset of any chaotic behavior. At higher temperatures, such as $T=32.7 \text{ K}$, the hysteresis loop is negligibly small, and only period-two behavior is observed.

5.3.4 High-Dimensional Dynamics

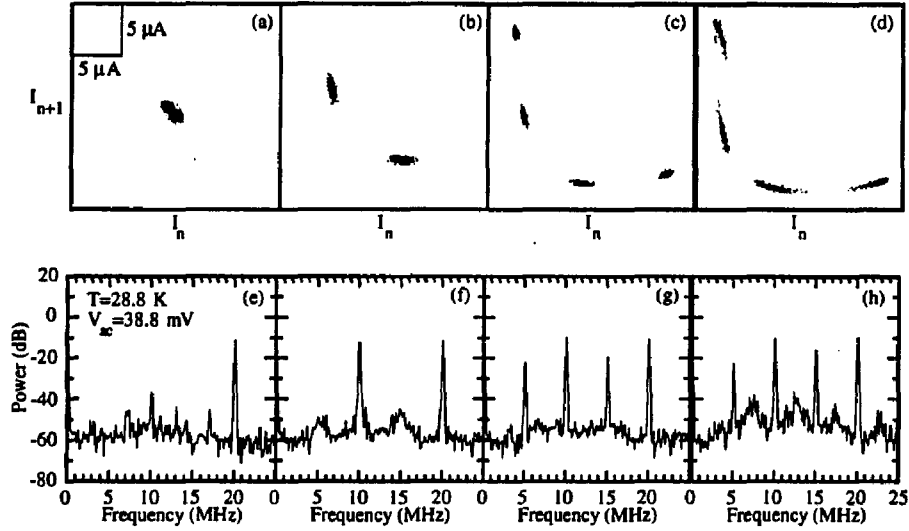


Figure 5.6: Time-delay reconstruction of Poincaré section from time series, and corresponding analog power spectra (below) at $T=28.8 \text{ K}$ (see text for discussion). (a,e) $V_{dc}=141.4 \text{ mV}$. (b,f) $V_{dc}=145.7 \text{ mV}$. (c,g) $V_{dc}=148.6 \text{ mV}$. (d,h) $V_{dc}=150.2 \text{ mV}$.

At driving frequencies below a characteristic crossover frequency (for sample No. 1, at about 5 MHz), the behavior is quite different. The top trace in Fig. 5.7(a) shows the differential conductance at $\omega_{ex}/2\pi=4 \text{ MHz}$ and $V_{ac}=43.0 \text{ mV}$. Time series were measured at two phases with respect to the rf driving, one near the depinning transition, $\{I_n^{depin}\}$, and the other near the maximum of $I(t)$, $\{I_n^{max}\}$. Fig. 5.7(b) shows the rms magnitude of the measured time series for both $\{I_n^{depin}\}$ and $\{I_n^{max}\}$. Also shown is the rms noise from 0 MHz to 20 MHz, measured by an analog spectrum analyzer. Multiples of the fundamental frequency 4 MHz were not included in the average. The curves are shifted arbitrarily for clarity, but the scale for both time series is the same. For values of V_{dc} near threshold, we observe broadband, almost featureless “ac switching noise” which can be 10–20 dB larger than the broadband noise observed in the absence of rf driving [48]. This noise is observed in $\{I_n^{max}\}$, but not in $\{I_n^{depin}\}$. Likewise, at higher V_{dc} , low dimensional behavior is observed in $\{I_n^{depin}\}$, while $\{I_n^{max}\}$ shows essentially no signal.

Figs. 5.8(a–b) show high-sampling-rate measurements of the current versus time for two different values of V_{dc} . The dashed line indicates the response that is linear in the voltage $V(t)$. More than the ohmic contribution to the current has been subtracted, so that the

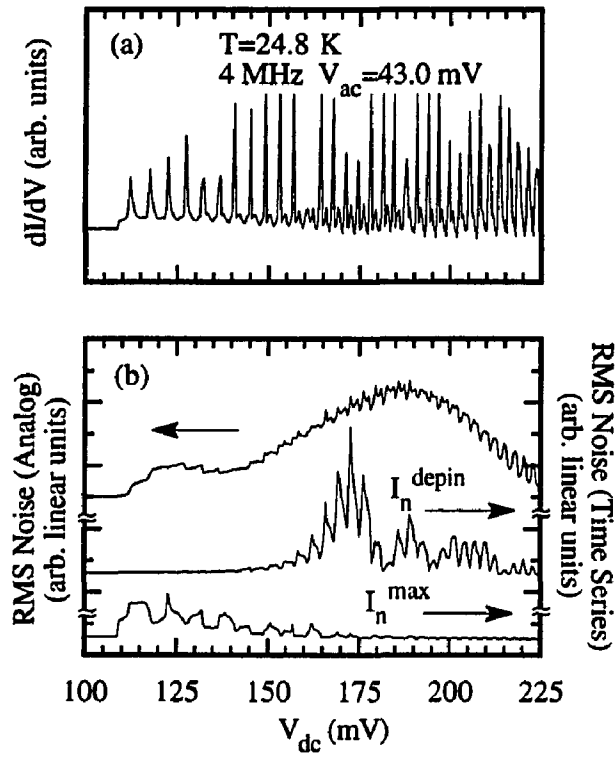


Figure 5.7: (a) Differential conductance dI/dV at $T=23.8$ K for $\omega_{ex}/2\pi=4$ MHz, $V_{ac}=43.0$ mV. (b) RMS noise from both analog power spectrum and time series measured at two different phases with respect to the drive. For $\{I_n^{max}\}$, the signal is large near the depinning threshold, while for $\{I_n^{depin}\}$ the signal becomes larger at higher values of V_{dc} .

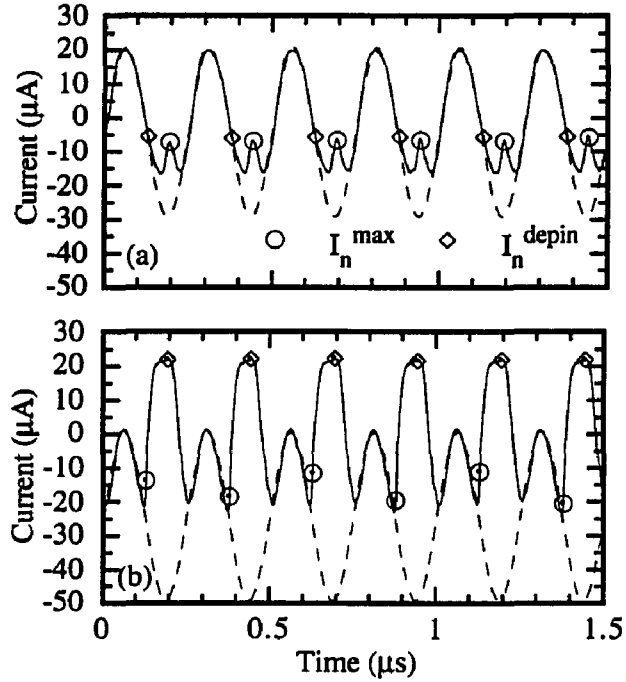


Figure 5.8: (a) High-sampling-rate measurement of CDW current versus time, after subtraction of most of fundamental, for regime where high-dimensional signal is large (see text for discussion). Parameters are $\omega_{ex}/2\pi=4$ MHz, $V_{ac} = 43.0$ mV, $V_{dc} = 117.1$ mV. Dashed lines indicate ohmic component of the signal. Note that after subtraction, effective ohmic resistance is actually *negative*. Circles indicate time-series obtained near depinning transition $\{I_n^{\text{depin}}\}$. Diamonds indicate time-series obtained near maximum of $I(t)$ $\{I_n^{\text{max}}\}$. Same as (a), but for $V_{dc} = 202.2$ mV, where the low-dimensional signal is large.

actual time-dependent voltage $V(t)$ is 180° out of phase with respect to the dashed line. In Fig. 5.8(a), the CDW is depinned for a small fraction of the drive cycle, while in Fig. 5.8(b), the CDW is depinned for more than half of the drive cycle. Time series were measured at two phases with respect to the rf driving, one near the depinning transition ($\{I_n^{\text{depin}}\}$, illustrated by circles), and the other near the maximum of $I(t)$ ($\{I_n^{\text{max}}\}$, illustrated by diamonds).

Fig. 5.9(a) shows a close-up of dI/dV in a region near threshold. Figs. 5.10(a-c) show visual reconstructions of the attractor for values of V_{dc} indicated by the letters A-C in Fig. 5.9(a), respectively. The main plots show the measured signal for $\{I_n^{\text{max}}\}$. The corresponding analog power spectra are plotted below, in Figs. 5.10(d-f). In Fig. 5.10(a), the CDW is pinned, and the corresponding signal is small. The only structure in the power spectrum shown in Fig. 5.10(d) is the fundamental frequency at 4 MHz. In Fig. 5.10(b), the signal is large, and with very little structure. There are correlations in the time series, as indicated by the slightly elliptical shape of the Poincaré section. The lower right insets of Figs. 5.10(a-c) show the Poincaré reconstruction from time series $\{I_n^{\text{depin}}\}$. The signals are very small, mostly due to the fact that the digitization has occurred slightly before the depinning transition. However, from Fig. 5.8(a) one can see that even at the depinning transition there is essentially no cycle-to-cycle deviation, suggesting that the high-dimensional signal does not originate from dynamics occurring near the depinning transition.

Fig. 5.9(b) shows a close-up of dI/dV at a higher field. Figs. 5.11(a-c) show visual reconstructions of the attractor for values of V_{dc} indicated by the letters A-C in Fig. 5.9(b), respectively. The main plots show the Poincaré reconstruction from time series $\{I_n^{\text{depin}}\}$. The corresponding analog power spectra are plotted below, in Figs. 5.11(d-f). In this regime of V_{dc} the period-doubling sequence is recovered. Figs. 5.11(a-c) show period-one, period-two, and chaotic behavior, respectively. The shape of the chaotic attractor is similar in shape to the one shown in Fig. 5.5(d). The lower right insets of Fig. 5.10(a-c) show the Poincaré reconstruction from time series $\{I_n^{\text{max}}\}$. The signal at this phase of the rf drive is not larger than the instrumental noise.

5.4 Analysis

More quantitative methods of time series analysis [94] were applied both to the time series plotted in Figs. 5.5(d) and 5.10(b). Of these methods, we found direct nonlinear modeling of the time series the most useful [95]. We used a local-linear predictor [96, 97], trained on the first half of a segment of the data, and computed the average rms error for one-step-ahead prediction on the second half the the data segment. Fig. 5.12(a) shows this error as a function of embedding dimension for the data of Fig. 5.5(d). There is no significant reduction of error for embedding dimensions larger than $m = 2$, suggesting that an adequate model of the dynamics can be constructed with only two degrees of freedom. Furthermore,

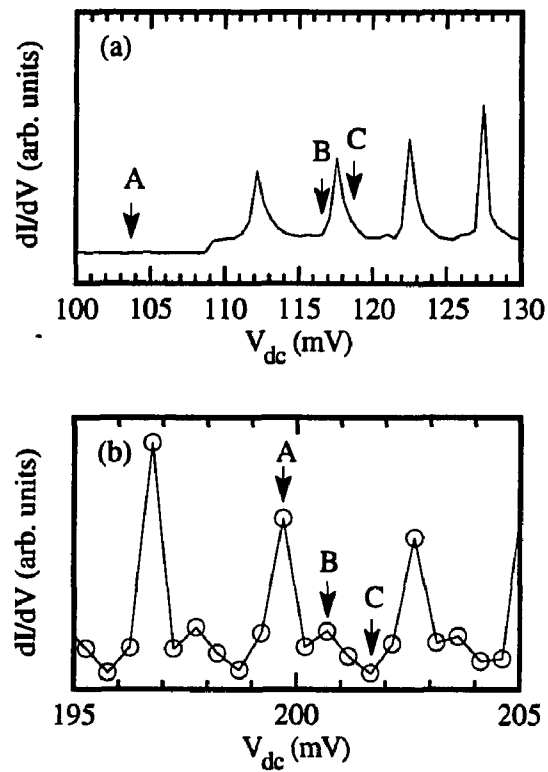


Figure 5.9: (a) Close-up of dI/dV near region which shows high-dimensional behavior. Letters A-C refer to Poincaré sections shown in Figs. 5.10(a-c), respectively. (b) Close-up of dI/dV near region which shows low-dimensional behavior. Letters A-C refer to Poincaré sections shown in Figs. 5.11(a-c), respectively.

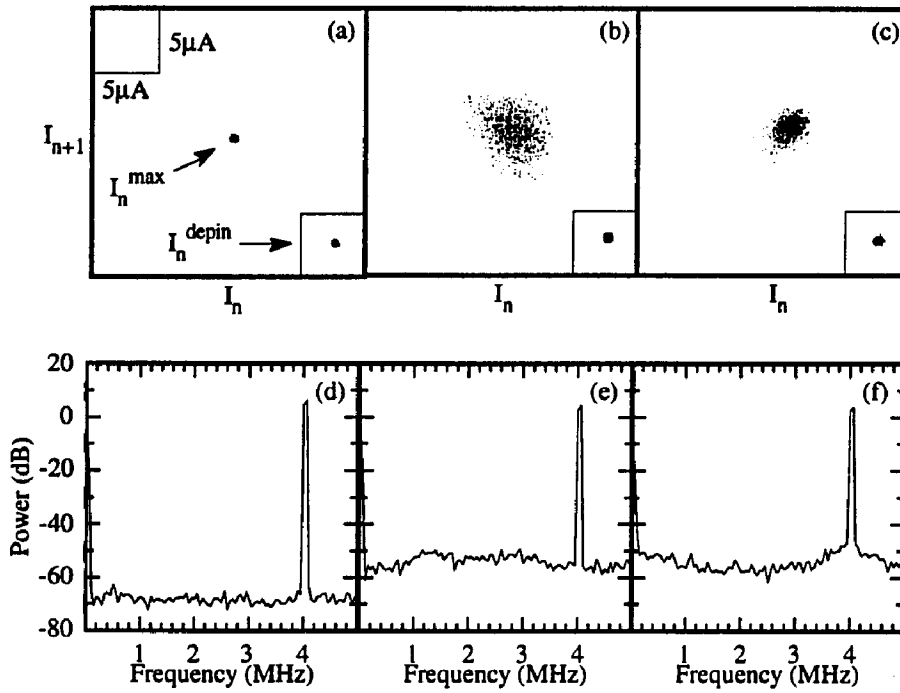


Figure 5.10: Time-delay reconstruction of Poincaré section from time series, and corresponding analog power spectra (below) at $T=23.8$ K and $\omega_{ex}/2\pi$ (see text for discussion). Main plot in (a-c) shows Poincaré section for time delay near maximum of $I(t)$ $\{I_n^{\text{max}}\}$, while lower right corner shows Poincaré section for time delay near depinning transition $\{I_n^{\text{depin}}\}$ (see Fig. 5.8). (a,d) $V_{dc}=103.8$ mV. (b,e) $V_{dc}=117.1$ mV. (c,f) $V_{dc}=118.6$ mV.

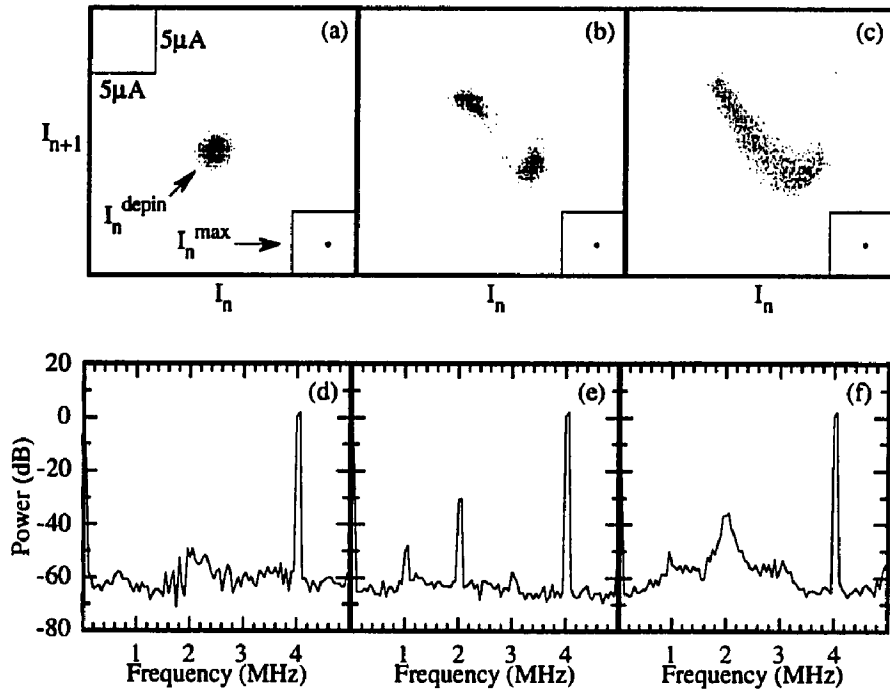


Figure 5.11: Time-delay reconstruction of Poincaré section from time series, and corresponding analog power spectra (below) at $T=23.8$ K and $\omega_{ex}/2\pi=4$ MHz (see text for discussion). Main plot in (a-c) shows Poincaré section for time delay near depinning transition $\{I_n^{depin}\}$, while lower right corner shows Poincaré section for time delay near maximum of $I(t)$ $\{I_n^{max}\}$ (see Fig. 5.8). (a,d) $V_{dc}=199.7$ mV. (b,e) $V_{dc}=201.2$ mV. (c,f) $V_{dc}=202.2$ mV.

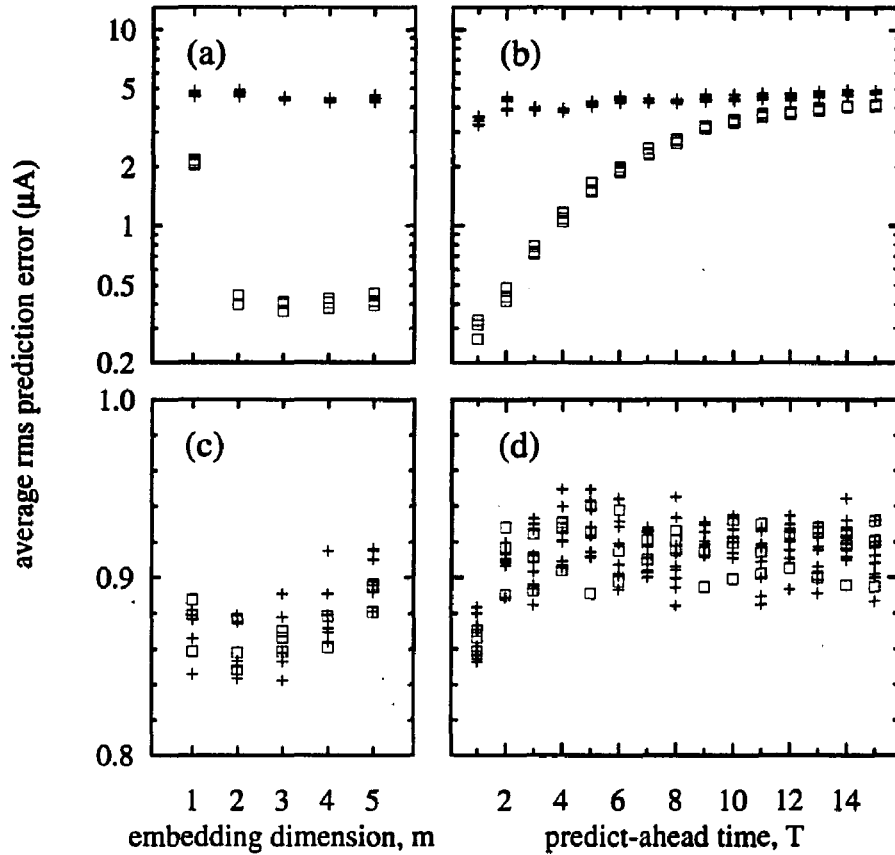


Figure 5.12: (a) One-step-ahead rms forecasting error versus embedding dimension m for the low-dimensional data shown in Fig. 5.5(a). The data sets are taken from non-overlapping segments of length $N = 4096$. Predictions on points in the last half of the segment are based on local linear fits using the $k = 30$ nearest neighbors in the first half of the segment. (This value of k was chosen because it gave the best predictions.) Different segments of the original data set are indicated by squares (\square). The same computations were made with surrogate data, indicated by pluses ($+$). (b) Forecasting error as a function of forecasting time T for length $N = 4096$ segments of the experimental time series (\square) and for surrogate data ($+$). The approximately exponential increase in error with T suggests a positive metric entropy in the dynamics of about 0.6 bits per time step. Note that no such behavior is observed in the surrogate data sets. (c-d) Same as (a-b), except for the data shown in Fig. 5.10(b). This data is evidently high dimensional, and is numerically indistinguishable for surrogate data.

the $m = 2$ dimensional local linear model makes predictions with an average rms error of $0.4\mu\text{A}$, which is about 7% of the signal's rms amplitude. This provides a measure of the underlying noise in the signal. We define "noise" operationally here to mean unpredictable signal. It is of course possible that some of this noise is modeling error (though we obtain essentially the same result with both longer and shorter data segments), but we can in any case assert that the signal to noise (power) ratio is at least 23 dB. This signal to noise ratio should be compared that obtained by comparing the time series for Fig. 5.5(a) with that for Fig. 5.5(d), which is 30 dB. Also shown in Fig. 5.12(a) is the same computation applied to "surrogate data." These are random data sets which have been artificially generated to have same Fourier power spectrum and amplitude distribution as the original data [98]. The large difference between results on real and surrogate data indicates that the nonlinear structure detected by the prediction algorithm is significant.

In Fig. 5.12(b), we compute forecasting error as a function of predict-ahead time T and find that the error increases approximately exponentially for small T . Following Ref. [97], we associate this rate of increase with the largest Lyapunov exponent, and estimate its value at about 0.6 bits per period. We have found this value to be robust (± 0.1 bits) to variation in embedding dimension, number of nearest neighbors in the local linear prediction algorithm, and the length of the data segment. We take this positive value as an indication of chaos [99].

The high-dimensional time series shown in Fig. 5.10(b), by contrast, exhibits no evidence for nonlinear predictable structure. Figs. 5.12(c-d) show the variation of prediction error with embedding dimension and predict-ahead time, respectively. Comparison of these computations with those for surrogate data shows no significant difference. We have compared this data to surrogate data using several other discriminating statistics, including estimated correlation dimension, and again are unable to make a distinction. From the data alone, there is no evidence to reject a null hypothesis of linearly correlated noise. However, the high-dimensional signal is clearly larger than the instrumental noise, and is thus attributed to the dynamics of the sliding CDW.

In earlier papers on ac-driven switching CDWs, the low-dimensional chaos was associated with mode-locking of the narrow-band noise [48]. Mode-locking in both the switching and non-switching regime was analyzed within the paradigm of the "circle map" [41], a one-dimensional map of the form:

$$\theta_{n+1} = \theta_n + \Omega + \frac{K}{2\pi} \sin 2\pi\theta_n, \quad (5.3)$$

where θ_n corresponds to the (single coordinate) phase of the CDW at $t = nT$. Mode-locking in the non-switching regime corresponded to $K < 1$, in which Eq. (5.3) exhibits mode-locking but no chaos, while mode-locking in the switching regime corresponded to $K > 1$, where period-doubling and chaotic behavior is observed in Eq. (5.3). A more sophisticated treatment was proposed by Inui *et al.* [56], which included amplitude degrees

of freedom and exhibited a period doubling route to chaos. Common to both models is the fact that the period-doubling route to chaos occurs when the system is mode-locked.

Our results indicate that the period-doubled and chaotic behavior have little to do with the current oscillations that give rise to mode-locking in the non-switching regime. The magnitude of the chaotic signal is much larger than the narrow-band noise, and comparable to the magnitude of the switch. The chaotic signal occurs only when V_{ac} is of a magnitude that repeatedly drives the CDW through the switch. A close examination of Fig. 5.3 shows that the phase (time modulo T) at which the CDW switches varies from cycle to cycle. These variations in the switching times account for almost all of the chaotic signal measured at the Poincaré sampling times.

There is also evidence that the CDW is not mode-locked during period-doubling. The power spectrum of the time series (5.2) at $V_{dc}=156.3$ mV, shown in the inset to Fig. 5.4(a), simultaneously displays an instrumentally narrow signal at $\omega_{ex}/2=10$ MHz, and 35 kHz wide peaks at 10 ± 1.3 MHz. We interpret the signal at 10 MHz as a period-doubling of the switching phase, and the other peaks as unlocked narrow-band noise (modulo the driving frequency) mixed with ω_{ex} and $\omega_{ex}/2$. An alternative explanation is that period-doubling of the narrow-band noise in a mode-locked portion of the sample gives rise to the instrumentally narrow peak at $\omega_{ex}/2$. We find this scenario unlikely due to the large separation of the narrow-band noise peak from any observed subharmonic of ω_{ac} . Also, the amplitude of the peak at $\omega_{ex}/2$ does not fluctuate in time, but is a direct function of the bias V_{dc} , as seen in Fig. 5.4. Amplitude fluctuations are generic in subharmonically mode-locked samples at higher temperatures, and have been interpreted as transitions between different mode-locked configurations [100].

The origin of the high-dimensional behavior, and the associated “ac switching noise,” is less clear. The relevant experimental results are the following:

1. High-dimensional behavior occurs only for ω_{ex} below a characteristic frequency. This frequency is sample-dependent. For sample No. 1, it was near 5 MHz, while for sample No 2, it was near 10 MHz.
2. The high-dimensional behavior occurs when the CDW is partly locked.
3. There are oscillations in the amplitude of the noise as a function of dc voltage, with a period of oscillation equal to approximately twice the width of a single mode-locked step, as shown in Fig. 5.8(b).
4. The noise is large when sampled near the maximum of $V(t)$, and small near the depinning transition.
5. The noise is large near threshold, and decreases at higher V_{dc} .

Observations (1) and (2) may be related, because mode-locking is generally more difficult to achieve at very low frequencies. It is actually somewhat surprising that mode-locking occurs at all in switching samples at these low driving frequencies. Since a switching CDW jumps to a high velocity when it depins, the narrow-band noise jumps in at a frequency that is typically several tens of MHz. In a $n:1$ mode-locked state, the CDW must advance n wavelengths per drive period. If the characteristic narrow-band noise frequency in the sliding state is much higher than the external driving frequency, then a low-order mode-locked step must correspond to the CDW being depinned for only a small fraction of the driving period. This can be qualitatively seen in Fig. 5.8(a).

It is possible that the high-dimensional behavior only occurs in “imperfect” samples, in which the cross-section exhibits one or many thickness steps, the mechanism being similar to that which produces broadband noise in the absence of rf driving [30]. Given the delicate nature of low-order mode-locking at low driving frequencies, it is possible that the high-dimensional behavior is originating from unlocked portions of the CDW. As V_{dc} is increased and the CDW is depinned for a larger fraction of a cycle of the external drive, the mode-locking actually improves (see dI/dV in Fig. 5.7(a)) and the noise amplitude decreases (although at high fields the noise is small even when the CDW is unlocked.) Observation (5) is consistent with the imperfect sample hypothesis, because broadband noise displays a similar dependence on V_{dc} . Even if the high-dimensional behavior is caused by sample imperfections, one must still explain why the amplitude of the ac switching noise is 10–20 dB larger than broad-band noise induced by a dc voltage. Observation (3) is quite mysterious, but may be related to systematic variations of nodes and maxima in the current oscillations relative to the fixed phase at which the current is recorded.

Observations (4) and (5) suggest that the high-dimensional noise and the low-dimensional behavior have different physical mechanisms. The fact that the noise is high-dimensional implies that many degrees of freedom are involved, in contrast to the low-dimensional chaos.

Several models of switching CDWs have been proposed in the literature, [41, 56, 57] including our own recently proposed unified model of switching and non-switching CDW dynamics [101]. However, none of these models has yet been successful in capturing even the qualitative behavior that we have observed. The reproducibility of the chaotic attractor shown in Figs. 5.5(d) provides strong quantitative constraints on any theory of switching CDW dynamics.

Fig. 5.3 provides clues to a qualitative understanding of the origin of the chaotic response. The cycle-to-cycle variation of the phase of the switch is reminiscent of previous experiments on the response of switching CDWs to square voltage pulses [91]. In those experiments, the CDW switched only after a delay τ which varied over several orders of magnitude for identical external parameters. The interpretation was that the τ were determined by the configuration of the pinned CDW prior to the voltage pulse. The phase of the switch in the chaotic state may also be determined by the previous configurations of the CDW. The low-

dimensional nature of the chaotic response leads us to speculate that the underlying physics is related to a spatial average over the configuration of the CDW, such as the polarization of the CDW. The global coupling proposed in the unified model [101] may be responsible for slaving the many degrees of freedom in the CDW to their spatial average.

Chapter 6

Unified Model of Switching and Non-Switching Charge-Density-Wave Dynamics

In this chapter I will argue that the dynamics of both switching and non-switching charge-density waves can be described by the classical Fukuyama-Lee-Rice model when the interactions with normal carriers are taken into account. We have constructed a circuit representation of the model and have performed numerical simulations in one dimension. We find switching in the limits of strong pinning or large normal-carrier resistance, consistent with experiment.

6.1 Introduction

The nonlinear dynamics of sliding charge-density waves (CDWs) has been studied extensively in the past fifteen years. Two classes of CDW behavior have been observed experimentally. Conventional, or “non-switching” behavior is characterized by a smooth, non-hysteretic I - V curve and a unique threshold field for sliding. Much of the non-switching behavior is well described by the Fukuyama-Lee-Rice (FLR) model [80], which treats the CDW phase as a classical field and ignores amplitude fluctuations of the CDW order parameter.

So-called “switching” behavior [57] is characterized by an abrupt, hysteretic transition into the sliding state. Switching was first observed in NbSe_3 , and subsequently in other ma-

terials such as TaS_3 , $(\text{NbSe}_4)_{3.33}\text{I}$, $\text{K}_{0.3}\text{MoO}_3$ and $\text{Rb}_{0.3}\text{MoO}_3$. It was observed later that switching could be induced in NbSe_3 by doping with iron, or by quenching [49], and that freshly-grown samples displayed switching while aged crystals did not. Based on these observations, switching in NbSe_3 has been associated with the presence of “ultrastrong” pinning centers. At lower temperatures, two threshold fields, the lower one non-switching and the upper one switching, have been observed in semiconducting materials such as $\text{K}_{0.3}\text{MoO}_3$, and also in NbSe_3 in the presence of a magnetic field [102]. The hysteresis increases as the temperature is lowered.

There have been a multitude of explanations for switching behavior [57]. Based on the importance of ultrastrong pinning centers, several models of switching have been proposed in which the dynamics of the CDW amplitude, ignored in the FLR model, are considered [67, 56]. The role of normal carriers is also ignored in most treatments of CDW dynamics. Tucker showed that normal carriers determine the time scale of dielectric relaxations of the pinned CDW [19]. P. B. Littlewood, elaborating on a two-fluid model of Sneddon [103], suggested that the inclusion of normal carriers could lead to two threshold fields and bistability of the CDW velocity, as observed in the semiconducting materials [19]. It was believed that the inclusion of normal carriers did not alter the form of the original FLR equations of motion, except to change the effective damping [104, 103].

In this chapter, we show that when the effects of normal carriers are properly incorporated into the FLR model, we obtain an additional new global coupling term. Non-switching behavior occurs in the limit of very weak pinning or small normal-carrier resistance. Switching occurs in the limits of strong pinning or large normal-carrier resistance. Both limits are consistent with experiment. We show how this model can be understood intuitively in terms of an electrical circuit. Numerical simulations in one dimension have been performed, consistent with our analytical results.

6.2 Derivation of the Model

In the one-dimensional FLR model, the charge density is written as

$$\rho(x) = \rho_c + \rho_0 \cos[Qx + \phi(x, t)], \quad Q = 2k_F, \quad (6.1)$$

where ρ_c is the condensate density, ρ_0 is the CDW amplitude (held fixed), $\phi(x, t)$ is the CDW phase, and k_F is the Fermi wavevector. The CDW current is given by

$$j_{\text{CDW}}(x, t) = -\frac{e}{\pi} \dot{\phi}(x, t). \quad (6.2)$$

Ignoring inertial effects, the FLR equation of motion is

$$\gamma_0 \dot{\phi} = K \nabla^2 - \rho_0 \sum_{i=1}^N V(x - x_i) \sin[Qx + \phi] - \frac{e}{\pi} E(x, t) \quad (6.3)$$

where γ_0 is the CDW damping constant, K is the CDW elasticity, $V(x - x_i)$ is the potential due to an impurity at site x_i , N is the number of impurities, and $E(x, t)$ is the local electric field. At finite temperature, normal carriers are excited across the Peierls gap, leading to a linear conductivity σ with an Arrhenius temperature-dependence. The total current in the presence of a spatially uniform external field (ignoring for simplicity displacement currents) is

$$\begin{aligned} j(x, t) &= j_{\text{CDW}}(x, t) + j_N(x, t) \\ &= -\frac{e}{\pi} \dot{\phi}(x, t) E(x, t), \end{aligned} \quad (6.4)$$

Incompressibility and current conservation ($\nabla \cdot \mathbf{j} = 0$) [105, 103] yield

$$j_{\text{CDW}}(x, t) + j_N(x, t) = \langle j_{\text{CDW}}(x, t) \rangle_x + \langle j_N(x, t) \rangle_x \quad (6.5)$$

where $\langle \rangle_x$ denotes a spatial average. Solving for $E(x, t)$, one obtains

$$E(x, t) = E_0 - \frac{e}{\pi\sigma} [\langle \dot{\phi}(x, t) \rangle_x - \dot{\phi}]. \quad (6.6)$$

The equations of motion can be written in a discretized form easily suited to numerical simulation by taking $V(r) = V_0\delta(x - x_i)$ and integrating out between impurities,

$$(\gamma_0 + \gamma_1)\dot{\phi}_i = K\nabla^2\phi_i + W \sin(\phi_i - \beta_i) + V + \gamma_1\langle \dot{\phi}_i \rangle_i \quad (6.7)$$

where ϕ_i represents the CDW phase at impurity site i , $\gamma_1 = e^2/\pi^2\sigma$ is the Ohmic damping constant, L is the average distance between impurities¹, $W \equiv -\rho_0 V_0/L$, $V \equiv -eE_0/\pi$, $\beta_i \equiv Qx_i$ is a random variable mod 2π , and $\langle \rangle_i$ denotes an average over impurity sites $i = 1, 2, \dots, N$.² We will henceforth work in units where $W = L = 1$. Viewed in the reference frame of the moving CDW [106, 19], the global coupling term $\gamma_1\langle \dot{\phi}_i(t) \rangle_i$ is by definition zero. But the CDW moving frame is not an inertial one, hence there will be a ‘‘fictitious’’ force $\gamma_1\langle \dot{\phi}_i(t) \rangle_i$. It is for this reason that we work in the inertial reference frame of the underlying lattice.

While the discretized version of Eq. 6.3 in the absence of normal carriers is often depicted in terms of balls and springs on a washboard, it also has a representation as an electrical circuit, as is shown in Fig. 6.1(a) for $N = 3$. The impurity potential seen by the CDW is represented by a nonlinear capacitor, which has the $Q - V$ relation $V = \sin(\phi_i - \beta_i)$, where ϕ_i represents the charge on the i th nonlinear capacitor. The domains are coupled by capacitors with capacitance $C = K^{-1}$, and are biased with a constant voltage V . The total CDW current is equal to the average of the currents through each nonlinear capacitor.

Fig. 6.1(a) demonstrates some of the unphysical aspects of the FLR model in the absence of normal carriers. Experimentally, one cannot specify the voltage across each single domain,

¹One need not approximate the impurity distance by its average. See Refs. [12, 11]

²Note that Eq. 6.7 follows directly from Eq. 6.6 when the condition $\nabla \cdot \mathbf{j} = 0$ is satisfied.

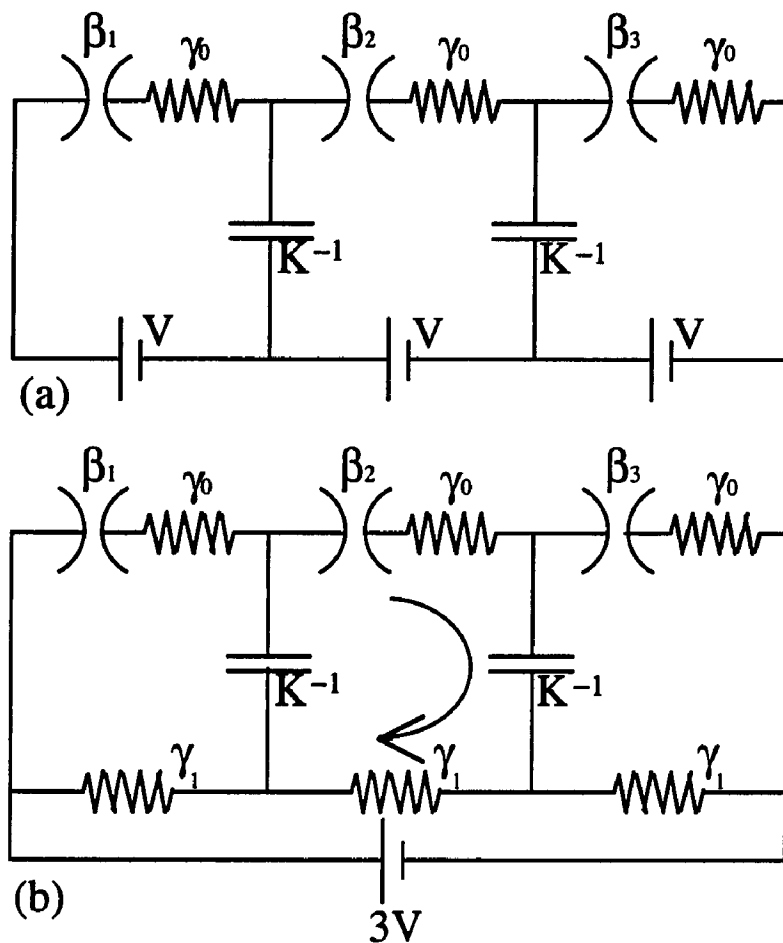


Figure 6.1: (a) Circuit representation of Fukuyama-Lee-Rice model (discretized version of Eq. 6.3) with $N = 3$ impurities (see text for discussion). The impurity potential seen by the CDW is modeled by a nonlinear capacitor with $V = \sin(\phi_i - \beta_i)$, where ϕ_i is the charge on the i th capacitor. The total CDW current is $(\dot{\phi}_i(t))_i$. (b) Circuit representation of Eq. 6.7. The voltage sources are replaced by resistors, and a voltage NV is applied across the ends of the circuit. Arrow indicates how a local CDW current is compensated by a backflow of normal electrons, thus conserving the total current. This circuit reduces to (a) in the limit $\gamma_1 \rightarrow 0$.

nor can one measure the current at each domain. Rather, one specifies the voltage across the entire sample, and measures the current, or vice-versa. Also, it is impossible to perform current-driven numerical simulations of the FLR model, making it difficult to compare with many experiments. Such difficulties are remedied by including normal carriers. Fig. 6.1(b) shows a circuit representation of Eq. 6.7. The voltage sources are replaced by resistors³ with resistance γ_1 , and the voltage across the ends of the network is NV (here, $N=3$). The arrow indicates how a local distortion of the CDW is compensated by a backflow of normal carriers. The circuit in Fig. 6.1(b) reduces to that of Fig. 6.1(a) if one lets γ_1 approach zero while holding V fixed (although the normal current becomes infinite).

6.3 Switching

One of the consequences of the additional term in Eq. 6.7 is switching behavior. The global nature of the coupling term $\gamma_i \langle \dot{\phi}_i(t) \rangle_i$ acts like an effective field which can “bootstrap” the CDW into a high-conduction state at a threshold field V_{i2} . The physical origin of the global coupling can be seen by imagining a situation where the CDW is pinned and V is close to V_{i2} . A local current flow, as indicated by the arrow in Fig. 6.1(b), will cause the voltage to drop across the center domain, thereby increasing the voltage across all the other domains. This situation is unstable for sufficiently large $\alpha \equiv \gamma_1/\gamma_0$, and can cause the CDW to switch to a high-conduction state. Once in the conducting state, the CDW can continue to slide until the voltage is lowered to $V_{i1} < V_{i2}$. We have performed numerical simulations of Eq. 6.7 for various values of α and K in a system with $N=50$ impurities. Figs. 6.2(a,b) plot the time-averaged CDW current \bar{J}_{CDW} versus V for various values of α and K . Fig. 6.2(a) shows that V_{i1} is independent α , while Fig. 6.2(b) shows that V_{i2} is insensitive to K , provided V_{i1} is sufficiently smaller than V_{i2} .

Fig. 6.3 shows how the size of the hysteresis loop $(V_{i2} - V_{i1})/V_{i1}$ varies with α and K . In the strong-pinning regime, the hysteresis is immeasurably small until $\alpha \sim 1$. In the weak-pinning regime, the crossover to significant hysteresis occurs at a larger value of α , and is a decreasing function of K for fixed α .

Much of the previous analysis of the FLR model carries over to Eq. 6.7, provided the system is in a particular pinned state. The reason is simple: in a stable pinned configuration, $\gamma_i \langle \dot{\phi}_i(t) \rangle_i = 0$, and hence, the location of the singular points in phase space will be independent of α . So, for example, the FLR arguments concerning the dependence on the upper threshold field V_{i2} on K for $\alpha=0$ remain valid for $\alpha > 0$. For $K \ll 1$ (strong pinning), the threshold field $V_{i2} \approx 1$, while for $K \gg 1$ (weak pinning), $V_{i2} \propto K^{4/(d-4)}$ in d dimensions [80]. Fig. 6.2(a) shows that V_{i2} is indeed independent of α ,⁴ and Fig. 6.2(b)

³One can model the effects of displacement currents by placing a capacitor in parallel with the normal resistor, and CDW inertia with an inductor in series with the CDW resistor.

⁴If the voltage is swept quickly, $\langle \dot{\phi}_j \rangle_j$ will not be zero, and hence V_{i2} will decrease. Such behavior is seen

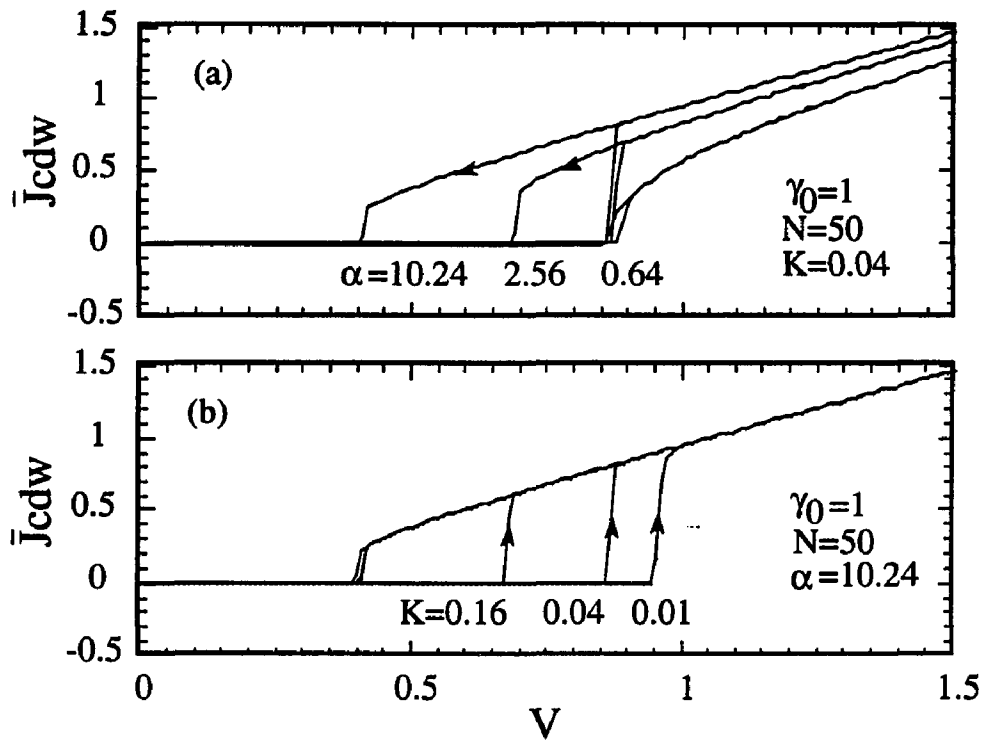


Figure 6.2: (a) Plot of time-averaged CDW current versus V for various values of α and $K = 0.16$ (see text for discussion). The upper threshold V_{t2} is independent of α . (b) Plot of I - V curves for various values of K and $\alpha = 10.24$. The lower threshold V_{t1} is independent of K for V_{t1} sufficiently smaller than V_{t2} .

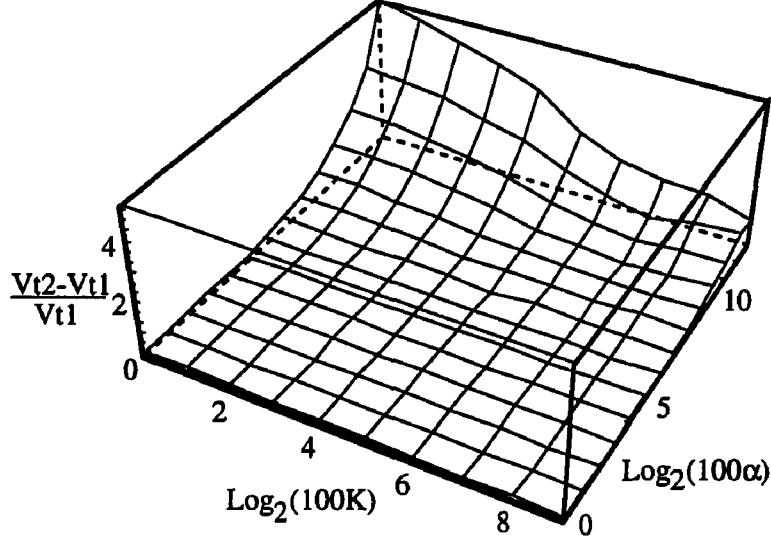


Figure 6.3: Plot of hysteresis as a function of α and K , with $N = 50$. Measurements were made at each grid intersection. Hysteresis for strong-pinning begins near $\alpha = 1$. For weak pinning, the onset of hysteresis occurs at a much larger value of α , and is smaller.

indicates that V_{i2} has the correct dependence on K , even for large α . Once in the sliding state, the picture changes dramatically. Estimating V_{i1} requires some manipulation of Eq. 6.7. One can re-express the global term by averaging both sides over the impurities i , obtaining

$$\gamma_0 \langle \dot{\phi}_i \rangle_i = \langle \sin(\phi_i - \beta_i) \rangle_i + V \quad (6.8)$$

and hence,

$$\gamma_0 \dot{\phi}_i = \frac{K \nabla^2 \phi_i + \sin(\phi_i - \beta_i) + \alpha \langle \sin(\phi_j - \beta_j) \rangle_j}{1 + \alpha} + V \quad (6.9)$$

Eq. 6.9 looks similar to Eq. 6.7, but now the global coupling term involves the spatial average of $\sin(\phi_j - \beta_j)$. The time- and space-averaged pinning force is related to the time-averaged CDW current \bar{J}_{CDW} by $\langle \sin(\phi_i - \beta_i) \rangle_{i,t} = \gamma_0 \bar{J}_{\text{CDW}} - V$. In the pinned state, $\langle \sin(\phi_j - \beta_j) \rangle_{j,t} \approx -V$, and $\langle \dot{\phi}_i \rangle_i \approx 0$. In the high-field limit, $\langle \sin(\phi_j - \beta_j) \rangle_{j,t} \approx 0$ and $\langle \dot{\phi}_i \rangle_i \approx V$. The high-field limit occurs at smaller V for larger α , as can be seen from Fig. 6.2(a). The pinning potential is scaled by $(1 + \alpha)$, so that $V_{i1} \propto (1 + \alpha)^{-1}$ for $\alpha \gg 1$. In the limit $K \rightarrow \infty$, one can view Eq. 6.8 as an equation of motion for $\Phi(t) \equiv \langle \phi_i(t) \rangle_i = \phi_j(t)$, for all j . In the limit $\alpha \rightarrow \infty$, one also obtains Eq. 6.8 for $\Phi(t) = \phi_j(t) + c_j$, where c_j are

numerically, and has in fact been observed experimentally. See Ref. [107].

“frozen”. Thus, at low temperatures, the CDW behaves as a rigid object. [19] Switching behavior is the rule rather than the exception for the semiconducting CDW materials.

As $T \rightarrow 0$, γ_0 , dissipation arising from phason-phason and phason-phonon scattering [108], tends to zero, while γ_1 becomes exponentially large [103]. In terms of the circuit representation, this amounts to removing the bottom resistors and shorting the top ones, leading to a rigid CDW whose differential resistance becomes zero at threshold. Such behavior has in fact been observed in $K_{0.3}MoO_3$ and other semiconducting materials [109]. We believe that our model also accounts for switching behavior in $NbSe_3$, although the situation is complicated by the presence of a chain in the unit cell which remains metallic at low temperatures. The increase of the hysteresis loop width $V_{i2} - V_{i1}$ as temperature is lowered is consistent with increasing α at fixed K in our model. This is in apparent conflict with the fact that the normal resistance of $NbSe_3$ decreases as temperature is lowered. The conflict suggests that the CDW is screened more effectively by quasiparticles on the CDW chain than by normal electrons on a neighboring chain, and that γ_1 cannot be simply assigned to the normal resistance in $NbSe_3$. We believe that the velocity discontinuities, or phase-slip centers, observed in switching samples of $NbSe_3$ are indicators of strong pinning centers but are not responsible for switching.

Another consequence of the global coupling term in Eq. 6.7 is the non-uniqueness of the sliding state. It has been shown that the FLR model obeys a so-called “no-crossing condition” [110], which requires the sliding state to be unique and the transition to the sliding state to be non-hysteretic. It is simple to show by construction that the global coupling term violates this no-crossing condition, hence allowing multiple sliding states for a fixed voltage V . Such multiple sliding states are observed numerically for large N , and N as small as 3. Fig. 6.4 shows the total current $J(t)$ versus time for two distinct sliding states corresponding to $V = 1.0$ in a system with $N = 3$. The magnitude of the current oscillations (narrow-band noise) are larger for the solid curve, but the time-averaged current is smaller. The effect of added noise might cause hopping between metastable running states, yielding long-term fluctuations of the narrow-band noise frequency, first noticed as such by Bhattacharya *et al.* [37].

The generalization of Eq. 6.7 to higher dimensions may yield two threshold fields, as observed experimentally. Also, observed differences between current- and voltage-driven experiments in switching samples may be borne out by analogous numerical “experiments”. Other phenomena associated with switching [57], such as period-doubling, negative differential resistance, and delayed switching, should be explored within the context of this model. Preliminary numerical experiments show that Eq. 6.7 exhibits period doubling, as well as delayed switching⁵. The global coupling term in Eq. 6.7 will very likely have a profound effect on the critical dynamics near threshold [35], even in parameter regimes where switching

⁵See Ch. 7

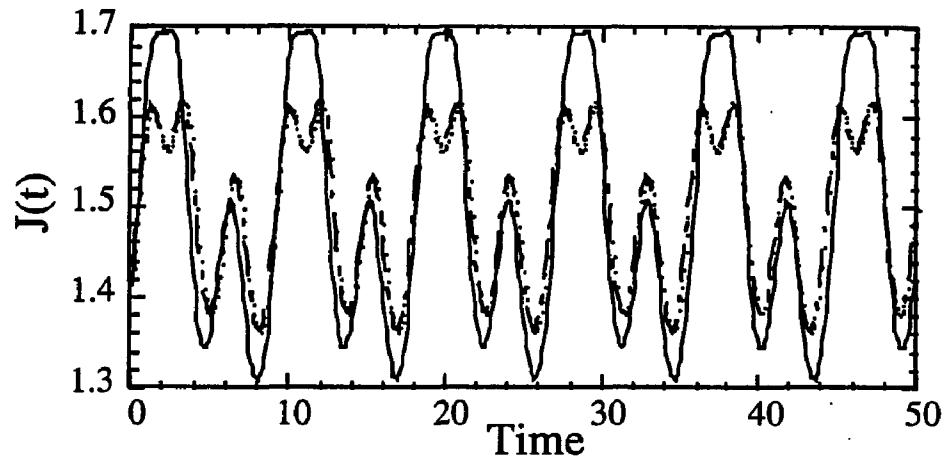


Figure 6.4: Steady-state total current $J(t)$ versus time for two different initial configurations and identical parameters $N = 3$, $K = 0.01$, $\gamma_0 = 1$, and $\alpha = 1.28$. The total current $\bar{J} = 1.490$ for the solid curve, and $\bar{J} = 1.497$ for the dash-dotted curve.

does not occur. This global coupling is present in many other nonlinear dynamical systems with many degrees of freedom, such as Josephson junction arrays [111, 112] and coupled laser systems [113], and its nonlinear dynamics should prove to be fascinating.

Chapter 7

Impulse Response of the Switching Charge-Density-Wave Conductor NbSe₃: A Novel Delayed Transition

When a switching CDW conductor is driven with a rectangular voltage pulse, the CDW begins to slide only after a delay τ . We present detailed measurements of the impulse response of the charge-density-wave (CDW) conductor NbSe₃ as a function of the pulse height, temperature, and initial configuration. We find that the average conduction delay $\bar{\tau}$ has an activated temperature dependence for pulse heights sufficiently far above threshold: $\bar{\tau} \propto \exp(E_a/k_B T)$, where $E_a = 24.0 \pm 3.8$ meV, comparable to the CDW gap. We have also performed numerical experiments based on a model which includes the interaction of the CDW with uncondensed electrons. Within this model, we can account for the polarization-dependence of the threshold for sliding, and the dependence of the conduction delay on the pulse height. If we assume that the ungapped carriers in NbSe₃ do not screen the motion of the CDW, then the Arrhenius temperature-dependence of the delayed conduction can also be explained. The excellent qualitative agreement between theory and experiment provides a compelling argument that switching behavior arises from the interaction of the CDW with uncondensed carriers.

7.1 Introduction

Charge-density-wave (CDW) conductors display a remarkable diversity of nonlinear phenomena [114]. The source of the nonlinearity arises from the interaction of the CDW, commonly treated as an elastically deformable medium [80], with randomly spaced impurities. The incommensurate CDW is pinned by these impurities, but slides and carries current when an applied electric field exceeds a threshold E_T . At temperatures near the Peierls transition temperature T_P , the threshold is unique and non-hysteretic. At lower temperatures, the interaction of the CDW with thermally excited quasiparticles becomes as important as the interaction with impurities in the semiconducting CDW materials such as $\text{K}_{0.3}\text{MoO}_3$ and o-TaS_3 . Experimental evidence for this includes the observation that the CDW conductivity above threshold becomes proportional to the number of normal carriers [17], and the presence of a broad overdamped mode (associated with internal modes of the CDW) which freezes out at low temperatures [115]. At still lower temperatures a second, hysteretic threshold E_T^* develops, above which the CDW slides almost without damping [116, 117, 18, 109].

It has been known for some time that normal carrier screening increases the effective CDW damping [103], but it was Littlewood who suggested that this interaction might explain the existence of two threshold fields and the hysteretic behavior in the semiconducting materials [19]. Much of the behavior observed in the semiconducting compounds are also seen in NbSe_3 , which remains metallic at low temperatures. So-called “switching” behavior, in which the CDW depins suddenly and hysteretically, is observed in some, but not all, samples of NbSe_3 [57]. Several attempts have been made to understand switching behavior in NbSe_3 in terms of phase slip [56], CDW inertia [47], and other processes [57]. We have proposed a model [101] similar to Littlewood’s, in which the uncondensed carriers are shown to produce a global coupling term into the equations of motion for the CDW, giving rise to hysteresis in one dimension, and two threshold fields in two dimensions [118].

Charge-density-wave dynamics in the switching regime differs markedly from the non-switching regime; included are the observation of negative differential resistance and related instabilities [52], anomalously large broadband noise [52], and period-doubling and chaotic behavior in the presence of combined dc and ac fields [48, 93]. A particularly unique and puzzling phenomenon was observed by Zettl and Grüner, who found that if one applies a voltage (or current) pulse above threshold, the CDW will begin to slide only after a delay τ [53]. Delayed conduction has also been observed in o-TaS_3 [55]. In a previous paper [91], we observed that the distribution of switching delays displayed a sensitive dependence on the initial configuration, and that the delay could vary over five orders of magnitude for nominally identical experimental conditions.

The phenomenon of delayed conduction provides a stringent test for competing models of switching CDW transport. Here we present the main results of a detailed experimental and numerical study of the phenomena of conduction delays in CDWs. In section 7.3, we

describe experiments which have investigated the phenomenon of conduction delays as a function of temperature, pulse height, and initial configuration. Our main results are as follows: Near the threshold for sliding, we observe a broad distribution of “long” delays τ , whose standard deviation exceeds the average, and whose average $\bar{\tau}$ depends quite strongly on the pulse height. As the pulse height is increased there is a distinct crossover to “short” delays, in which the standard deviation is below the average. The short delays decrease approximately exponentially with pulse height. The delay at the crossover between long and short delays (or the delay for a fixed fraction above threshold) displays an Arrhenius temperature dependence with an activation energy E_a comparable to previous measurements of the CDW gap. The switching time t_{sw} (defined as the time taken for the CDW current to rise from 10% to 90% of its asymptotic value) displays a similar temperature dependence. We have also performed experiments in which the initial configuration was prepared in specific ways. The first method involved heating the CDW crystal above the Peierls transition and allowed it to cool in zero field. The second method involved applying a negative pulse to the CDW. In both cases, we observed a lower threshold for sliding when a positive pulse was applied starting from the relaxed configuration.

In Sec. 7.4, we describe numerical “experiments” on delayed conduction. The model we simulate is a variant of the model of switching and non-switching CDW transport discussed in Ref. [101]. In this variant, both the interaction between the CDW and normal carriers and the non-uniform spatial distribution of impurities are taken into account. We observe delayed conduction, and explain its origin in the model, as well as the dependence of the threshold field on the initial configuration, the temperature dependence of the conduction delay τ and the switching time t_{sw} . We also observe good qualitative agreement between the dependence of the delay time τ with pulse height. The agreement between experiment and theory provides strong support for the model, as well as a compelling argument that ungapped carriers in NbSe₃ play a negligible role in screening CDW deformations.

7.2 Experimental Methods

The experiments were performed on three samples of NbSe₃ at temperatures $18 \text{ K} < T < 33 \text{ K}$. All three samples displayed a single, clean switch. In this paper, we will present mostly the results for a single sample, but will summarize the results for the other samples where appropriate.

The samples were grown by conventional vapor transport methods. Switching samples of NbSe₃ generally are obtained in freshly-grown batches, but we have found that cooling the samples in liquid nitrogen and/or storing them in vacuum greatly prolongs the life of a switching batch. The samples were placed inside of a conflat flange filled with 1 atm. of Helium gas, in order to minimize ohmic heating of the sample, and cooled using a closed-

cycle helium refrigerator. The samples were mounted in a two-probe configuration on a ceramic 50 Ohm microstripline terminated by 50 Ohm resistors at each end. The conflat flange can hold up to six samples at a time, which was important because the success rate in finding high-quality samples is quite low. Temperature stability was somewhat problematic, because of the uneven cooling power of the refrigerator, but this difficulty was overcome by using two pairs of temperature sensors and heaters, one near the coldhead, and one inside the conflat flange. With this method we were able to achieve a temperature stability of ± 10 mK over an indefinite range of time. The samples were driven by a pulse generator with a rise time of 5 ns.

7.3 Experimental Results

At temperatures near the Peierls temperature $T_{P2}=59$ K, the CDW depins smoothly at a threshold E_t . As the temperature is lowered, the CDW conductivity near E_t decreases, and a second threshold develops at a higher field E_t^* . This threshold becomes hysteretic, and the width of the hysteresis loop increases, as the temperature is lowered further. Fig. 7.1 shows the current as a function of applied voltage for sample #1, at temperatures ranging from 28.2 K down to 18.8 K. Due to the low impedance of the sample (32 Ohms at T=20 K), the voltage across the sample differs in the sliding and pinned state. The width of the hysteresis loop increases as the temperature is lowered. The ohmic resistance of the sample decreases with temperature in this range, whereas the sliding state conductivity is approximately independent of temperature.

In the first set of experiments, a one-second voltage pulse V_p was applied to the sample, followed by a two-second interval with zero voltage, as depicted in Fig. 7.2. The CDW current was digitized over the range 0.1 μ sec–1 sec, and the delay τ was determined by a computer algorithm. The switching time t_{sw} was also measured from the resulting current trace. Typically, 1024 delays were measured for a given V_p and temperature.

7.3.1 Distribution of Delays

Figs. 7.3(a–d) shows a histogram of the conduction delays for various temperatures T and pulse heights V_p . The various histograms are offset for clarity. We define as threshold V_{th} the pulse height for which half of the pulses do not result in CDW conduction. Our main results do not depend critically on this choice for V_{th} . For T=19.8 K, $V_p^{th}=14.96$ mV, as seen in the top trace of Fig. 7.3(a). As V_p is increased, the distribution remains broad, but begins to narrow relative to its average near $V_p=15.31$ mV. Above this pulse height, the distribution remains narrower, and the average decreases much less rapidly. Similar behavior is observed in Figs. 7.3(b–d).

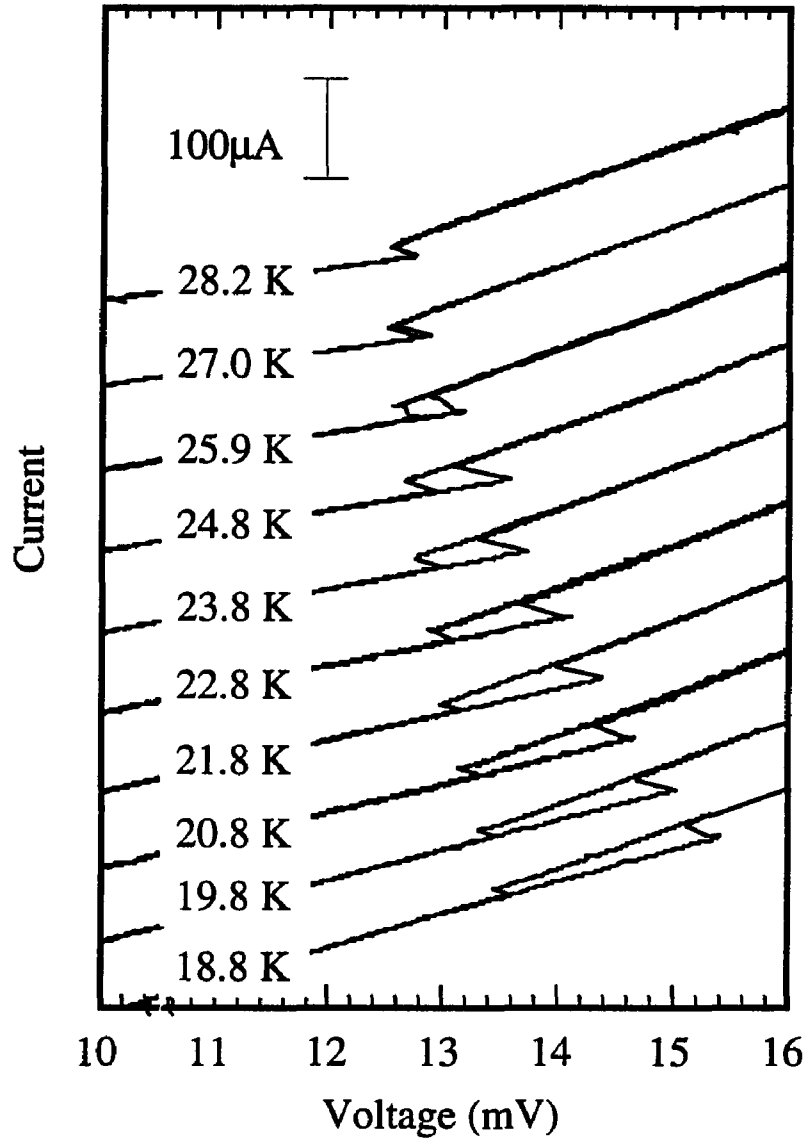


Figure 7.1: I - V curves at various temperatures for sample No. 1 (length = 0.4 mm; ohmic resistance = 32 Ohms at $T=20$ K). The onset of hysteresis occurs near 28 K, although the I - V curve is double-valued at higher temperatures due to the finite impedance of the voltage source. The transitions to and from the sliding states are not vertical, due to the 50 Ohm impedance of the voltage source and the 50 Ohm terminating resistors. As the temperature is lowered, the ohmic (low field) resistance decreases, and the hysteresis increases.

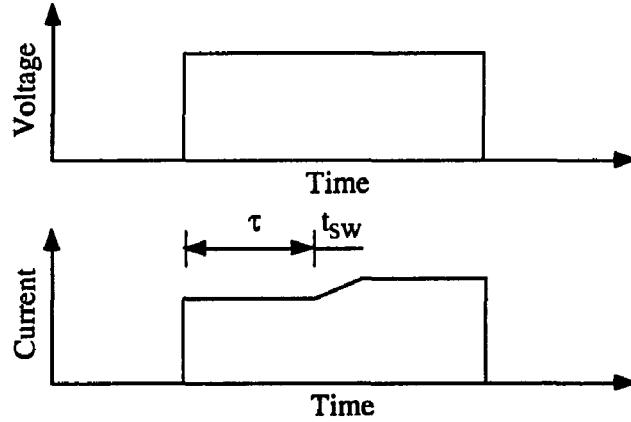


Figure 7.2: Schematic representation of the impulse response experiments. The sample is driven by a one-second voltage pulse of height V_p , followed by a two-second wait period. The CDW current is then digitized, and the conduction delay τ and switching time t_{sw} are determined from the current trace. The experiment is repeated 1024 times for various values of V_p and at different temperatures.

The crossover from a fairly broad distribution to a much more narrow one can be seen more clearly if one looks at the average delay $\bar{\tau}$ and standard deviation σ as a function of V_p . Figs. 7.4(a-c) show the average delay and standard deviation versus the reduced pulse height $\epsilon \equiv (V_p - V_p^{th})/V_p^{th}$ for the three samples which were studied. For values of ϵ below a sample- and temperature-dependent crossover value ϵ_{co} , the distribution of “long” delays is quite broad, and the average delay $\bar{\tau}$ depends sensitively on ϵ . Associated with ϵ_{co} is a fairly distinct crossover at time τ_{co} to “short” delays, in which $\bar{\tau}$ depends much more weakly on V_p , and for which the standard deviation σ is much smaller than $\bar{\tau}$. This crossover time is more pronounced in samples #2 and #3 than in sample #1. The dependence of the short delays on ϵ can be fit fairly well to a power law $\bar{\tau} \propto \epsilon^{-\delta}$ with $\delta \approx 2$ for sample #1, but samples #2 and #3 clearly appear to fit an exponential form much better.

7.3.2 Temperature Dependence of Delays

The conduction delays display a very strong dependence on temperature. By changing the temperature over a few degrees, the average delay can change by several orders of magnitude. Figs. 7.5(a-c) show the average delay $\bar{\tau}$ versus reduced pulse height ϵ at various temperatures for samples #1-3, respectively. As the temperature is increased, the average delay decreases. The temperature dependence of ϵ_{co} is very much sample-dependent, remaining essentially constant for sample #1, decreasing with temperature for sample #2,

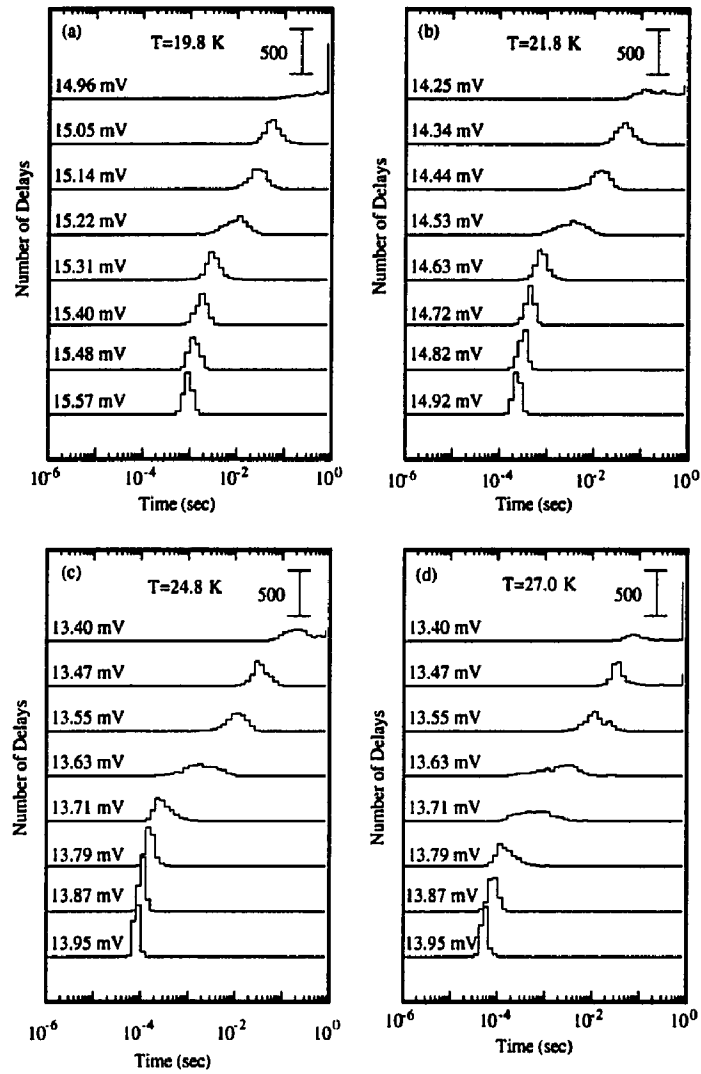


Figure 7.3: Distribution of delays as a function of V_p and temperature. For V_p close to the threshold for sliding, the distribution of delays is broad. As V_p increases, there is a crossover to a much narrower distribution. (a) $T=19.8$ K. (b) $T=21.8$ K. (c) $T=24.8$ K. (d) $T=27.0$ K.

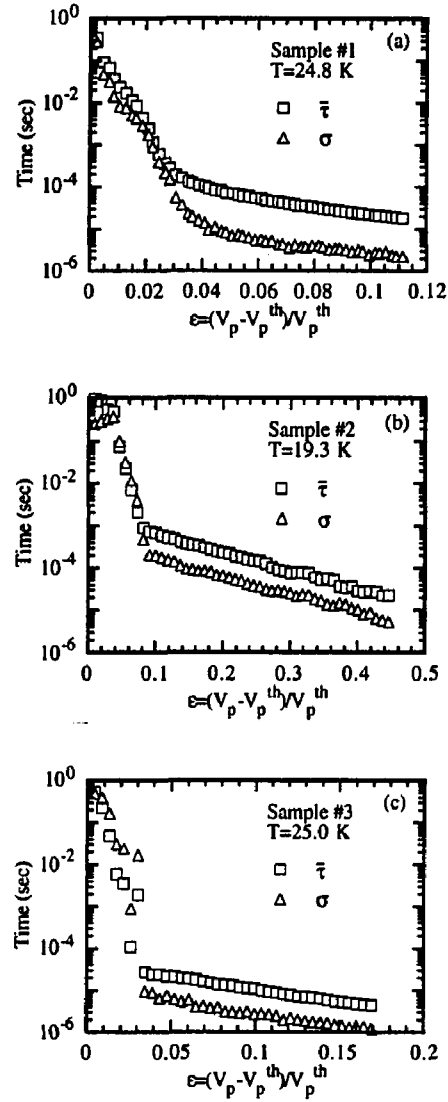


Figure 7.4: Plot of average switching delay $\bar{\tau}$ (\square) and standard deviation σ (Δ), for samples #1–3, respectively. Near threshold, the delays are “long”: $\bar{\tau}$ depends strongly on the reduced pulse height ϵ , and the standard deviation σ on the order of $\bar{\tau}$. At larger ϵ , the delays become “short”: the standard deviation falls below the average, and the dependence of τ on V_p is much weaker. There is a fairly well-defined crossover time τ_{co} which separates the two regimes. (a) Sample #1. (b) Sample #2. (c) Sample #3.

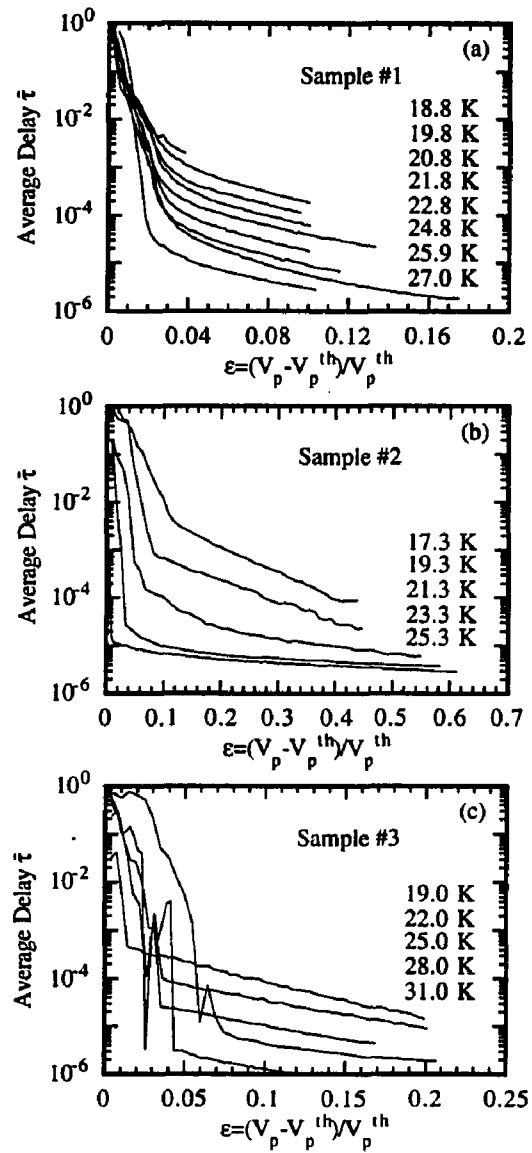


Figure 7.5: Average switching delay $\bar{\tau}$ versus ϵ for different temperatures. The delays decrease monotonically as the temperature is increased. (a) Sample #1. (b) Sample #2. (c) Sample #3.

and apparently increasing for sample #3. These sample-to-sample variations may have to do with the fact that the distribution of delays is bimodal in many samples [91]; the presence of only a small fraction of “long delays” may overwhelm an otherwise smaller average, as is the case for Fig. 7.5(c) at $T=31.0$ K. The exponential dependences of $\bar{\tau}$ on ϵ seen in samples #2 and #3 are more robust at lower temperatures, becoming less dependent on ϵ as $\bar{\tau}$ approaches a critically small value (3 μ sec for sample #2).

The switching time t_{sw} displays a similar dependence on temperature. Fig. 7.6 shows typical short switches for sample #1 at four different temperatures, for values of ϵ slightly above ϵ_{co} . As the temperature is increased from 19.8 K to 27.0 K, τ decreases by more than two orders of magnitude. The switching time t_{sw} decreases in a similar fashion. The switching time t_{sw} , while highly dependent on temperature, displays no observable dependence on ϵ .

The temperature dependence of both $\bar{\tau}_{co}$ and t_{sw} are shown in Figs. 7.7(a–b). Fig. 7.7(a) shows an Arrhenius plot of τ_{co} versus inverse temperature for three different samples. The data are clearly fit well by straight lines, with a mean activation energy $E_a = 24.1 \pm 3.2$ meV. The switching time t_{sw} also appears to behave in an activated fashion (with mean activation energy $E_a = 24.0 \pm 3.8$ meV), as shown in Fig. 7.7(b). The activation energy is comparable (i.e., within factors of two) to more direct measurements of the CDW gap, [119, 120, 121] as well as measurements of the activated behavior of the CDW current in $NbSe_3$ below E_T^* by Adelman et al. [122].

7.3.3 “Melting” the CDW

We have also performed experiments in which we prepared the initial configuration of the CDW in various ways. One method that we have used previously [91] involves applying a sinusoidal signal to the CDW of the form $V(t) = V_0(\frac{1}{2})(1 - \cos \Omega t) \cos(2\pi f t)$, where $2\pi/\Omega = 3$ sec and f ranged from 100 Hz to 100 kHz. The disadvantage of this method of preparing the initial configuration is that one has little intuition of what the final configuration of the sample might be, and there is no guarantee that the configuration will be the same for every pulse. A conceptually simpler method of preparing the initial configuration is the following: first, the sample is heated above the Peierls temperature, in effect “melting” the CDW. Next, the sample is allowed to cool slowly at zero electric field, to a final temperature. The CDW should then be in a highly reproducible configuration, and one can investigate the impulse response beginning from this configuration. Several one-second pulses are then applied as in the earlier experiments.

Fig. 7.8 shows the time evolution of the current for two successive pulses (pulse 1 and pulse 2) at various values of V_p and $T=20$ K for sample #1. The initial configuration of the CDW was prepared as described above. The traces for different values of V_p are offset for clarity, but there is no offset between pulse 1 (squares) and pulse 2 (circles). The top

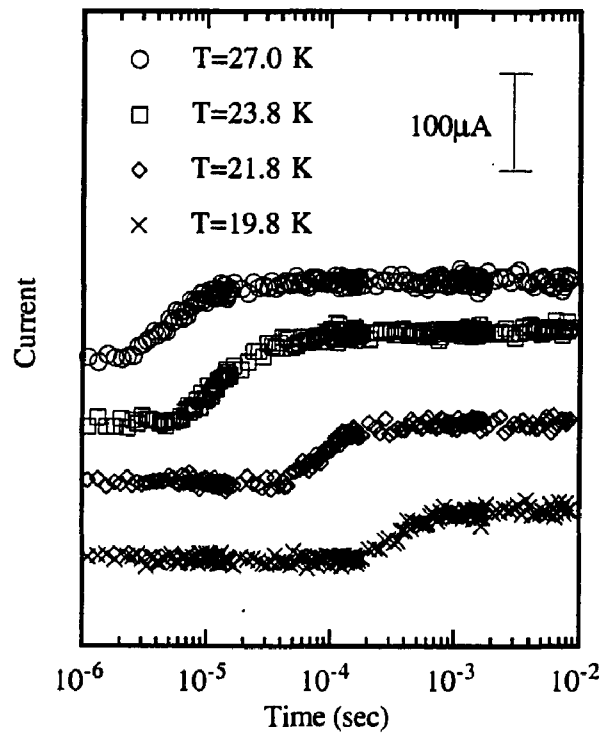


Figure 7.6: Experimentally measured CDW current versus time for a typical “short” delay at four different temperatures. The four traces are offset vertically for clarity. Note that the time scale for both τ and t_{sw} scale together (i.e., the curves look similar but shifted on a logarithmic scale).

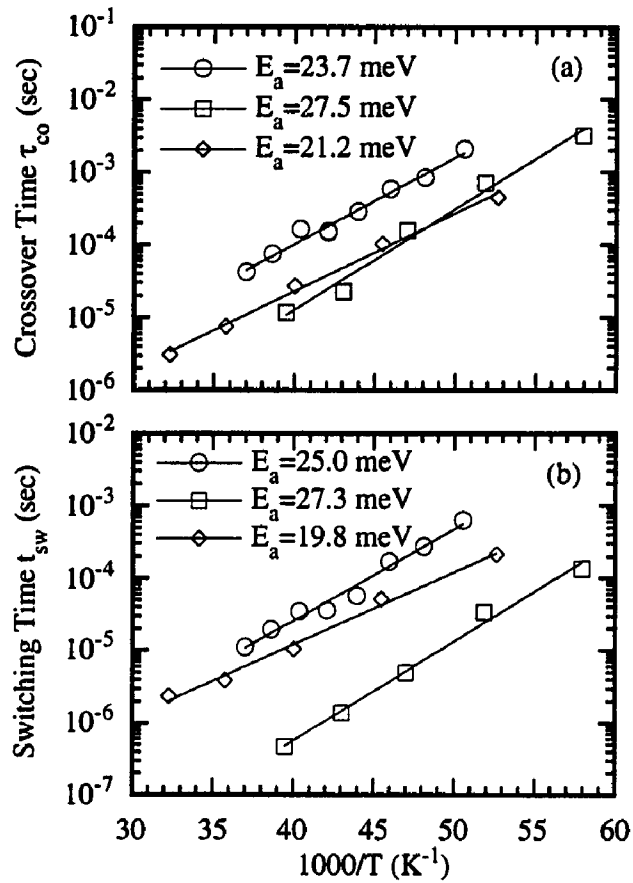


Figure 7.7: (a) Plot of crossover time τ_{co} versus inverse temperature for three different samples of NbSe₃. The solid lines represent fits to the form $\tau_{co} \propto \exp(E_a/k_B T)$. (b) Plot of switching time t_{sw} for the same samples as in (a). Solid lines are fits to the same functional form as in (a).

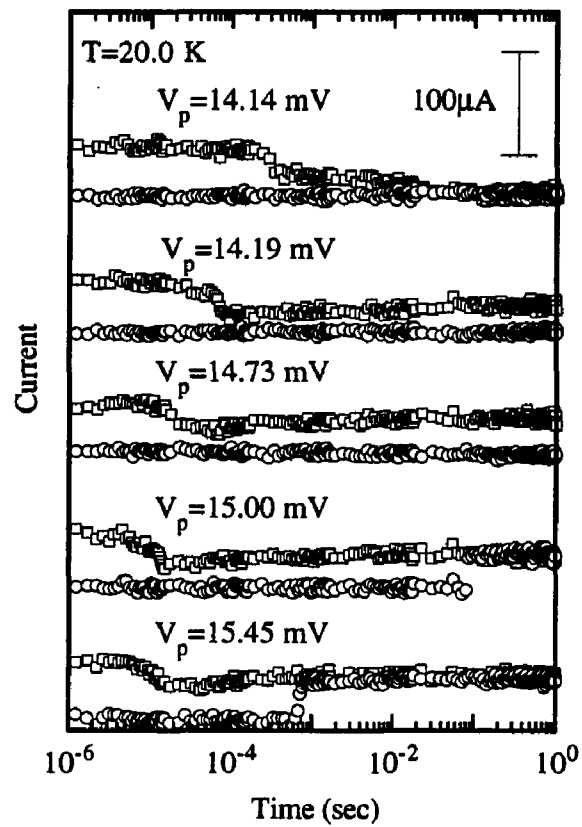


Figure 7.8: Current versus time for various values of V_p , for two different initial conditions. Pulse 1 (\square) is the response after heating the sample to 70 K and cooling down to 20 K over a period of 600 sec. Pulse 2 (\circ) started 3 s after the end of pulse 1. The current traces for different V_p are shifted for sake of clarity. See text for a detailed description.

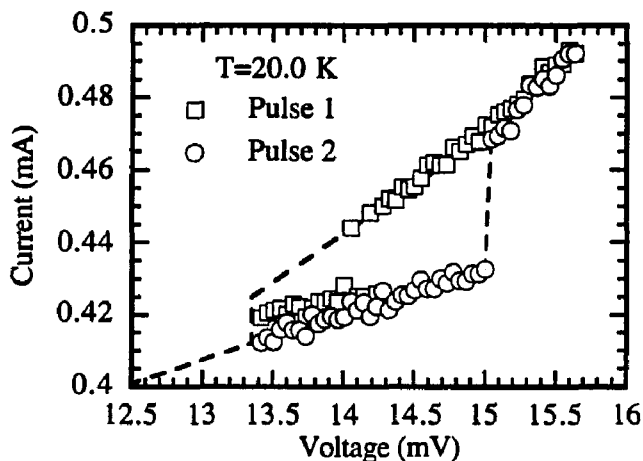


Figure 7.9: Final current versus pulse height V_p for two successive pulses (1 and 2) after heating the sample above the Peierls temperature ($T \approx 70$ K) and allowing it to cool to $T=20$ K at zero field. The dashed line represents the I - V curve for slow ramping. The threshold for switching is significantly lower for the first pulse.

two traces show the current versus time for $V_p=14.14$ mV. At the end of both pulses the CDW remained in the pinned state. For pulse 1, there is a large polarization current, which appears to decay abruptly near $30 \mu\text{s}$, and disappear completely by 10 ms. This polarization current is not observed for pulse 2. At $V_p=14.19$ mV, one sees a similar polarization current for pulse 1, and the CDW remains in the sliding state. After approximately $100 \mu\text{s}$, even though there is no clear switch, the current has reached an approximately steady state with the CDW sliding. The second pulse shows no polarization current, and remains in the pinned state. Similar behavior is also observed at $V_p=14.73$ mV, although the time at which the polarization current decreases has decreased. At $V_p=15.00$ mV, one observes delayed conduction in pulse 2 at 100 ms. The conduction delay shortens as V_p is increased to 15.45 mV, consistent with earlier experiments. The response to pulse 2 and successive pulses is qualitatively indistinguishable from the response of the CDW when its initial condition was not specially prepared.

The initial configuration of the CDW appears to have a profound effect on the pulse-driven threshold for sliding. Fig. 7.9 shows a plot of the total current through the sample at the end of the first and second pulses versus V_p . The dashed line indicates the hysteresis loop obtained from a slowly ramped I - V trace. For pulse 1, the CDW slides when V_p is

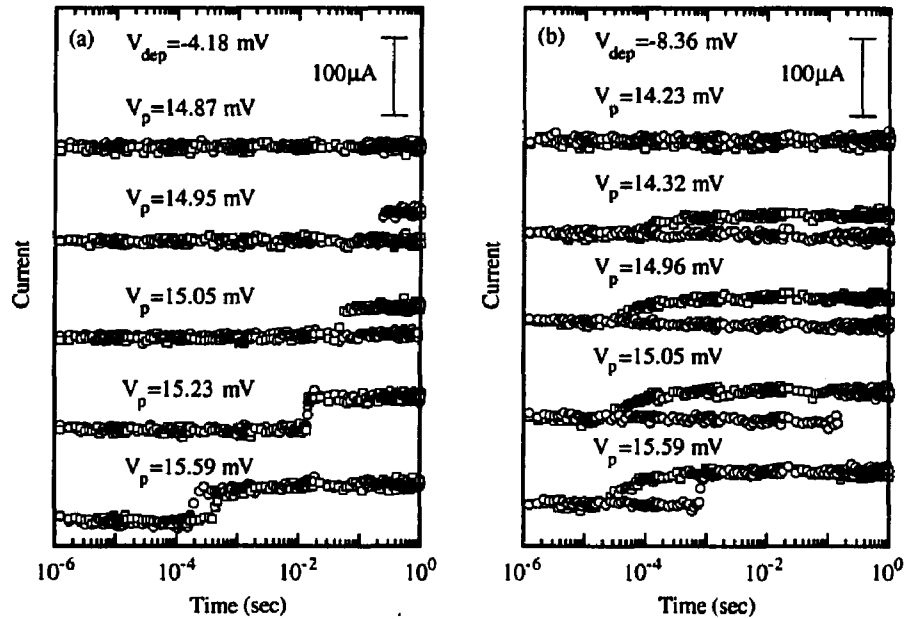


Figure 7.10: (a) Current versus time for two successive pulses (1 (\square) and 2 (\circ)) at various values of V_p , after a 1 s depolarizing pulse of strength V_{dep} . (a) $V_{dep} = -4.18$ mV. (b) $V_{dep} = -8.36$ mV.

near the middle of the hysteresis loop, while for pulse 2 and successive pulses, the CDW slides only if V_p exceeds the threshold obtained from the slowly-ramped I - V curve.

The polarization currents described above, as well as the polarization dependence on the threshold for sliding, were reproduced in sample #2, and were not checked for sample #3.

7.3.4 “Depolarizing” the CDW

A similar experiment was performed in which the CDW was prepared by a one-second pulse of strength V_{dep} , followed by two seconds at zero bias. Several one-second pulses were then applied as in the earlier experiments. Figs. 7.10(a-b) show current traces for two values of V_{dep} . As in Fig. 7.8, the traces for different values of V_p are offset for clarity, but there is no

offset between pulse 1 (squares) and pulse 2 (circles). In Fig. 7.10(a) $V_{\text{dep}} = -4.18$ mV. At $V_p = 14.87$ mV, there are no measurable polarization currents for pulse 1, in contrast to the behavior for Fig. 7.10. As V_p is increased, we observe no statistically significant difference between pulse 1 and pulse 2. At $V_p = 14.95$ mV, switching occurs for pulse 1, but not for pulse 2, while at $V_p = 15.05$ mV, the situation is reversed. At $V_p = 15.23$ mV, both pulse 1 and pulse 2 produce a switch at almost exactly the same time.

The situation is different when the magnitude of V_{dep} is increased to -8.36 mV, as shown in Fig. 7.10(b). The current traces are essentially the same for both pulse 1 and pulse 2 at $V_p = 14.23$ mV. At $V_p = 14.32$ mV switching occurs for pulse 1, but not for pulse 2. At $V_p = 15.05$ mV both pulse 1 and pulse 2 produce switching, although one can see that the delay is much longer for pulse 2. The switching time t_{sw} is approximately the same for both pulses.

Figs. 7.11(a–b) show plots of the total current through the sample at the end of the first and second pulses versus V_p for the two values of V_{dep} corresponding to Figs. 7.10(a–b), respectively. The dashed line indicates the hysteresis loop obtained from a slowly ramped I - V trace. In Fig. 7.11(a), there is no appreciable difference between pulse 1 and pulse 2, while Fig. 7.11(b) clearly shows that the threshold for switching is somewhere near the middle of the hysteresis loop for pulse 1, and near the threshold for the slowly ramped I - V curve for pulse 2 and successive pulses. Behavior similar to Fig. 7.11(b) was observed for higher values of V_{dep} , with no appreciable change in the threshold for pulse 1. For pulse 1, the CDW slides when V_p is near the middle of the hysteresis loop, while for pulse 2 and successive pulses, the CDW slides only if V_p exceeds the threshold obtained from the slowly-ramped I - V curve.

7.4 Numerical Results

7.4.1 Previous Work

Several theories have been proposed to explain CDW conduction in switching samples. Hall *et al.* [51] have proposed that switching samples contain a few “ultrastrong pinning centers” [66] which prevent the intact CDW from sliding. The CDW can slide only when the internal strains become sufficiently large to cause tears, or phase slips, in the fabric of the condensate. Inui *et al.* [56] proposed a many-body Hamiltonian embodying these ideas, and they numerically investigated a 1-degree-of-freedom version. Strogatz *et al.* [67] have proposed a different, exactly-soluble many-body Hamiltonian that is isomorphic to the mean-field x-y model. Each of these models shows delayed switching [65], and there has not been much experimental work that could distinguish between them. Other mechanisms

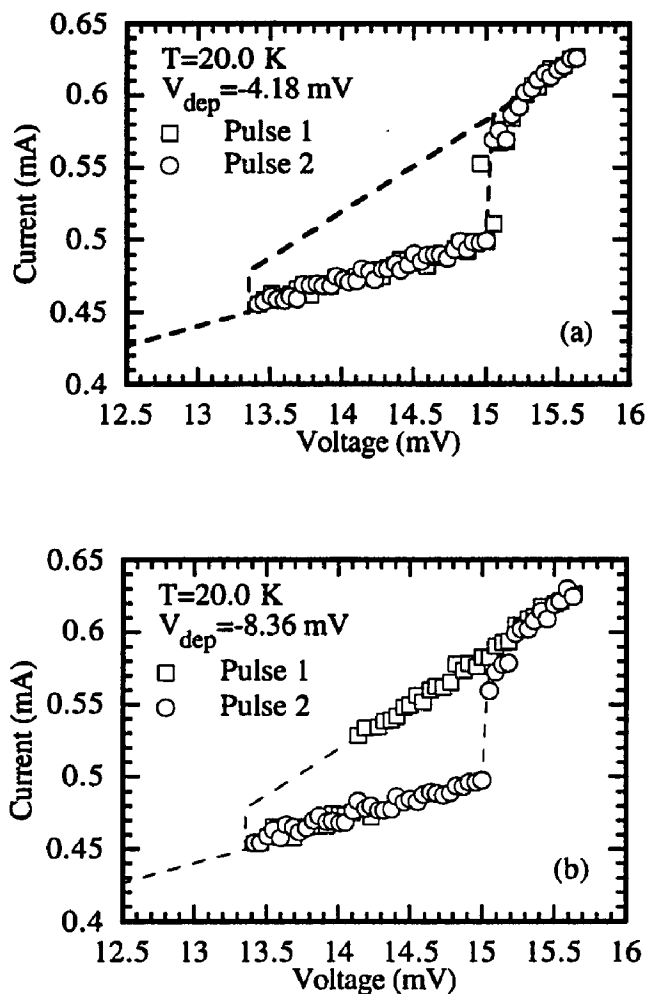


Figure 7.11: Final current versus pulse height V_p for pulse 1 and pulse 2 for depolarizing experiment (see Fig.7.10). Dashed line shows hysteretic I - V curve for slowly swept voltage. The voltage shown assumes that the response of the sample is ohmic (c.f. Fig. 7.1). (a) $V_{\text{dep}} = -4.18$ mV. There is little difference between pulse 1 and pulse 2. (b) $V_{\text{dep}} = -8.36$ mV. Pulse 1 ends up in the sliding state for $V_p > 14.2$ mV, whereas the threshold is $V_p > 15.0$ mV for pulse 2.

have also been proposed to explain delayed conduction specifically [53, 64, 123, 124]. In this section, we discuss a variant of the model described in Ref. [101], in which the distribution of impurities has been taken into account. We then present numerical simulations and compare our results with experiment.

7.4.2 Equations of Motion

We first discuss the origin of the equations of motion that we use for our simulations. We have found that it is crucial to employ a nonuniform (Poisson) distribution of impurity spacings, because it is this distribution which gives rise to polarization-dependent effects such as the pulse-sign memory effect [12]. Our method of discretization differs slightly (but significantly) from previous methods [11, 12]. We start as usual with the Fukuyama-Lee-Rice energy functional:

$$U = \int dx \frac{K}{2} \left[\frac{\partial \phi}{\partial x} \right]^2 - \phi E(x) + \sum_j \rho(x) V(x - x_j), \quad (7.1)$$

where $\phi(x)$ is the CDW phase as position x , K is the CDW elasticity, $E(x)$ is the (local) electric field, $\rho(x)V(x) \approx -\cos(Qx + \phi(x))\delta(x)$ is the impurity energy associated with impurity site x_j , and Q is the CDW wavevector. We then make the *ansatz* that the system is overdamped, with a damping constant γ_0 . The overdamped equation of motion arises from the equation

$$\gamma_0 \dot{\phi}(x) = -\frac{\delta U}{\delta \phi(x)}. \quad (7.2)$$

We then integrate Eq. 7.2 between impurity sites, making the following *approximations*:

$$\int_{s_j}^{s_{j+1}} dx \phi(x) \approx (s_{j+1} - s_j) \phi(x_j) \equiv d_j \phi_j \quad (7.3)$$

$$\begin{aligned} \int_{s_j}^{s_{j+1}} dx \sin[Qx + \phi(x)]\delta(x - x_j) &= \sin[\phi(x_j) + Qx_j] \\ &\approx \sin[\phi_j - \beta_j] \end{aligned} \quad (7.4)$$

$$\begin{aligned} \int_{s_j}^{s_{j+1}} dx \frac{\partial^2 \phi}{\partial x^2} &= \left[\frac{\partial \phi}{\partial x} \right]_{s_j}^{s_{j+1}} \\ &\approx \frac{\phi_{j+1} - \phi_j}{x_{j+1} - x_j} - \frac{\phi_j - \phi_{j-1}}{x_j - x_{j-1}} \equiv \Delta \phi_j \end{aligned} \quad (7.5)$$

$$\int_{s_j}^{s_{j+1}} dx E(x) \approx d_j E(x_j) \equiv d_j E_j, \quad (7.6)$$

where $s_j = (x_{j-1} + x_j)/2$, and $\beta_j \equiv -Qx_j$. (If the average impurity spacing is much larger than the CDW wavelength, then the β_j can be considered to be random numbers modulo 2π .) The discrete equations of motion then become [125]:

$$\gamma_0 d_j \dot{\phi}_j = K \Delta \phi_j - \sin(\phi_j - \beta_j) + d_j E_j(t). \quad (7.7)$$

The CDW current density J_{CDW} coexists with a normal current density j_N , which together form an incompressible fluid:

$$\nabla \cdot j = \frac{dJ_{\text{CDW}}}{dx} + \frac{dJ_N}{dx} = 0, \quad (7.8)$$

where $J_{\text{CDW}}(x) = \dot{\phi}(x)$ and $J_N(x) = E(x)/\gamma_1$. Here γ_1 is the resistance of the uncondensed carriers which are excited across the CDW gap at finite temperature. Condition 7.8 implies that the total current obeys the condition

$$J(x) = \frac{1}{L} \int_0^L dx J(x), \quad (7.9)$$

where $L = \sum_{j=1}^N d_j$ is the length of the CDW. The discrete version of Eq.7.9 is the following:

$$\begin{aligned} \dot{\phi}_j + \frac{E_j}{\gamma_1} &= \frac{1}{L} \sum_{k=1}^N d_k \left(\dot{\phi}_k + \frac{E_k}{\gamma_1} \right) \\ &\equiv \langle \dot{\phi}_k \rangle_k + \frac{E}{\gamma_1}, \end{aligned} \quad (7.10)$$

If one substitutes for $d_j E_j$ using Eq. 7.10, then Eq. 7.7 becomes:

$$\begin{aligned} (\gamma_0 + \gamma_1) d_j \dot{\phi}_j &= K \Delta \phi_j - \sin(\phi_j - \beta_j) + \\ &d_j E(t) + \gamma_1 d_j \langle \dot{\phi}_k \rangle_k. \end{aligned} \quad (7.11)$$

7.4.3 Numerical Experiments

We have studied the impulse response of Eq. 7.11 as a function of γ_1/γ_0 and initial configuration, in analogy with the experiments described in Section 7.3. We chose a system of size $L = N = 64$, with $K = 0.1$. Periodic boundary conditions were employed. Time is measured in units of γ_0 , which is set to $\gamma_0 = 1$ in all the computations. We looked at a single distribution of impurities x_j , and we do not expect the general results to depend critically on the exact distribution. Our aim was to reproduce qualitatively the striking features of our experiments on delayed conduction. We have not attempted to make a quantitative comparison of experiment and theory, although such a comparison is in principle possible. We have concentrated on features of our results which appear robust in the three samples which we have examined.

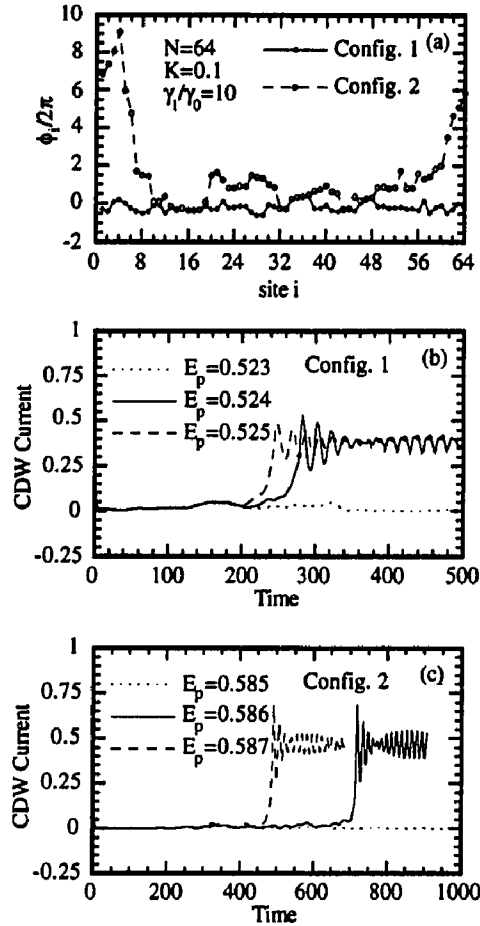


Figure 7.12: Numerical simulations of Eq. 7.11 for two different initial configurations. (a) Plot of two initial configurations. For configuration 1, the CDW is in a relaxed state of minimum strain energy, obtained by letting the CDW relax from $\phi_i=0$ at $t = -\infty$. For configuration 2, the CDW was allowed to relax to a metastable condition after a pulse (which did not switch) with $E_p = 0.523$. (b) Current versus time for three values of E_p for configuration 1. At $E_p=0.523$, the CDW remains pinned, but slides after a delay $\tau=270$ for $E_p=0.524$, and $\tau=250$ for $E_p=0.525$. (c) Current versus time for three values of E_p for configuration 2. Note the change in time scale. At $E_p=0.585$, the CDW remains pinned, but slides after a delay $\tau=700$ for $E_p=0.586$, and $\tau=475$ for $E_p=0.587$.

In the first set of numerical experiments, we applied a time-dependent field $E(t)$ of the form

$$\begin{aligned} E(t) &= 0, & t < 0 \\ E(t) &= E_p, & t \geq 0, \end{aligned} \quad (7.12)$$

starting from two different initial configurations, as shown in Fig. 7.12(a). Configuration 1 was obtained by setting all of the phases ϕ_j to zero and allowing the CDW to relax into a metastable state. Configuration 2 was obtained by allowing the final configuration of one of the first pulses with $E_p = 0.523$ to relax at zero field. Fig. 7.12(b) shows the CDW current as a function of time for two different values of E_p and $\gamma_1 = 10$, starting from configuration 1. For $E_p = 0.523$, the CDW polarizes, but does not switch. The CDW switches for $E_p = 0.524$, and the delay changes from $\tau = 270$ to $\tau = 240$ when E_p is increased to $E_p = 0.525$. Fig. 7.12(c) shows the CDW current as a function of time for two different values of E_p and $\gamma_1 = 10$, starting from configuration 2. When the CDW starts in a highly polarized state, the polarization currents become much smaller, and the switching delays much longer. For $E_p = 0.585$, the CDW polarizes somewhat but does not switch. For $E_p = 0.586$, the CDW switches near $t = 700$, more than three times longer than near threshold in the unpolarized case (note the change of time scale). The dependence of τ on E_p is also more pronounced for configuration 2. The pulse for which $E_p = 0.587$ switches near $t = 475$, a much larger fractional change than for configuration 1.

The threshold for conduction E_p^{th} depends on the initial configuration. Fig. 7.13 shows a plot of the final CDW current versus E_p for configurations 1 and 2. The current for configuration 1 is offset slightly for clarity. The dashed line represents the hysteretic I - V curve obtained by slowly ramping the field E . Just as was seen experimentally in Fig. 7.9, E_p^{th} is much smaller for configuration 1 where the CDW is unpolarized, than for configuration 2, where the CDW is initially polarized.

We have also examined switching behavior in Eq. 7.11 as a function of γ_1 , the normal carrier resistance. Fig. 7.14 shows a plot of the current versus time for three values of γ_1 for the unpolarized initial condition shown in Fig. 7.12(a). Not shown in this figure is a small initial polarization current which is independent of γ_1 . The current quickly drops to almost zero after that, and remains small until $t = \tau$, when the current switches on. At the switch, the current oscillations are quite large, and the current has been averaged over several oscillation periods for the sake of clarity (*c.f.* Fig. 7.17(b)). It takes a time t_{sw} for the current to reach a maximum. As one can see from Fig. 7.14, both τ and t_{sw} are proportional to γ_1 .

The dependence of the delay τ on $\epsilon \equiv (E_p - E_p^{\text{th}})/E_p^{\text{th}}$ is shown in Fig. 7.15. Very close to $\epsilon = 0$, τ depends quite sensitively on ϵ , becoming less so for $\epsilon \geq 0.05$. As one can see, τ drops roughly exponentially as ϵ is increased, similar to that seen experimentally (*c.f.* Fig. 7.4). The dependence is more closely exponential for $\gamma_1 = 50$ than for $\gamma_1 = 10$.

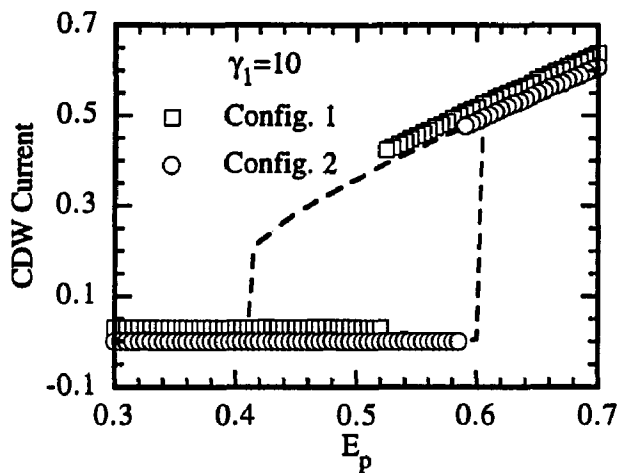


Figure 7.13: Final CDW current versus pulse height E_p for configurations 1 and 2 and $\gamma_1=10$. The current for configuration 1 is shifted slightly for clarity. The transition to the sliding state occurs at a smaller value of E_p for the unpolarized state.

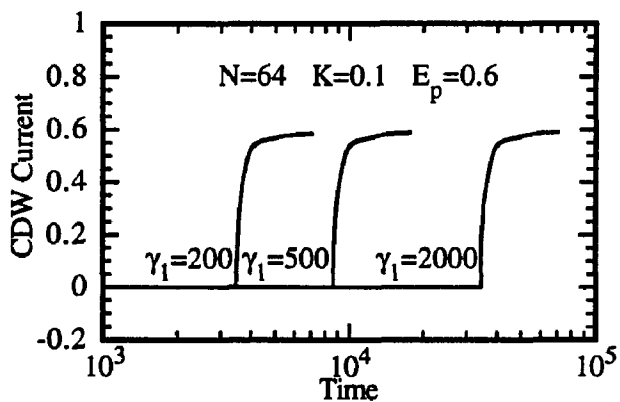


Figure 7.14: CDW current response to a pulse $E_p = 0.6$ for three different values of γ_1 , the normal carrier resistance. The current has been coarse-grained in time for clarity (c.f. Fig. 7.17). The three current traces appear shifted by a constant horizontal amount, indicating that both the delay time τ and the switching time t_{sw} are proportional to γ_1 .

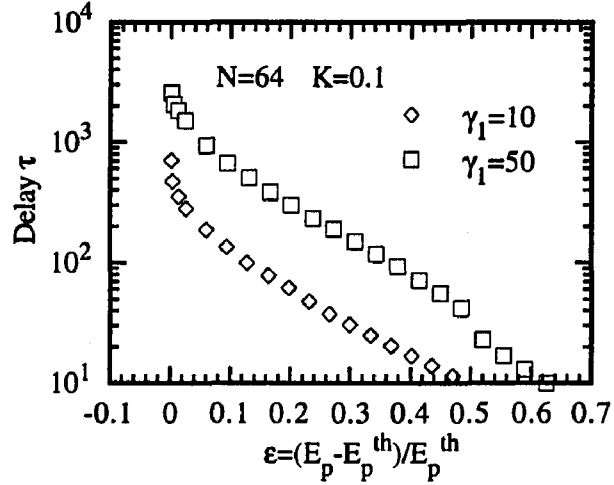


Figure 7.15: Plot of delay τ versus reduced pulse height ϵ for two values of γ_1 . The initial configuration is a polarized state similar to that shown in Fig. 7.12. For $\epsilon < 0.02$, τ depends quite sensitively on ϵ . Above $\epsilon = 0.02$, the decrease in τ is much less rapid, although still approximately exponential. For $\gamma_1=50$, there is a discontinuous jump near $\epsilon = 0.5$, corresponding to the condition $|\Psi(t=0)| = E_p$.

7.5 Analysis and Discussion

7.5.1 Origin of Delayed Conduction

In trying to understand why delayed conduction is observed at all in Eq. 7.11, it is useful to define a complex order parameter:

$$\Psi \equiv r e^{i\theta} \equiv \frac{1}{N} \sum_{j=1}^N e^{i(\phi_j - \beta_j)} \equiv \frac{1}{N} \sum_{j=1}^N \psi_j \quad (7.13)$$

The order parameter is represented graphically in Fig. 7.16. The spatially-averaged pinning energy E_{pin} and pinning force F_{pin} are given in terms of Ψ by

$$U_{\text{pin}} = -r \cos(\theta) \quad (7.14)$$

$$F_{\text{pin}} = -r \sin(\theta), \quad (7.15)$$

whereas the CDW current is given by

$$\gamma_0 \langle \dot{\phi}_k \rangle_k = E(t) + F_{\text{pin}} = E(t) - r \sin(\theta) \quad (7.16)$$

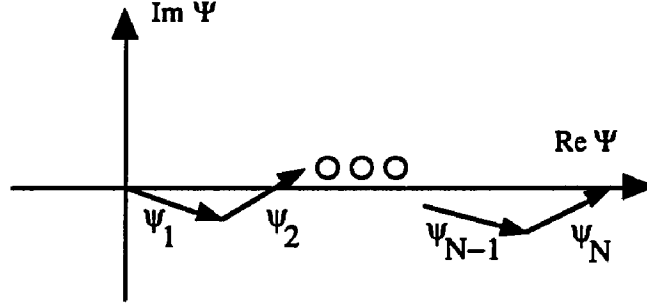


Figure 7.16: Phasor representation of the order parameter $\Psi = \frac{1}{N} \sum_{i=1}^N \psi_i \equiv \frac{1}{N} \sum_{i=1}^N \exp(\phi_i - \beta_i)$. The space-averaged CDW velocity $\dot{\Phi} = E(t) - \text{Im } \Psi$, while the pinning energy $E_{\text{pin}} = -\text{Re } \Psi$. In the $E = 0$ pinned state, $\text{Im } \Psi = 0$ exactly, and for strong pinning $|\Psi| \approx 1$.

and is well approximated by $(\dot{\phi}_k)_k \approx \dot{\theta}$ when $\gamma_1 \gg \gamma_0$, for reasons which will become clear below. We shall consider the case of strong pinning ($K \ll 1$), which is both conceptually simpler and the case we have considered in our simulations. In the $E = 0$ pinned state, U_{pin} will be minimized, which means that $r \approx 1$, or $\phi_j - \beta_j \approx 0 = \theta$ for all j .

If the normal carrier resistance γ_1 is much larger than the intrinsic CDW damping γ_0 , then there is a separation of time scales for the rigid translation of the CDW and the motion of internal degrees of freedom. However, there is an important coupling between the two, and it is this coupling which leads to conduction delays. To see why this is so, we define new variables Φ and η_j , which correspond to the rigid translation of the CDW and to the motion of internal degrees of freedom, respectively:

$$\Phi \equiv \langle \phi_k \rangle_k \quad (7.17)$$

$$\eta_j \equiv \phi_j - \Phi \quad (7.18)$$

The equations of motion for these new variables can be found from Eq. 7.11:

$$\gamma_0 \dot{\Phi} = -r \sin(\theta) + E(t) \quad (7.19)$$

$$\begin{aligned} (\gamma_0 + \gamma_1) d_j \dot{\eta}_j &= K \Delta \eta_j - \sin(\eta_j - \beta_j + \Phi) \\ &\quad + d_j r \sin(\theta) \end{aligned} \quad (7.20)$$

One can find the equation of motion for the magnitude and phase of the order parameter Ψ :

$$\dot{\theta} = \frac{1}{N} \sum_{j=1}^N \frac{1}{r} \cos(\eta_j - \beta_j + \Phi - \theta) \eta_j + \dot{\Phi} \quad (7.21)$$

$$\dot{r} = \frac{1}{N} \sum_{j=1}^N -\sin(\eta_j - \beta_j + \Phi - \theta) \eta_j \quad (7.22)$$

By combining Eq. 7.19 and Eq. 7.21, one sees that when the pulse is turned on, the CDW behaves like a single-degree-of-freedom damped driven pendulum:

$$\gamma_0 \dot{\theta} = E_p - r(t) \sin(\theta) + \mathcal{O}(\gamma_0/\gamma_1). \quad (7.23)$$

The initial polarization of the CDW is brief, and after a time $t \sim \gamma_0$ the CDW current drops almost to zero. The internal degrees of freedom move on a time scale γ_1 . For now, let us consider the case in which the CDW is initially unpolarized. Then, one can ignore the elastic contributions, and the η_j obey the approximate equation:

$$\begin{aligned} (\gamma_0 + \gamma_1) \dot{\eta}_j &\approx r \sin(\theta) - \sin(\eta_j - \beta_j + \Phi)/d_j \\ &\approx E_p - \sin(\eta_j - \beta_j + \Phi)/d_j \end{aligned} \quad (7.24)$$

The η_j for which $d_j > 1$ will be above “threshold” and will advance, while the η_j for which $d_j < 1$ will remain “pinned” and will in fact move slightly in the opposite direction, due to the value of Φ . The net result is that the magnitude r will decrease due to dephasing of the order parameter. This dephasing occurs on a time scale γ_1 . As r decreases, the effective threshold in Eq. 7.23 decreases, and when $r \approx E$, the CDW switches. Even when the CDW begins to slide, there is still a bottleneck because r is still comparable to E . The steady state is characterized by $r \approx 0$, and takes a time $t_{sw} \propto \gamma_1$ to approach that state. Hence both τ and t_{sw} are proportional to γ_1 .

The motion of the order parameter Ψ is shown graphically in Fig. 7.17(a) for a numerical simulation in which $\gamma_1=50$, and $E_p = 0.6$. The dashed line corresponds to $\text{Im}\Psi = E_p = 0.6$. At point A, $t = 0$, and the current $\dot{\Phi} = 0.6$. The order parameter Ψ moves in a circular arc towards point B, which is reached at $t = 6$. The dynamics are very slow as Ψ creeps along the dashed line, and at $t = 933$ the current has reached point C. The peak of the first current oscillation occurs at point D at $t = 945$. The corresponding CDW current is plotted versus time in Fig. 7.17(b). The current oscillations are quite large when the CDW switches because r is still large. The fact that the current oscillations are large is an artifact of the equations of motion in one spatial dimension, and are not expected to be large in higher dimensions.

7.5.2 Dependence on Initial Configuration

It was seen both experimentally and numerically that the threshold for conduction depended sensitively on the initial configuration. Experimentally, the threshold voltage V_p^{th} was lower if the CDW configuration was prepared either by heating the CDW above the Peierls transition or by polarizing it in the opposite direction. Numerically, we observe a

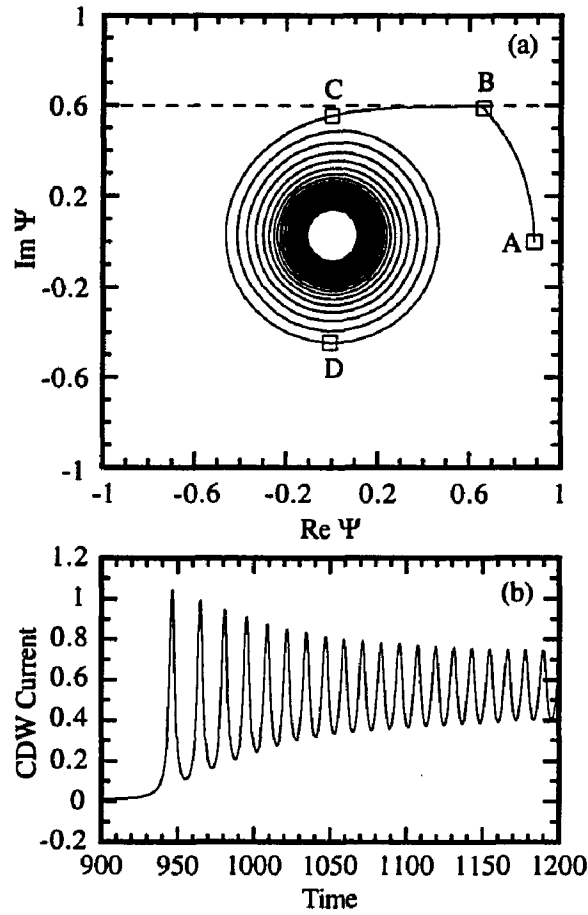


Figure 7.17: (a) “Configuration-space” plot of $\Psi(t) = r(t)\exp(i\theta(t))$ for $\gamma_1/\gamma_0 = 50$, and $E_p = 0.6$, beginning from a polarized configuration. The dashed line corresponds to $\text{Im}\Psi = E_p$. The CDW current is given by $\gamma_0\langle\phi_k\rangle_k = E_p - \text{Im}\Psi$. The CDW begins at point A at $t = 0$ in a state of minimum pinning energy, with $\Psi(t = 0) = 0.88$. When the pulse is turned on, θ increases with r essentially constant until Ψ approaches the dashed line at point B. At this point the velocity is nearly zero. Because of the distribution of impurity domain sizes d_j , the ψ_j begin to dephase, and r decreases at a rate $\propto \gamma_1$. Near point C, $r \approx E_p$, and the CDW can begin to slide quasi-rigidly, and $\Psi(t)$ spirals in toward $r \approx 0$. The peak of the first current oscillation occurs at point D. (b) Plot of CDW current for same conditions as in (a). The current increases abruptly near $t = 940$. The current oscillations are large near the beginning of the switch because $|\Psi(t)| \approx E_p$, and the CDW is behaving like a single degree of freedom oscillator near threshold.

similar dependence on initial configuration. If the CDW begins in a polarized configuration, then the amount of dephasing of Ψ will be much smaller because the “local fields” which cause the η_j to move at different velocities in Eq. 7.20 will be counterbalanced by elastic forces, and the threshold field will increase as a result.

Experimentally, the polarization currents were much larger when the initial configuration was prepared by heating the CDW above T_P than by driving the CDW with a pulse of the opposite sign. The excess current seen in the heating experiments may be due to a weak temperature dependence in the CDW wavevector Q . This hypothesis is consistent with a small shift in the CDW wavevector observed by x-ray diffraction, depending on whether the CDW was cooled in zero electric field or driven above threshold [126]. This effect cannot be modeled using closed boundary conditions, but presumably could if one employed open boundary conditions.

7.5.3 Pulse Height Dependence

The dependence of τ on pulse height agrees well between experiment and theory. In both cases one sees roughly two regions: for very small reduced field ϵ there is a very sensitive dependence of τ on ϵ , whereas for larger ϵ the delay τ decreases approximately exponentially with ϵ . We have not tried to find numerically the distribution of delays versus ϵ because that would require knowing the distribution of initial configurations, but we do expect a more sensitive dependence of τ on initial configuration near the threshold. The threshold itself depends on the initial configuration, as was discussed in Sec. 7.5.2.

7.5.4 Temperature Dependence

The temperature dependence of the average delay τ and the switching time t_{sw} were both found to be activated with an activation energy E_a comparable to the CDW gap. Numerically, it was found that both τ and t_{sw} were proportional to γ_1 , where γ_1 is interpreted as the resistance due to uncondensed carriers. In a semiconducting CDW, one would expect γ_1 to be activated. In order for the numerical simulations to be consistent with experiment, one must assume that

$$\gamma_1 \propto \exp(E_a/k_B T). \quad (7.25)$$

In NbSe₃ however, the Fermi surface is not completely gapped, and hence contributions to the ohmic conductivity come from both quasiparticles excited across the CDW gap and from ungapped electrons. Below $T = 48$ K the resistance in NbSe₃ *decreases* with temperature, while the hysteresis in the I - V curves *increases*. Although it appears difficult to justify microscopically, the evidence is quite compelling that the ungapped electrons in NbSe₃ do not play a significant role in screening CDW fluctuations [101, 122].

The remarkable qualitative agreement between the experimental results and numerical simulations provides strong evidence that the mechanism for switching in $NbSe_3$ is governed by the interaction between the CDW and uncondensed carriers. However, assumption 7.25 is clearly at odds with the fact that $NbSe_3$ is metallic at low temperatures. The mounting body of evidence consistent with this assumption impels us to search for a microscopic description.

Chapter 8

Conclusions

It is difficult to write a conclusion for this thesis. Research is an ongoing process in which one aims for a complete understanding of a given phenomenon; one can only hope to achieve a more accurate approximation to the truth. When I began my thesis work there were many outstanding questions related to CDW phenomena.

Perhaps the least well-understood of all CDW phenomena was the hysteretic “switching” behavior observed in some, but not all, samples of NbSe_3 and other CDW compounds. Some of the questions related to switching behavior are itemized below:

- What is the physical origin of switching?
- Why do some samples switch and others not?
- Why do switching samples behave chaotically in response to rf driving, whereas non-switching samples do not?
- What is the physical origin of delayed conduction?
- Why are there fluctuations in the conduction delay times?

This thesis has addressed many of these questions, and has raised several new ones as well. There is compelling evidence that switching behavior has its origin in the interaction of the CDW with uncondensed carriers. If one assumes that the CDW and uncondensed electrons form an incompressible fluid, then it is easy to show that one obtains a global coupling term which gives rise to switching behavior. This model was described in chapter 6. The strongest argument in favor of this model comes from the comparison between experiment and theory in chapter 7, where nearly every aspect of the phenomena of delayed conduction is shown to be consistent with numerical experiments based on the model described in chapter 6. There are, however, many unanswered questions related to switching phenomena.

The low-dimensional chaotic behavior described in chapter 5 does not appear in the one-dimensional model presented in chapter 6. Perhaps the generalization of the model to higher spatial dimensions will reveal such behavior. Another important unanswered question is related specifically to the switching behavior of NbSe_3 : Why does NbSe_3 behave as though it were a semiconducting material? In actuality, there are uncondensed carriers at low temperatures, and yet all of the evidence suggests that they play no part in the screening of CDW deformations which gives rise to global coupling. In my opinion, this is perhaps the most fascinating unresolved issue related to switching phenomena.

The nature of mode-locking was not very well understood either. In particular, the question of whether many degrees of freedom were essential to the description of mode-locking was a hotly debated subject. There were many mysterious observations, such as large amplitude fluctuations of the narrow-band noise when the CDW was locked in the 1 : 2 mode-locked state. The techniques of nonlinear dynamics have proved quite useful in understanding the behavior of mode-locking in CDWs. By measuring time-series, we were able to obtain information about the mode-locked state which could not be obtained by other types of measurements. Our results made it clear that many degrees of freedom were essential to describing the phenomena of mode-locking. We were also able to explain the amplitude fluctuations in terms of the motion of "dynamical solitons", topological features whose existence is predicted by the classical-deformable Fukuyama-Lee-Rice model.

The time-domain methods which were successfully applied to understanding mode-locking in the non-switching regime was also used to study chaos in "switching" samples of NbSe_3 . With these techniques we were able to show that the chaotic behavior was low-dimensional, and is consistent with the dynamics of two coupled first-order nonlinear ordinary differential equations with periodic driving and noise. The shape of the chaotic attractor was reproduced in a second sample, indicating that the behavior is robust, and therefore provides strong quantitative constraints on any theory of switching CDW dynamics. At the present time, no model of CDWs has been successful in reproducing the chaotic behavior we observed, although I am hopeful that a detailed study of the model presented in chapter 6, generalized to higher spatial dimensions, will exhibit such behavior.

Charge-density waves provide unique, highly accessible experimental system in which to study the behavior of extended nonlinear dynamical systems driven far from equilibrium. Conversely, the tools of nonlinear dynamics and time-series analysis have proven useful in understanding the physics of charge-density waves. I hope that it has become clear to the reader after reading this thesis that the fields of nonlinear dynamics and charge-density waves have a lot yet to learn to one another.

Bibliography

- [1] A. J. Berlinsky, Rep. Prog. Phys. **42**, 1243 (1979).
- [2] G. Grüner and A. Zettl, Phys. Rep. **119**, 117 (1985).
- [3] S. Kagoshima, H. Nagasawa, and T. Sambongi, in *One-Dimensional Conductors*, No. 72 in *Springer Series in Solid-State Sciences*, edited by M. Cardona, P. Fulde, K. von Klitzing, and H. J. Queisser (Springer-Verlag, Berlin, 1988).
- [4] G. Gruner, Rev. Mod. Phys. **60**, 1129 (1988).
- [5] *Charge-Density Waves in Solids*, No. 25 in *Modern Problems in Condensed Matter Sciences*, edited by L. P. Gor'kov and G. Grüner (North-Holland, Amsterdam, 1989).
- [6] R. E. Peierls, *Quantum Theory of Solids* (Oxford University Press, London, 1955).
- [7] R. E. Thorne, Ph.D. thesis, Cornell University, University of Illinois at Urbana-Champaign, 1987.
- [8] For a review of mode-locking in CDWs, see S. E. Brown and A. Zettl, in *Charge Density Waves in Solids*, edited by L. P. Gorkov and G. Grüner, *Modern Problems in Condensed Matter Sciences*, Vol. 25 (North-Holland, Amsterdam, 1989), p. 223.
- [9] P. Haen *et al.*, in *Low Temperature Physics-LT14*, edited by M. Krusius and M. Vuorio (American Elsevier, ADDRESS, 1975), Vol. 5.
- [10] R. E. Thorne, Phys. Rev. B **45**, 5804 (1992).
- [11] L. Pietronero and S. Strässler, Phys. Rev. B **28**, 5863 (1983).
- [12] P. B. Littlewood, Phys. Rev. B **33**, 6694 (1986).
- [13] S. N. Coppersmith, Phys. Rev. B **44**, 2887 (1991).
- [14] P. B. Littlewood, Phys. Rev. B **33**, 6694 (1986).
- [15] P. A. Lee and H. Fukuyama, Phys. Rev. B **17**, 542 (1978).

- [16] E. Sweetland *et al.*, Phys. Rev. Lett. **65**, 3165 (1990).
- [17] R. M. Fleming *et al.*, Phys. Rev. B **33**, 5450 (1986).
- [18] L. Mihály and G. X. Tessema, Phys. Rev. B **33**, 5858 (1986).
- [19] P. B. Littlewood, Solid State Comm. **65**, 1347 (1988).
- [20] L. Sneddon, Phys. Rev. Lett. **52**, 65 (1984).
- [21] A. Zettl and G. Grüner, Phys. Rev. B **29**, 755 (1984).
- [22] R. M. Fleming and C. C. Grimes, Phys. Rev. Lett. **42**, 1423 (1979).
- [23] G. Mozurkewich and G. Gruner, Phys. Rev. Lett. **51**, 2206 (1983).
- [24] S. E. Brown and L. Mihaly, Phys. Rev. Lett. **55**, 742 (1985).
- [25] N. P. Ong, G. Verma, and K. Maki, Phys. Rev. Lett. **52**, 663 (1984).
- [26] N. P. Ong and K. Maki, Phys. Rev. B **32**, 6582 (1985).
- [27] S. M. Shapiro, Phys. Rev. Lett. **11**, 80 (1963).
- [28] P. Monceau, J. Richard, and M. Renard, Phys. Rev. Lett. **45**, 43 (1980).
- [29] A. A. Middleton, O. Biham, P. B. Littlewood, and P. Sibani, Phys. Rev. Lett **68**, 1586 (1992).
- [30] M. P. Maher *et al.*, Phys. Rev. B **43**, 9968 (1991).
- [31] P. Monceau, J. Richard, and M. Renard, Phys. Rev. B **25**, 931 (1982).
- [32] M. S. Sherwin and A. Zettl, Phys. Rev. B **32**, 5536 (1985).
- [33] R. E. Thorne, J. R. Tucker, and J. Bardeen, Phys. Rev. Lett. **58**, 828 (1987).
- [34] R. E. Thorne *et al.*, Phys. Rev. B **37**, 10055 (1988).
- [35] D. S. Fisher, Phys. Rev. B **31**, 1396 (1985).
- [36] S. E. Brown, G. Mozurkewich, and G. Gruner, in *Charge-Density Waves in Solids*, edited by G. Hutiray and J. Solyom (Springer-Verlag, Berlin, 1985), Vol. 217.
- [37] S. Bhattacharya, J. P. Stokes, M. J. Higgins, and R. A. Klemm, Phys. Rev. Lett. **59**, 1849 (1987).
- [38] S. Bhattacharya, M. J. Higgins, and J. P. Stokes, Phys. Rev. B **38**, 10093 (1988).

- [39] K. Wiesenfeld and I. Satija, *Phys. Rev. B* **36**, 2483 (1987).
- [40] M. F. Crommie, K. Craig, M. S. Sherwin, and A. Zettl, *Phys. Rev. B* **43**, 13699 (1991).
- [41] M. H. Jensen, P. Bak, and T. Bohr, *Phys. Rev. Lett.* **50**, 1637 (1983).
- [42] M. H. Jensen, P. Bak, and T. Bohr, *Phys. Rev. A* **30**, 1960 (1984).
- [43] T. Bohr, P. Bak, and M. H. Jensen, *Phys. Rev. A* **30**, 1970 (1984).
- [44] M. J. Feigenbaum, *J. Stat Phys.* **19**, 25 (1979).
- [45] M. J. Feigenbaum, *J. Stat Phys.* **21**, 669 (1979).
- [46] M. J. Feigenbaum, L. P. Kadanoff, and S. J. Shenker, *Physica* **5D**, 370 (1982).
- [47] R. P. Hall, M. S. Sherwin, and A. Zettl, *Phys. Rev. B* **29**, 7076 (1984).
- [48] M. S. Sherwin, A. Zettl, and R. P. Hall, *Phys. Rev. B* **38**, 13028 (1988).
- [49] K. Svoboda, A. Zettl, and M. S. Sherwin, *Solid State Comm.* **70**, 859 (1989).
- [50] M. P. Everson and R. V. Coleman, *Phys. Rev. Lett.* **28**, 6659 (1983).
- [51] R. P. Hall, M. F. Hundley, and A. Zettl, *Phys. Rev. B* **38**, 13002 (1988).
- [52] R. P. Hall and A. Zettl, *Solid State Comm.* **50**, 813 (1984).
- [53] A. Zettl and G. Grüner, *Phys. Rev. B* **26**, 2298 (1982).
- [54] R. P. Hall, M. S. Sherwin, and A. Zettl, *Phys. Rev. Lett.* **52**, 2293 (1984).
- [55] G. Kriza, A. Janossy, and G. Mihaly, in *Delayed Switching Between Normal and CDW Conducting States in o-TaS₃*, Vol. 217 of *Lecture Notes in Physics*, edited by G. Hutiray and J. Solyom (Springer-Verlag, Berlin, 1984), p. 426.
- [56] M. Inui, R. P. Hall, S. Doniach, and A. Zettl, *Phys. Rev. B* **38**, 13047 (1988).
- [57] For a review of the dynamics of switching CDWs, see R. P. Hall, M.F. Hundley, and A. Zettl, *Phys. Rev. B* **38**, 13002 (1988); R. P. Hall and A. Zettl, *ibid.*, **38**, 13019; M. S. Sherwin, A. Zettl, and R. P. Hall, *ibid.*, **38**, 13028 (1988), and references therein.
- [58] C. M. Marcus, S. H. Strogatz, and R. M. Westervelt, *Phys. Rev. B* **40**, 5588 (1989).
- [59] S. Bhattacharya, M. J. Higgins, and J. P. Stokes, *Phys. Rev. Lett.* **63**, 1503 (1989).
- [60] G. Mihaly and L. Mihaly, *Phys. Rev. Lett.* **52**, 149 (1984).
- [61] S. Zhu, A. W. Wu, and R. Roy, *Phys. Rev. A* **34**, 4333 (1986).

- [62] See for example, G. Ahlers, in *Complex Systems, SFI Studies in the Sciences of Complexity*, edited by D. Stein (Addison-Wesley Longman, Reading, MA 1989), p. 197.
- [63] J. C. Gill, *Solid State Comm.* **39**, 1203 (1981).
- [64] B. Joos and D. Murray, *Phys. Rev. B* **29**, 1094 (1984).
- [65] S. H. Strogatz and R. M. Westervelt, *Phys. Rev. B* **40**, 10501 (1989).
- [66] Large lattice defects can be ultrastrong pinning centers. See Ref. [49].
- [67] S. H. Strogatz, C. M. Marcus, R. M. Westervelt, and R. E. Mirollo, *Phys. Rev. Lett.* **61**, 2380 (1988).
- [68] K. Wiesenfeld and M. Sherwin, *Phys. Rev. A* **45**, 3467 (1992).
- [69] P. Colet and K. Wiesenfeld, *Phys. Rev. A* **46**, 4676 (1992), *physical Review A (Statistical Physics, Plasmas, Fluids, and Related Interdisciplinary Topics)*, 15 Oct. 1992, vol.46, (no.8):4676-88.
- [70] R. P. Hall and A. Zettl, *Phys. Rev. B* **30**, 2279 (1984).
- [71] S. E. Brown, G. Mozurkewich, and G. Gruner, *Phys. Rev. Lett.* **52**, 2277 (1984).
- [72] S. Bhattacharya, M. J. Higgins, and J. P. Stokes, *Phys. Rev. B* **38**, 7177 (1988).
- [73] S. N. Coppersmith and P. B. Littlewood, *Phys. Rev. Lett.* **57**, 1927 (1986).
- [74] H. Matsukawa and H. Takayama, *J. Phys. Soc. Jpn.* **56**, 1507 (1987).
- [75] H. Matsukawa, *J. Phys. Soc. Jpn.* **56**, 1522 (1987).
- [76] S. Martin and W. Martienssen, *Phys. Rev. Lett.* **56**, 1522 (1986).
- [77] E. G. Gwinn and R. M. Westervelt, *Phys. Rev. Lett.* **59**, 157 (1987).
- [78] C. Myers and J. Sethna, unpublished. (unpublished).
- [79] See, for example, S. Neil Rasband, *Chaotic Dynamics of Nonlinear Systems*, (Wiley, New York, 1990), pp. 200ff, and references therein.
- [80] H. Fukuyama and P. A. Lee, *Phys. Rev. B* **17**, 535 (1978); P. A. Lee and T. M. Rice, *Phys. Rev. B* **19**, 3870 (1979).
- [81] H. Matsukawa, *Synth. Met.* **29**, F343 (1989).
- [82] M. J. Rice, A. R. Bishop, J. A. Krumhansl, and S. E. Trullinger, *Phys. Rev. Lett.* **36**, 432 (1976).

- [83] W. P. Su, J. R. Schrieffer, and A. J. Heeger, *Phys. Rev. Lett.* **42**, 1698 (1979).
- [84] For recent reviews of the dynamics of sliding charge-density waves, see *Charge Density Waves in Solids*, edited by L. P. Gorkov and G. Grüner, *Modern Problems in Condensed Matter Sciences Vol. 25* (North-Holland, Amsterdam, 1989).
- [85] P. Monceau, J. Richard, and M. Renard, *Phys. Rev. Lett.* **45**, 43 (1980).
- [86] For a review of mode-locking in CDWs, see S. E. Brown and A. Zettl, in *Charge-Density Waves in Solids*, edited by L. P. Gorkov and G. Grüner, *Modern Problems in Condensed Matter Sciences Vol. 25* (North-Holland, Amsterdam, 1989), p.223.
- [87] R. M. Fleming and L. F. Schneemeyer, *Phys. Rev. B* **33**, 2930 (1986).
- [88] S. N. Coppersmith and P. B. Littlewood, *Phys. Rev. B* **36**, 311 (1987).
- [89] C. Tang *et al.*, *Phys. Rev. Lett.* **58**, 1161 (1987).
- [90] J. Levy and M. S. Sherwin, *Phys. Rev. Lett.* **67**, 2846 (1991); J. Levy and M. S. Sherwin, in *Proceedings of the 1st Experimental Chaos Conference*, edited by S. Vohra, M. Spano, M. Shlesinger, L. M. Pecora, and W. Ditto, (World Scientific, New Jersey, 1992).
- [91] J. Levy and M. S. Sherwin, *Phys. Rev. B* **43**, 8391 (1991).
- [92] K. Wiesenfeld, *J. Stat. Phys.* **38**, 1071 (1985).
- [93] J. Levy, M. S. Sherwin, and J. Theiler, *Phys. Rev. Lett.* **70**, 2957 (1993).
- [94] For a recent review which describes a variety of methods for nonlinear time series analysis, see P. Grassberger, T. Schreiber, and C. Schaffrath, *Int. J. Bif. Chaos* **1**, 521 (1991).
- [95] Because (as Figs. 5.5(d) shows) the low-dimensional data is nearly one-dimensional, and the small extent perpendicular to that dimension is obscured somewhat by noise, a direct dimension estimation did not prove useful.
- [96] J. D. Farmer and J. J. Sidorowich, *Phys. Rev. Lett.* **59**, 845 (1987).
- [97] J. D. Farmer and J. J. Sidorowich, in *Evolution, Learning, and Cognition*, edited by Y. C. Lee (World Scientific, ADDRESS, 1988), pp. 277–330.
- [98] J. Theiler *et al.*, *Physica D* **58**, 77 (1992).

- [99] Further evidence for chaos comes from preliminary estimates of the Lyapunov spectrum, performed by U. Parlitz, which indicate one positive and one negative Lyapunov exponent. These computations are based on the algorithm described in U. Parlitz, *Int. J. Bif. Chaos* **2**, 155 (1992).
- [100] J. Levy and M. S. Sherwin, *Phys. Rev. Lett.* **67**, 2846 (1991).
- [101] J. Levy, M. S. Sherwin, F. F. Abraham, and K. Wiesenfeld, *Phys. Rev. Lett.* **68**, 2968 (1992).
- [102] R. V. C. *et al.*, *Synth. Metals* **19**, 795 (1987).
- [103] L. Sneddon, *Phys. Rev. B* **29**, 719 (1984).
- [104] P. B. Littlewood, in *Computer Simulations of CDW Dynamics*, Vol. 25 of *Modern Problems in Condensed Matter Sciences*, edited by L. P. Gor'kov and G. Grüner (North-Holland, Amsterdam, 1989), p. 321.
- [105] W. L. McMillan, *Phys. Rev. B* **12**, 1197 (1975).
- [106] L. Sneddon, M. C. Cross, and D. S. Fisher, *Phys. Rev. Lett.* **49**, 292 (1982).
- [107] Y. Kim, G. Mihaly, and G. Gruner, *Solid State Comm.* **55**, 663 (1989).
- [108] S. Takada, K. Y. M. Wong, and T. Holstein, *Phys. Rev. B* **32**, 4639 (1985).
- [109] G. Mihaly and P. Beauchene, *Solid State Comm.* **63**, 911 (1987).
- [110] A. A. Middleton, *Phys. Rev. Lett.* **68**, 670 (1992).
- [111] P. Hadley, M. R. Beasley, and K. Wiesenfeld, *Phys. Rev. B* **38**, 8712 (1988).
- [112] K. Wiesenfeld and P. Hadley, *Phys. Rev. Lett.* **62**, 1335 (1989).
- [113] K. Wiesenfeld, C. Braicikowski, G. E. James, and R. Roy, *Phys. Rev. Lett.* **65**, 1749 (1990).
- [114] For a review of the dynamics of sliding charge-density waves, see *Charge Density Waves in Solids*, edited by L. P. Gorkov and G. Grüner, *Modern Problems in Condensed Matter Sciences Vol. 25* (North-Holland, Amsterdam, 1989).
- [115] R. J. Cava *et al.*, *Phys. Rev. Lett.* **53**, 1677 (1984).
- [116] A. Maeda, T. Furuyama, and S. Tanaka, *Solid State Comm.* **55**, 951 (1985).
- [117] A. Maeda, T. Furuyama, K. Uchinokura, and S. Tanaka, *Physica* **143B**, 123 (1986).
- [118] J. Levy and M. S. Sherwin, unpublished.

- [119] W. A. Challener and P. L. Richards, *Solid State Comm.* **52**, 117 (1984).
- [120] A. Fournel *et al.*, *Physica B* **143B**, 177 (1986).
- [121] R. V. Coleman *et al.*, *Appl. Surf. Sci.* **60**, 485 (1992).
- [122] T. L. Adelman *et al.*, *Phys. Rev. B* **47**, 4033 (1993).
- [123] A. Jánossy, G. Mihály, and L. Mihály, in *Relaxation of the Deformed CDW State: Electric and Thermal Hysteresis*, Vol. 217 of *Lecture Notes in Physics*, edited by G. Hutiray and J. Sólyom (Springer-Verlag, Berlin, 1984), p. 412.
- [124] W. Wonneberger and H. J. Breymayer, *Z. Phys. B* **56**, 241 (1984).
- [125] This *ansatz* differs slightly from that of Pietronero and Strässler (Ref. [11]), who assume that the damping only occurs at the impurity sites. This assumption allows the equations of motion to be discretized *exactly*, yielding the following equation of motion:
- $$\gamma_0 \dot{\phi}_j = K \Delta^2 \phi_j + \sin(\phi_j - \beta_j) + d_j E.$$
- These equations give unphysically large strains for large E .
- [126] R. E. Thorne, private communication.